

A Thermodynamic Investigation of Thermochemical Heat Storage Materials

Dissertation with the aim of achieving a doctoral degree at the Faculty
of Mathematics, Informatics and Natural Sciences

Department of Chemistry
of Universität Hamburg

Fritz Höffler

2017 in Hamburg

Die vorliegende Arbeit wurde im Zeitraum vom September 2012 bis September 2017 am Institut für Anorganische und Angewandte Chemie der Universität Hamburg im Arbeitskreis von Prof. Dr. Michael Steiger angefertigt.

1. Gutachter: Prof. Dr. Michael Steiger

2. Gutachterin: Prof. Dr. Carmen Herrmann

Datum der Disputation: 01.12.2017

Danksagung

In aller Form möchte ich mich bei Prof. Dr. Michael Steiger für sein stetiges Interesse am Fortgang dieser Arbeit, seine Diskussionsbereitschaft, seiner Geduld und seinem Vertrauen bedanken. Auch für die Möglichkeiten meine Ergebnisse auf Konferenzen zu präsentieren und mich mit anderen Wissenschaftlern auszutauschen bin ich zu Dank verpflichtet. Des Weiteren war die durgehende finanzielle Unterstützung meiner Promotion keine Selbstverständlichkeit für mich und auch dafür möchte ich mich bedanken.

Dr. Kirsten Linnow möchte ich für die geduldige Einweisung in die Geräte, stete Diskussionsbereitschaft experimentelle Anregungen und die gute Zusammenarbeit im Projekt Thessapor danken.

Prof. Dr. Carmen Herrmann danke ich für die Erstellung des Zweitgutachtens sowie Prof. Dr. Alf Mews und JProf. Dr. Simone Mascotto für die Übernahme des Disputationsbeisitzes.

Meinem gesamten Arbeitskreis (Tobias Grünzel, Nadine Lindström, Kirsten Linnow, Michael Niermann, Amelie Stahlbuck und Tanya Talreja-Muthreja) möchte ich für die freundliche Aufnahme, die gute Zusammenarbeit und unvergessliche Sommerfeste, Betriebsausflüge und Weihnachtsfeiern bedanken. Es sind nicht immer nur die fachlichen Hilfestellungen die einem weiterhelfen sondern oft auch ein freundschaftliches Gespräch. Darüber hinaus gilt mein besonderer Dank Michael Niermann für die unzähligen Stunden an Diskussionen über Konstruktionen, Messtechnik, Materialien, daraus entstandenen Anregungen und seine konstruktive Kritik sowie Unterstützung meiner Arbeit.

Meinen im Rahmen von Masterarbeiten und Praktika betreuten Studierenden Imke Müller und Luc Fünsterer sowie Philipp Merkel und Lars Thormann möchte ich für die ausgezeichnete Zusammenarbeit und die mir entgegengebrachte Geduld bedanken.

Auch dem Team der Forschungswerkstatt der physikalischen Chemie möchte ich für ihre Unterstützung und die Realisierung aller meiner Konstruktionen bedanken.

Dem BMBF und dem BMWi sei für die finanzielle Unterstützung über den Zeitraum dieser Arbeit gedankt.

Besonderer Dank gilt auch den Korrektoren dieser Arbeit für ihre kritische Durchsicht des Manuskripts.

Meiner Familie und meinen Freunden danke ich für die Geduld und Unterstützung während der Entstehung dieser Arbeit. Solch ein Werk entsteht nicht allein im dunklen Kämmerlein sondern bedarf der Hilfe, Anregung, Diskussion und des Ansporns verschiedener Personen. Bei jedem, der am Gelingen dieser Dissertation beteiligt war, bedanke ich mich in diesem Sinne.

List of Notations

ν	stoichiometric coefficient
φ	relative humidity
T	absolute temperature
R	gas constant
p	vapor pressure
a	activity
m	molality
γ	activity coefficient
μ	chemical potential
ϕ	osmotic coefficient
G	Gibbs energy
L	relative enthalpy
H	enthalpy
C_p	heat capacity
A	Debye-Hückel parameter
B	second virial coefficient
C	third virial coefficient
$\beta^{(i)}$	binary interaction parameter
Δp_{cryst}	crystallization pressure
Δp_{hydr}	hydration pressure
K	equilibrium constant
α	numerical constant
b	constant
E	cell potential
F	Faraday constant

1	Introduction	1
1.1	Thermal Storage Technologies	3
1.2	Materials for Thermal Energy Storage	7
1.3	Aim	10
2	Theory and Equations.....	11
2.1	Phase Diagrams.....	11
2.2	Thermodynamics of Electrolyte Solutions	13
2.3	The Ion Interaction Approach.....	16
2.4	The Influence of Pressure on Crystal Growth	21
2.5	Measurement of Activity Data.....	23
3	Thermodynamic properties of $\text{ZnSO}_4(\text{aq})$ and phase equilibria in the $\text{ZnSO}_4\text{--H}_2\text{O}$ system from 268 K to 373 K	25
3.1	Introduction.....	25
3.2	Experimental.....	26
3.3	Theory and Equations	27
3.3.1	Phase Equilibria.....	27
3.3.2	Ion Interaction Model.....	28
3.4	Results and Discussion	29
3.4.1	Experimental Results.....	29
3.4.2	Pitzer Model Parameters for $\text{ZnSO}_4(\text{aq})$	29
3.4.3	Solubility Products of $\text{ZnSO}_4 \cdot n\text{H}_2\text{O}$	34
3.4.4	Phase Diagram $\text{ZnSO}_4\text{--H}_2\text{O}$	40
3.5	Conclusion	44
4	Thermodynamic properties of $\text{CuSO}_4(\text{aq})$ and phase equilibria in the $\text{CuSO}_4\text{--H}_2\text{O}$ system from 271 K to 373 K	45
4.1	Introduction.....	45
4.2	Theory and Equations	47
4.2.1	Phase Equilibria.....	47
4.2.2	Apparent Molar Heat Capacity	47
4.2.3	Ion Interaction Model.....	47
4.3	Experimental.....	48
4.4	Results and Discussion	48

4.4.1	Experimental Results.....	48
4.4.2	Parameterization of $\text{CuSO}_4(\text{aq})$	50
4.4.3	Solubility Products of $\text{CuSO}_4 \cdot n\text{H}_2\text{O}$	55
4.4.4	Phase Diagram of $\text{CuSO}_4\text{--H}_2\text{O}$	60
4.5	Conclusion.....	62
5	Determination of the thermodynamic properties of $\text{CaSO}_4(\text{aq})$ solution with few available data and definition of the phase boundaries in the System $\text{CaSO}_4\text{--H}_2\text{O}$	63
5.1	Introduction.....	63
5.2	Theory.....	64
5.2.1	CaSO_4 Phases.....	64
5.2.2	Phase Equilibria.....	65
5.3	Results and Discussion.....	65
5.3.1	Parameterization of $\text{CaSO}_4(\text{aq})$	65
5.3.2	Solubility Products of $\text{CaSO}_4 \cdot n\text{H}_2\text{O}$	66
5.3.3	Equilibria in Mixed Solutions.....	69
5.3.4	Phase Diagram.....	70
5.4	Conclusion.....	76
6	The measurement of the pressure resistance of mirabilite ($\text{Na}_2\text{SO}_4 \cdot 10\text{H}_2\text{O}$).....	77
6.1	Introduction.....	77
6.2	Experimental Planning and Measurement Setup.....	78
6.3	Experimental Procedure.....	81
6.4	Results and Discussion.....	81
6.4.1	Series 1 at 298.95 K and 85% RH.....	82
6.4.2	Series 2 at 298.95 K and 84% RH.....	84
6.4.3	Influences on the Measurements.....	85
6.5	Conclusion.....	91
7	Conclusion.....	93
8	Abstract.....	95
9	Zusammenfassung.....	97
10	References.....	99
I	Used Chemicals.....	i

II Statement in Lieu of an Oath (Eidesstattliche Versicherung) ii

1 Introduction

From the beginning of human civilization, the capability for the storage of energy has been a key factor for the development towards our modern lifestyle. As advanced the term of energy storage sounds, the simple collection of firewood to provide heat for cooking or through the winter is an early but still present form of energy storage. Its advantages are quickly mentioned. It has a high energy density, can easily be converted in useful types of energy, e.g. heat or light, is reasonably safe and can be stored for a nearly infinite period of time without a loss in its energy content. With the continuous advance of civilization and technology, mankind perpetually accessed new energy reserves and converted them into resources. These can roughly be split in three sectors. There are carbon-based fossil fuels, nuclear power and the renewable energies. In the light of a continuously increasing population and a growing consumption of energy per individual shadowed by the simultaneous release of greenhouse active gases like CO₂ and the dwindling reserves of fossil fuels, the research for alternative types of energy generation and its storage has become a modern but also pressing topic for our society. Figure 1 shows the change in the primary energy generation in the Federal Republic of Germany (FRG) between 1990 and 2015. With the passing of the “Erneuerbare-Energien-Gesetz” (renewable energies act) in 2011, the increase of the ratio of renewable energies in the energy production is politically promoted and the implementation has started.

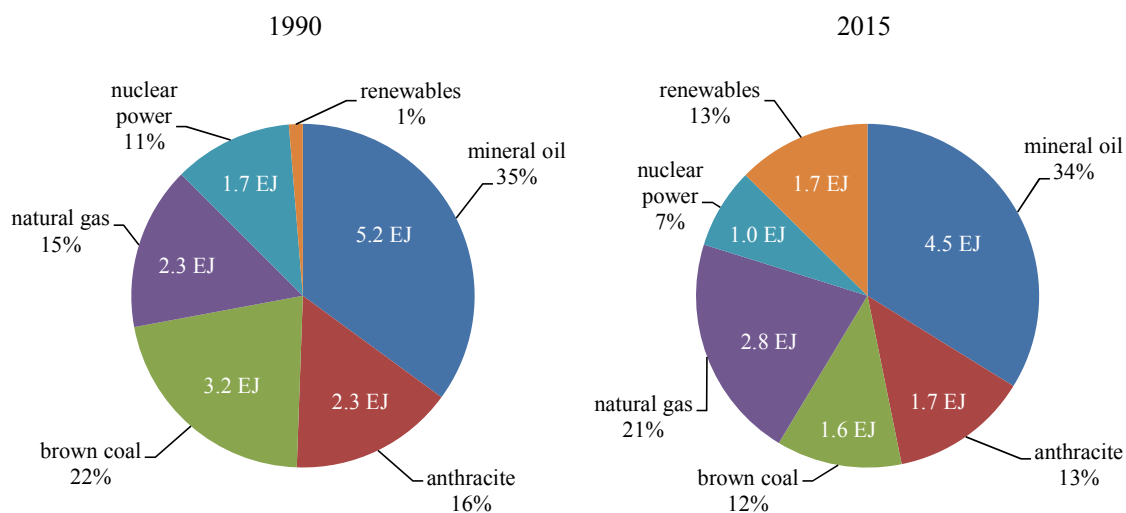


Figure 1: Comparison of the primary energy production of the FRG between 1990 and 2015. The renewable sector in 1990 produced 0.2×10^{18} J. ^[1]

The importance for new types of energy storage technologies becomes evident if looked upon the above mentioned three sectors of possible energy production. The key question is if the generated energy is in a storable form or if it needs to be converted for storage. Fossil and nuclear fuels have the advantage, that they can be stored for very long periods of time before they are converted into the type of energy of interest when needed. In the sector of renewable energy production, only hydroelectric energy, biomass and geothermal energy can be stored rather easily. Photovoltaic and wind energy on the other hand are being directly converted into electricity and suitable storage technologies are still in development. An example for a

different approach to convert solar radiation into electricity is realized in solar thermal power plants that can bridge timescales of hours using integrated latent heat storage units (e.g. Andasol complex, Granada, Spain).^[2] With missing energy storage technologies to use renewables effectively for base load energy production, the step from fossil fuels towards renewable energy will not be possible without a massive change of our lifestyle.

Roughly, the primary energy consumption can be divided in three major sectors; electrical energy, heat and mobility. Each of these sectors uses about one third of the primary energy if looked upon on a global scale.^[3] The technology for effective energy storage in each of these sectors requires totally different concepts as the type, amount and accessibility of the required energy varies not only between but also within the different sectors. For example, the heat needed for home heating has different requirements than the heat that is converted into electrical power in power plants as in the above mentioned example. It is quoted, that about 40% of the final energy consumption in the FRG is to generate low-temperature heat used primarily for room heating.^[4] Figure 2 shows the average energy consumption of private households in the FRG during 2015 without the mobility sector.^[5] Here it is visible, that 83% are used for room heating and production of warm water for general usage. This is an example for a possible application for a low-heat thermal energy storage system with a saving potential of about 1.9 EJ as the total annual solar energy on a single housing exceeds its energy demand for heating during the year.^[4]

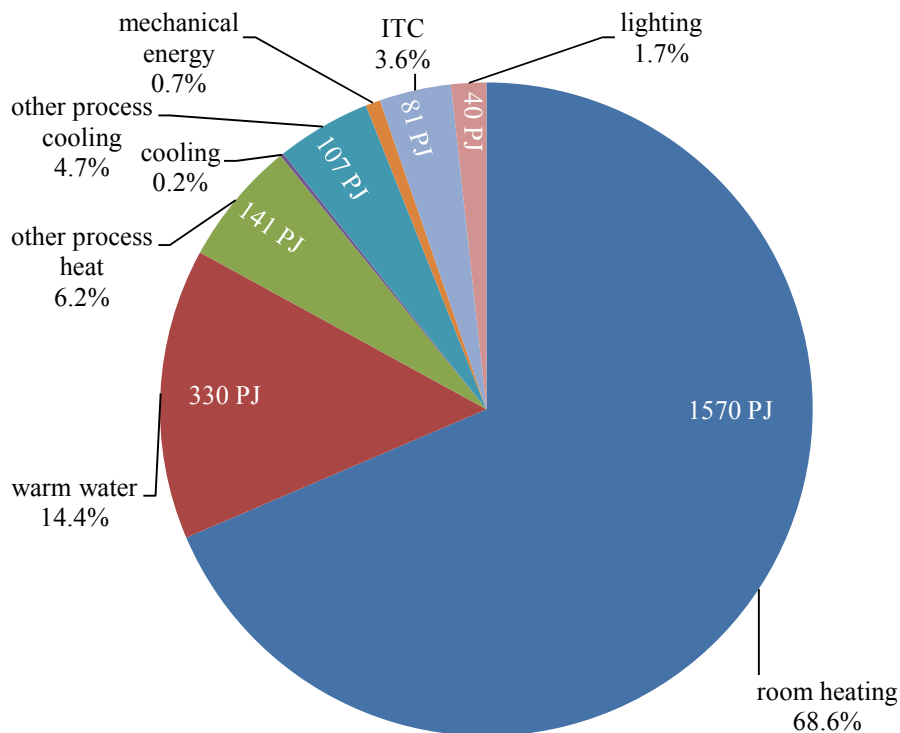


Figure 2: The average energy consumption of a private household in the FRG in 2015 without the mobility sector.^[5]

1.1 Thermal Storage Technologies

In the sector of thermal energy storage, various types of technologies exist which can be divided into being physical and chemical based. An overview about the types and properties are given in Table 1. The target is to make renewable energy more utilizable than it is today. This requires the buffering of energy availability peaks during daily cycles and the storage of excess energy during times of high availability (e.g. in summer) to periods when the demand (e.g. in winter) exceeds the supply (cf. Fig. 3). The most important parameters for thermal storages are the storage temperature and the storage density.

Of all storage technologies mentioned in Table 1, the storage of energy comes with a change in the inner energy of the storage medium. In sensible systems, the thermal energy is stored by increasing the thermal–kinetic part of the inner energy of the storage medium while latent systems use the thermal–potential part of the inner energy.^[6] Thermochemical energy storage uses the reversible energy that is consumed or released during the creation or breaking of physical or chemical bonds. Here the chemical part of the inner energy is increased. As the oxidation is irreversible, the energy is released by lowering the inner energy of the reaction products through breaking and rearranging very strong covalent bonds.

Table 1
Different types of energy storage.

	reversible			irreversible
	sensible	latent	thermochemical	oxidation
general principle	physical	physical	chemical	chemical
used storage property	heat capacity	phase change	Sorption, chemical reaction	chemical reaction
typical materials	water, concrete	paraffin, salt hydrates, salt	zeolites, salt hydrates	coal, oil, gas
storage temperature	273–373 K, water 273–773 K, concrete	273–343 K, paraffin 303–373 K, hydrates 373–673 K, salts	373–673 K, zeolites 273–573 K, hydrates	–
storage density	0.1–0.4 GJ m ⁻³	0.2–0.6 GJ m ⁻³	0.7–2.1 GJ m ⁻³	>32 GJ m ⁻³

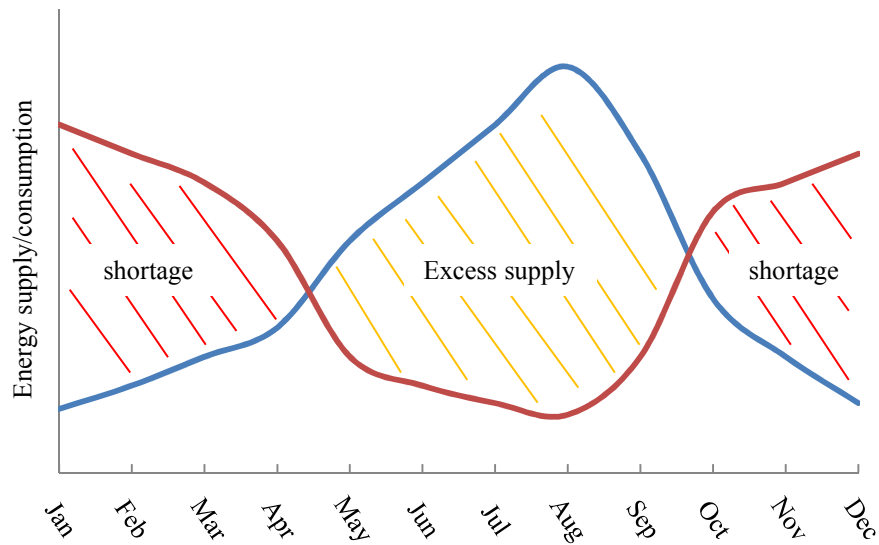


Figure 3: Schematic view over the available energy supply from solar radiation on private households in the northern hemisphere (blue line) in comparison to their energy consumption (red line). The yellow hatched area shows the duration of excess energy while the red hatched area shows the energy shortage.

The physical based thermal energy storage is split in two categories, sensible and latent. The sensible storage method is the oldest physical storage and most commonly used technique. During the storage, the energy is transferred as a direct heat flow to the material, where it is stored by keeping up the temperature gradient between the storage material and the surrounding. In this case, the storage capacity of the material is dependent on the heat capacity of the material itself as well as the temperature difference. On one hand, the capacity of the storage unit can be improved if the storage material has a high specific heat capacity and if a large temperature difference can be achieved. On the other hand, the temperature scale for the heat storage is limited by the transition points of the storage material. The most common material for sensible heat storage is water that has its transition temperatures between solid and liquid at 273 K and liquid and gaseous at 373 K. It is a very simple method for short term energy storage that can be accessed quickly but with increasing temperature gradients, complex insulation is required to prevent heat loss over longer periods of time. The specific heat capacity of water is $4.217 \text{ J g}^{-1} \text{ K}^{-1}$ at 273 K^[7] and assuming that the heat capacity remains constant with increasing temperature, heating the water from one transition point to the next by 100 K results in a stored amount of energy of about 0.4 GJ m^{-3} . For common household heating applications, the stored amount is more $0.2\text{--}0.3 \text{ GJ m}^{-3}$ as the temperature gradients cannot be that large. Compared with other heat storage techniques, it has a low energy density and in combination with the heat loss over long periods, it makes this technology only suitable for seasonal storage when large volumes are used to increase the volume–surface ratio of the storage tank. Conclusively, the advantages of this technology are fairly cheap storage materials (e.g. water or concrete) and the advanced state of development that already resulted in the construction of long term energy storage units.^[8] Major disadvantages are the relatively low energy storage capacity, variations in the temperature during a discharge (cf. Fig. 4a) and the inevitable heat loss during long storage periods.

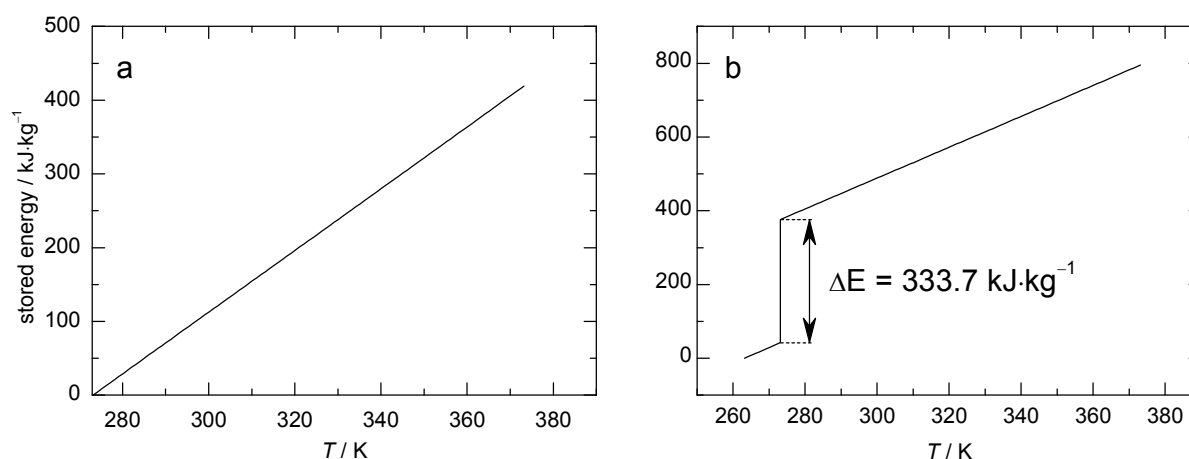
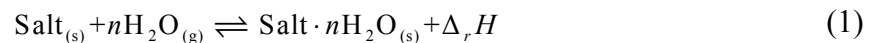


Figure 4: a) storage capacity of water used in a sensible heat storage if heated from 273 K to 373 K. b) latent heat of melting or freezing of water at 273 K.

The second physical storage technique is the latent heat storage. Here, the storage of heat is based on the heat exchange during the phase change of the material. The stored heat is called latent heat, because it is stored in the phase change which does not come with a change in temperature. Therefore, the materials used in latent heat storage are usually abbreviated as PCM (phase change material). The solid–liquid phase change is used, because even though for most substances the enthalpy of evaporation and the enthalpy of condensation in the liquid–gaseous phase change is significantly higher, the handling of the large changes in volume is technically difficult. Disadvantageous when using solids is their poor heat conductivity. A PCM for a heating application is charged, if the material is heated to its solid–liquid transition temperature. Any excess heat will be consumed until the complete melting of the material. The discharge is triggered by cooling the material below its transition temperature. The stored energy is then released upon the materials solidification. The latent heat equals the enthalpy of fusion or the enthalpy of crystallization (cf. Fig. 4b). Typical materials are various types of paraffin or crystalline hydrates of preferably congruently melting salts up to 400 K. Salt hydrates form a solution with their containing crystal water when they melt. These solutions show the tendency of supercooling where in some cases (e.g. $\text{CH}_3\text{COONa}\cdot 3\text{H}_2\text{O}$) the melt reaches ambient temperatures without recrystallization. Paraffin does not show supercooling behavior and the desired phase change temperature can be adjusted by various mixtures of different alkanes. If higher temperatures are required, other materials like anhydrous salts, namely nitrates and hydroxides (420 K–650 K) or chlorides, carbonates and fluorides (<670 K) can be selected. Usually, the heat storing properties are better if compared to sensible storage, e.g. $\text{NaOH}\cdot\text{H}_2\text{O}$ melts at 337 K and absorbs 272.1 kJ mol^{-1} of latent heat.^[9] Advantages of the latent storage are the higher energy density of about 0.58 GJ m^{-3} for the example of $\text{NaOH}\cdot\text{H}_2\text{O}$ and the relatively constant temperature during the phase transition. Problematic remains the need for thermal insulation if a long-term storage is desired and the tendency of some materials to supercool where they remain in a metastable state without releasing the latent heat.

The chemical based energy storage can be divided in two categories as well. On one hand, irreversible reactions, e.g. burning of fossil fuels, represent the largest fraction that is used for

primary energy production. The technology to transform the stored energy into heat, mechanical or electrical energy is very advanced. The release of its stored energy is based on the enthalpy of reaction during a redox reaction. An example would be the oxidation of fossil fuels like diesel. This reaction releases about 35.4 GJ mol^{-1} . On the other hand, thermochemical energy storage is based on reversible reactions like physisorption and chemisorption to store the energy in the formation of chemical bonds. The discharge takes place by breaking these “loose” bonds again. The formation of chemical bonds can store large amounts of energy and therefore the thermochemical energy storage has the highest theoretical storage density of the mentioned reversible heat storage types. Materials used for physisorption are highly porous materials with preferably small pore diameters in the micro (0.5–2 nm) and lower mesoporous (2–50 nm) size range. Problematic with physical sorbents (e.g. zeolites or silica gel) are the very high temperatures needed for a complete desorption in order to achieve a good storage density of 0.8 GJ m^{-3} .^[6] Salt hydrates are of interest as they show an even larger potential for a low potential heat storage application. Besides the rather low dehydration temperatures, high theoretical energy densities of more than 2 GJ m^{-3} are possible with many salt hydrates. In general, the charging and discharging reaction of a thermochemical storage unit using salt hydrates is shown in Eq. (1).



The discharge of the storage material is shown by the reaction from left to right. The hydration reaction is started by adding water vapor. The released enthalpy of reaction $\Delta_r H$ consists of the enthalpy of condensation ($\Delta_{\text{con}}H$) and the enthalpy of hydration ($\Delta_{\text{hyd}}H$). The needed energy for the charging can be obtained from renewable energy sources, e.g. solar heat. This way, the storage material is charged by adding $\Delta_r H$ being composed of the enthalpy of evaporation and the enthalpy of dehydration. A major advantage of this method is that both educts of Eq. (1) are in different states, solid and gaseous. This fact makes them easily separable and while the anhydrous salt cannot engage the back reaction without present water vapor, the substances loaded with a large amount of energy can be stored for transportation or even over long periods of time, as long as both reaction partners stay separated.^[10] The long-term storage can be separated in 3 stages, charging, storing and discharging, shown in Figure 5. In case of a salt hydrate, the hydrated phase is shown as AB. By spending energy, the salt is dehydrated to a lower hydrate or even the anhydrate B and the water vapor released. The solid anhydrate can be stored for long periods of time while it is separated from water vapor. If the stored energy needs to be released, rejoining the anhydrate with water vapor will trigger the exothermic hydration reaction and release the previously stored enthalpy of reaction $\Delta_r H$.

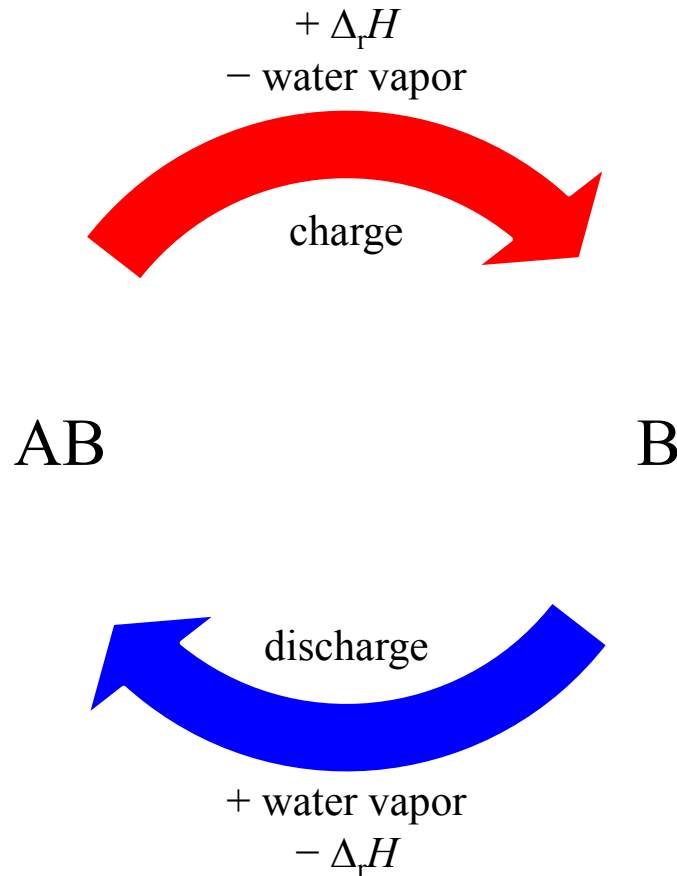


Figure 5: The three stages in a thermochemical storage cycle: charging, storing and discharging.

1.2 Materials for Thermal Energy Storage

Depending on the desired operational temperature of the storage unit, various materials exist to realize a thermochemical based heat storage.^[9,11] In this thesis, only salt hydrates with the sulfate ion in common will be in the focus of investigation. In a recent study on thermochemical materials (TCMs), a screening of a large amount of different hydrates with a fixed program for a special application has been carried out.^[12] This way, a large number of materials could be scanned, but as fruitful as this study is for the single application, the transferability of its results to other working conditions will rarely be possible. The simplest way for the reaction shown in Eq. (1) has two operational parameters, the water vapor partial pressure and the temperature. This study focusses on the target to create a comprehensive view on the thermodynamic properties of the three possible TCMs and a characterization that also other fields of research can use its results. Examples are given in the respective chapter introductions.

The comprehensive view is combined in a relative humidity (φ) versus temperature phase diagram of the available hydrates in the investigated temperature range of the system. An example is given in Figure 6 for the previously investigated system of $\text{MgSO}_4\text{-H}_2\text{O}$.^[13]

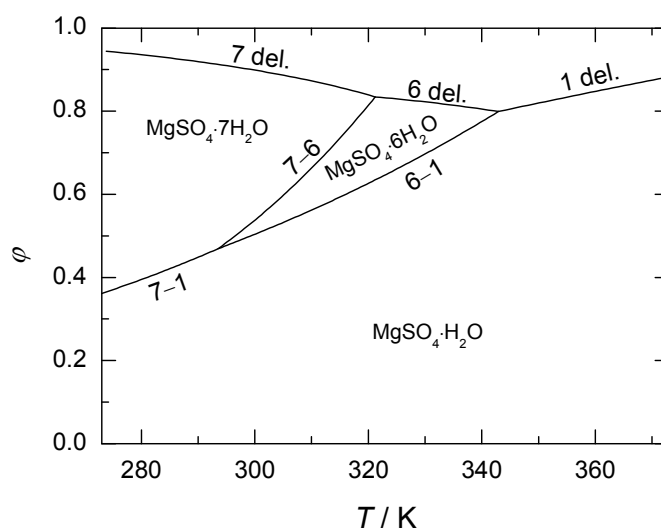


Figure 6: Calculated phase boundaries in the system $\text{MgSO}_4\text{-H}_2\text{O}$ from 273 K to 373 K.^[13] Solid lines represent deliquescence humidities of $\text{MgSO}_4\cdot 7\text{H}_2\text{O}$ (denoted as 7 del.), $\text{MgSO}_4\cdot 6\text{H}_2\text{O}$ (6 del.) and $\text{MgSO}_4\cdot \text{H}_2\text{O}$ (1 del.) and phase boundaries of $\text{MgSO}_4\cdot 7\text{H}_2\text{O}\text{-MgSO}_4\cdot \text{H}_2\text{O}$ (7-1), $\text{MgSO}_4\cdot 7\text{H}_2\text{O}\text{-MgSO}_4\cdot 6\text{H}_2\text{O}$ (7-6) and $\text{MgSO}_4\cdot 6\text{H}_2\text{O}\text{-MgSO}_4\cdot \text{H}_2\text{O}$ (6-1). Phase stability fields are marked with $\text{MgSO}_4\cdot n\text{H}_2\text{O}$ ($n = 7, 6, 1$).

With such phase diagrams, it is possible to determine the values, thermodynamically required for the operational parameters, water vapor pressure and temperature, to enable the desired hydration reaction. Additionally, it also shows the maximum reaction temperatures and the margin of variability for the parameters to enable further optimization of the reaction kinetics without risking unwanted side reactions like the deliquescence of a present phase.

Besides the optimal reaction conditions from a thermodynamic point of view, the discharge of the storage material needs to be fast. Therefore, not only the reaction has to be quick but the generated heat has to be transported away from the reaction site. A promising way to increase the reaction kinetics is to embed the salt in an open-porous matrix to create a composite material that offers a very large reaction surface^[9] but also improves the thermal conductivity of the material at the reaction site.^[10] Numerous studies^[4,14,15] continued investigating this approach, but as promising a composite material is, it also encounters an old problem that becomes visible when salts are brought into porous media. Especially in the field of cultural heritage but also in modern construction, salts inside the porous building material can pose a challenge when certain climatic conditions are met. An example about the destructive potential of salt hydrates is shown in Figure 7 where a sandstone, impregnated with anhydrous Na_2SO_4 is exposed to a cooled, saturated Na_2SO_4 solution.^[16] This provokes the crystallization of $\text{Na}_2\text{SO}_4\cdot 10\text{H}_2\text{O}$ from a supersaturated solution generating stress in the material that results in its destruction.

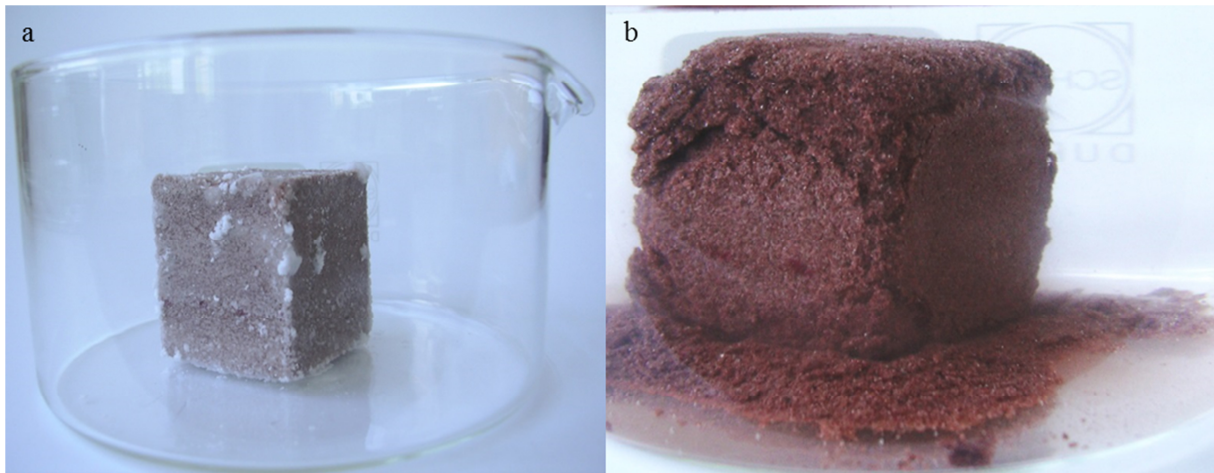


Figure 7: Damage potential of $\text{Na}_2\text{SO}_4 \cdot 10\text{H}_2\text{O}$ in natural sandstone (Ebenheider Sandstein). a) shows the sandstone impregnated with Na_2SO_4 at the beginning of the experiment. b) depicts the result after exposing the pretreated stone for 2 h to a cooled, saturated Na_2SO_4 solution.^[16]

An absolute measurement of the capability of salt hydrates to generate pressure through a hydration reaction, note that Figure 7 shows the different dissolution–recrystallization reaction mechanism, has not been performed up to this day. Furthermore, the ability of salts to generate pressure through a solid–gas hydration reaction is questioned.^[17] In an attempt to add the third variable of pressure, this work focused on the development of a method to measure the absolute pressure resistance of hydrates at defined climatic conditions before a dehydration reaction takes place. The importance results from the fact that the surfaces of crystals, growing in a porous media and build up pressure against the pore wall, are under anisotropic pressure themselves. Hence the crystal can only generate the amount of pressure it is able to resist itself. The increased pressure itself affects the phase diagram and the conditions for a phase change shift to other temperatures and relative humidities and therefore the operational parameters of the storage unit. The theoretical calculations for the crystallization and hydration pressure based on the solution properties and the dissociation humidities that can be calculated with the equations provided by this work, respectively, can be performed with existing equations.^[18]

The destructive potential of salt hydrates clarifies the necessity of a precise knowledge about the phase change behavior of the used storage material inside the composite at varying temperature, water vapor pressure and pressure on the crystal surfaces. Even if the hydration reaction does not generate a pressure, large enough to damage the porous host material, the possibility of a deliquescence–recrystallization reaction must be prevented in order to sustain the composite material and therefore the storage unit’s operability.

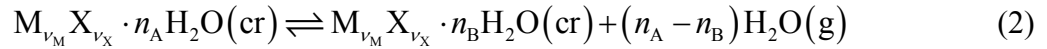
1.3 Aim

In order to determine the suitability of a salt hydrate as a thermochemical material for heating applications, different approaches exist. This work focusses on the fundamental equilibrium states in each investigated system at least between 273 K and 373 K. At this moment, none or only contrary phase diagrams for each hydrate exist. The aim of this study is to understand the phase change behavior in detail over the mentioned temperature range at various relative humidities including both stable and metastable equilibria as well as the stability fields of the investigated phases. As the ongoing research about thermochemical storage materials continues to focus on composite materials, additional information about the influence of anisotropic stress on the crystals is needed. The gained information about the salt hydrates should be treated as a basis for a heat storage system that can fulfill the annual heat demand in a household.

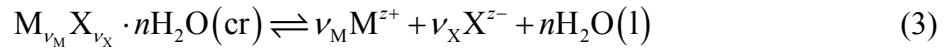
Comprehensive phase diagrams were established in this work in the following way. Solution properties are used together with the Pitzer ion interaction model to establish the parameters for the calculation of solution properties over a large range of temperature and concentration. Solubility data of the investigated phases provided the basis for the determination of the respective solubility products. The database is then supplemented with dissociation humidities to substantiate the phase boundaries in both stable and metastable ranges. This groundwork will give continuative studies in the sector of thermochemical energy storage the opportunity to estimate optimal operation parameters for its intended application for the Systems of $\text{ZnSO}_4\text{-H}_2\text{O}$, $\text{CuSO}_4\text{-H}_2\text{O}$ and $\text{CaSO}_4\text{-H}_2\text{O}$.

2 Theory and Equations

As this work focuses on the equilibria of hydration and dehydration reactions, this chapter will walk through the thermodynamic fundamentals. Depending on the surrounding climate conditions, temperature and relative humidity, certain salts can incorporate water from the gaseous phase into their crystal lattice. For any salt hydrate of a general composition $M_{v_M}X_{v_X} \cdot nH_2O$ with v_M cations and v_X anions and n molecules of water, the equilibrium reaction between the two solids can be described by



Next to the solid–vapor equilibrium, the formation of a solution can take place if the relative humidity is increased to the deliquescence humidity of the given hydrate. In this case, the solid absorbs water from the gaseous phase to form a saturated solution. This dissolution reaction for a hydrate can be described by



If the relative humidity is kept above the deliquescence humidity, a dilution of the solution will take place.

These phase boundaries between the solid hydrate phases, the liquid solution and the gaseous phase can be visualized in a ϕ vs. T diagram as will be done in the following chapters.

2.1 Phase Diagrams

ϕ vs T phase diagrams are a very useful tool for a quick overview about the pictured system. Figure 8 shows an exemplary phase diagram that displays the phase boundaries of a system $MX-H_2O$ between the solid hydrate $MX \cdot nH_2O$ (A) and the anhydrous phase MX (B) as well as the liquid solution (C).

In the two diagrams, different patterns show the expected reaction pathways in a reaction vessel and the resulting phases. The example in the left diagram follows the pattern between the points I to V. Starting material is the hydrated phase (A), which is stable at the starting conditions at point I. Increasing the relative humidity ϕ to point II does not result in a reaction when line b' is crossed as phase (B) is not present in the reaction vessel. A further increase of the relative humidity raises ϕ in the vessel above the deliquescence humidity of phase (A). The surrounding conditions are now in the stability field of (C); hence the dissolution of (A) and the formation of a solution will take place. So far, the reactor was operated at isothermal conditions. If the temperature is increased at constant ϕ to point IV, the state of a solution will remain but if ϕ is reduced to point V, the deliquescence humidity of (B) is crossed. The solution is then metastable with respect to phase (B); hence the water will evaporate and the crystallization of phase (B) takes place.

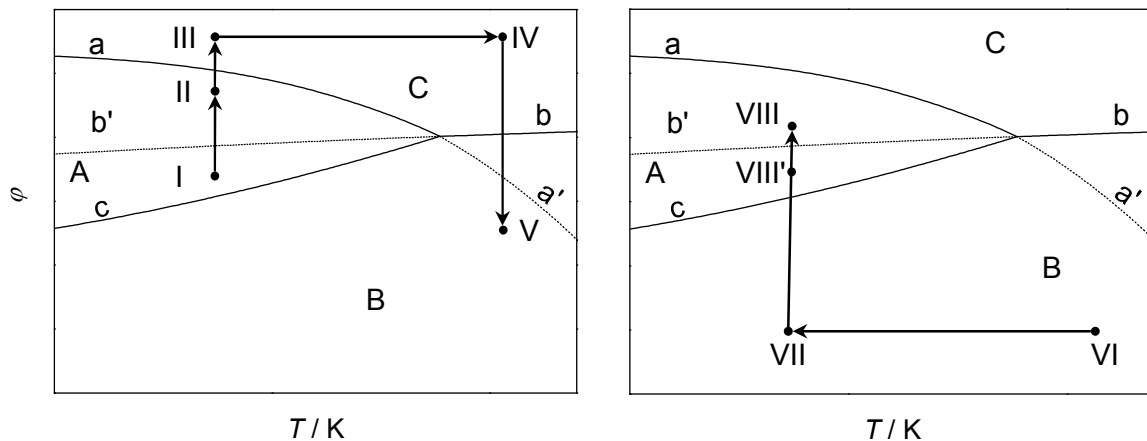


Figure 8: Exemplary phase diagram of a random system $\text{MX-H}_2\text{O}$.

The second example, shown in the right hand diagram of Figure 8, focusses on the operating conditions of a thermochemical storage material during seasonal heat storage as shown in Figure 5. Starting with the hydrated phase (A) and increasing the temperature to point VI will cause the dehydration of the material to phase (B). During this process, the heat is stored in the salt by breaking the bonds and evaporating the water. If both reaction products are separated, the anhydrous salt can be cooled to ambient temperature at point VII. The only heat loss in the process is through the actual cooling whereas the energy content of the material remains constant. Discharging the storage is done by increasing φ to the optimal working conditions, shown as point VIII. By crossing the lines c and b' , the solid–gas hydration reaction and the solid–liquid deliquescence–recrystallization are induced respectively. As the reaction will generate heat, the temperature in the reaction vessel will increase and the conditions will shift to the right. With closing in on the phase boundaries a or c , the reaction will become slower and finally stop when one of the two is reached. Therefore, the phase boundaries a and c mark the maximum working conditions for operating this system and the intersection of a , b and c gives the highest theoretically possible operating temperature for the system as the hydrate (A) is not stable above that temperature. Once the storage unit is exhausted, the temperature will decrease to ambient level and the remaining humidity needs to be separated to prevent condensation in the reaction vessel. After that, the storage unit is fully discharged and can be recharged by increasing the temperature back to point VI.

To identify the optimal temperature rise possible for each investigated material, it is crucial to know the location of lines similar to b' from this example. If φ is not raised from VII to VIII but only to VIII', the reaction mechanism will not be of the dissolution–recrystallization kind but only hydration. The first mechanism has much faster reaction kinetics but the material will enter the liquid phase in the process. Once the dissolution of (B) has started, the recrystallization of (A) will occur as the formed solution of (B) is supersaturated with respect to (A). The lifespan of the liquid phase should be kept very short as it can also result in the generation of stress on the porous host when the crystals grow against the pore walls. Hence, the structure of the host can be damaged in the process. Additionally, the distribution in the porous matrix can change as the salt is mobilized by the formation of a solution that results in a reduction of

the materials capability to undergo cycling. As some pores might even get clogged in the event, the storage density of the composite will decline as well. Especially the latter part of the second example points out the necessity of a precise knowledge of the phase boundaries in a system.

2.2 Thermodynamics of Electrolyte Solutions

An ideal solution can be characterized by neglecting the interactions between the dissolved species and with the solvent molecules. This assumption is only valid at very small concentrations of the dissolved species. Raoult's law describes the ideal solution as where the partial vapor pressure p_i of substance i above the solution is directly proportional to the molar fraction of the dissolved species x_i and the vapor pressure of the pure substance p_i^0 :

$$p_i = x_i p_i^0 \quad (4)$$

Electrolyte solutions only follow Eq. (4) in a very dilute state. To describe the real behavior of an aqueous solution, both interactions between the dissolved species themselves as well as the solute and the solvent need to be considered. Instead of using the concentration of the dissolved substances, the activity a is used. For the solute, the activity is defined as

$$a_i = \gamma_i m_i / m^\circ \quad (5)$$

where m_i is the concentration, γ_i is the activity coefficient and m° is the standard concentration. The standard concentration is defined as a hypothetical state, where all interactions that would result in a deviation of the ideal behavior are excluded. It is defined as $m = 1 \text{ mol kg}^{-1}$. In the case of infinite dilution, the activity equals the concentration and this results in an activity coefficient of $\gamma_i = 1$ (cf. Eq. (5)).

In addition to the activity a_i of the dissolved species i , the activity of the solvent has to be defined. As this work deals only with aqueous solutions, the water activity a_w is defined as

$$RT \ln a_w = \mu_w(l) - \mu_w^\circ(l) \quad (6)$$

with the universal gas constant R , the absolute temperature T , the chemical potential of water in the solution $\mu_w(l)$ and the chemical potential of pure water $\mu_w^\circ(l)$.^[19] Pure water, which is in equilibrium with the water vapor above it, can be defined as

$$\mu_w^\circ(l) = \mu_w^\circ(g) = \mu_w^\circ + RT \ln f_w^0 / p^\circ \quad (7)$$

The chemical potential of pure water vapor and water in standard state are given by $\mu_w^\circ(g)$ and μ_w° respectively. The fugacity is defined as $f = \gamma_f p$, where γ_f is the fugacity coefficient that corrects the deviation of the gas to the ideal behavior and p is the pressure of the gas. In Eq. (7), f_w^0 is the saturation fugacity of pure water and p° refers to a standard pressure of 10^5 Pa . Corresponding to Eq. (7), the chemical potential of water in a solution $\mu_w(l)$ is given by

$$\mu_w(l) = \mu_w(g) = \mu_w^\circ + RT \ln f_w / p^\circ \quad (8)$$

Hence, the chemical potential of water in a solution $\mu_w(l)$ is in equilibrium with the water vapor above a solution $\mu_w(g)$ when the fugacity f_w reaches a certain value at a defined temperature T . Insertion of Eqs. (7) and (8) in Eq. (6) and by solving for a_w simplifies to

$$a_w = f_w/f_w^0 \quad (9)$$

and if the water vapor above a solution is considered as an ideal gas, the fugacity coefficients γ_f can be presumed as 1. This allows transforming Eq. (9) to

$$a_w = p_w/p_w^0 = \varphi \quad (10)$$

where the water activity is defined as the quotient of the partial water vapor pressure above the solution and the saturation water vapor pressure of pure water. Hence, if ideal behavior of the gaseous phase above the solution is assumed, the water activity of the solution equals the relative humidity above the solution. If the water activity of a solution needs to be calculated with very high precision, e.g. from direct water vapor pressure measurements, it is necessary to correct the non-ideal behavior of water vapor and the pressure dependency of the water activity. The procedure without the necessity of the fugacity coefficient is described in the work of Rard and Platford.^[20]

This correction is required, if the water activity of a solution is expressed as the osmotic coefficient ϕ because the logarithmic relationship requires values of very high accuracy (cf. Eq (11)).

$$\ln a_w = -(\phi/m_w) \sum_i m_i \quad (11)$$

Here, $m_w = 55.50844 \text{ mol kg}^{-1}$, is the molality of water, m_i the molality of ion i and i covers all solute species. The logarithmic relationship between the osmotic coefficient and the water activity enables to show even small deviations from ideal behavior provided that the measurement of the water activity is very accurate.

In addition to activity coefficients and osmotic coefficients, there is interest in the enthalpy and heat capacity for a further characterization of electrolyte solutions. These quantities describe the temperature dependent behavior of the excess Gibbs energy. In this chapter, the quantities will be introduced shortly, while in the following chapter 2.3 a more detailed view on the connections is given.

A partial molar quantity of a substance i is defined as

$$J_{m,i} = (\partial J / \partial n_i)_{p,T,n_j} \quad (12)$$

with constant pressure, temperature and amounts of the substance j . Therefore it is the effective quantity of i in a mixture with j and differs from that of the pure substance i . The absolute amount of J for a mixture is given by the sum of all partial molar quantities and is described by

$$J=J_{m,i}n_i+J_{m,j}n_j \quad (13)$$

J and n are the partial molar quantities and amounts of the substances i and j respectively. The partial molar Gibbs energy, commonly known as the chemical potential is defined in analogy with Eq. (12) as

$$\mu_i=(\partial G/\partial n_i)_{p,T,n_j} \quad (14)$$

and gives the change in Gibbs energy G with varying amount of substance. The Gibbs energy of a mixture of substances i and j can, according to Eq. (13), be calculated by

$$G=\mu_i n_i+\mu_j n_j \quad (15)$$

The above mentioned excess quantities will be expressed as apparent molar quantities.^[21] For electrolyte solutions are mixtures, it has to be defined what ratio is given by the solvent (index 1) and what by the solute (index 2). The general definition of an apparent molar quantity ${}^\phi J_2$ is given by

$${}^\phi J_2=(J-J^\circ)/n_2=(J-n_1 J_{m,1}^\circ)/n_2 \quad (16)$$

Here, J is the measured quantity and J° the part of the pure solvent. n_1 and n_2 represent the amounts of substance of the solvent and the solute, respectively, while $J_{m,1}^\circ$ is the partial molar quantity of the pure solvent.

The relative partial molar enthalpy $L_{m,i}$ of a component i is defined as the difference between the partial molar enthalpy $H_{m,i}$ and the standard state partial molar enthalpy $H_{m,i}^\circ$ of component i , $L_{m,i}=H_{m,i}-H_{m,i}^\circ$. The standard state of an electrolyte solution is defined as the state at infinite solution, what corresponds to an ideal solution. This results in the apparent molar enthalpy showing the difference between the real and ideal solution, hence it equals zero at infinite dilution.

The relative apparent molar enthalpy ${}^\phi L_2$ is the part of the electrolyte and can be expressed in analogy to Eq. (16) by

$${}^\phi L_2=(L-L^\circ)/n_2=L/n_2 \quad (17)$$

For the apparent molar enthalpy of the solvent L° equals zero, the relation between the relative apparent molar enthalpy ${}^\phi L_2$ and the relative enthalpy L is quite simple.

As mentioned above, next to the relative apparent molar enthalpies, apparent molar heat capacities ${}^\phi C_p$ are important for the characterization of electrolyte solutions and they are defined by

$${}^\phi C_p=(C_p-C_p^\circ)/n_2=(C_p-n_1 C_{p,m}^\circ)/n_2 \quad (18)$$

C_p is the heat capacity of the solution and C_p° and $C_{p,m}^\circ$ the heat capacity and the partial molar heat capacity of the solvent, respectively. According to Eq. (18), the apparent molar heat

capacity ${}^\phi C_p$ requires the heat capacity of the mixed solution and the partial molar heat capacity of the pure solvent $C_{p,m}^\circ$, in this case water. In general, this work uses the equation of Wagner and Pruß^[7] for the calculation of $C_{p,m}^\circ$ of water with the exception in chapter 4.4.1, where the IAPWS-IF97^[22] formulation is used.

2.3 The Ion Interaction Approach

To describe the properties of electrolyte solutions, both short-range ion-ion and ion-solute as well as long-range coulombic interactions have to be considered. The long-range interactions between cation and anion and the resulting deviation from the ideal behavior are commonly derived using the Debye-Hückel limiting law. For these interactions are nonspecific, it is generally applicable but limited to very dilute solutions only. With increasing concentration, the influence of specific short-range interactions predominates. Hence, in order to predict the real behavior of solutions with higher concentrations, a model considering both long-range and short-range interactions is required. The ion interaction approach developed by Pitzer^[23] has been successfully employed to represent data within the margin of experimental error for single and mixed electrolyte solutions.

The ion interaction approach of Pitzer, often briefly called the “Pitzer model”, claims to describe the properties of electrolyte solutions using simple equations that concur with the basic principles of thermodynamics and statistical mechanics. In addition, and this is its real advantage, it is possible to predict the properties of complex mixed systems containing multiple ions that have not been measured directly. The requirements to do so are parameterizations for the binary and ternary systems containing the desired ions. Hence, it is necessary to have precise knowledge of binary systems consisting of a pure salt and water, and if required, ternary systems containing two salts with one common ion and water. Ternary or more complex systems will not be calculated in this work and are therefore just briefly mentioned.

The Pitzer equations need to describe both the long-range and short-range ion interactions. The nonspecific long-range interactions are represented using an extended form of the Debye-Hückel limiting law. For it is nonspecific, it is mainly affected by the ionic strength I . On the other side, the specific short-range interactions need to be determined for each species separately. They are expressed by the second and third virial coefficients, where the second virial coefficient describes the short-range interactions between two ions and is dependent on the ionic strength, while the third virial coefficient describes the interactions between three ions omitting the ionic strength dependency. In general it would be possible to extend the equation to higher order ionic strength dependency^[24] and coefficients^[25] but they are usually neglected for their small influence. For it is a molality based model, additional advantages are that molalities are independent of pressure and temperature in contrast to molarities but limitations occur at highly concentrated solutions.

The general equation is based on the Gibbs excess energy G^{ex} , a quantity that is simply defined as the difference between a real and an ideal solution, with a series of terms that increase in powers of molality and is expressed by

$$G^{\text{ex}}/(w_w RT) = f(I) + \sum_i \sum_j m_i m_j \lambda_{ij}(I) + \sum_i \sum_j \sum_k m_i m_j m_k \mu_{ijk} \quad (19)$$

where w_w is the mass of water in kg, R the gas constant and T the temperature. $f(I)$ represents the coulombic long-range interactions (Debye-Hückel term) and m_i , m_j and m_k the molalities of the dissolved species in mol kg⁻¹. The ionic strength, I , is defined as

$$I = \frac{1}{2} \sum_i m_i z_i^2 \quad (20)$$

with z_i giving the charge of species i . λ_{ij} symbolizes the second virial coefficient and defines the short-range interactions between the two species i and j . It is dependent on pressure, temperature and in this case on the ionic strength. The third virial coefficient μ_{ijk} can be described similar as it defines the short-range interactions involving three species i , j and k . An ionic strength dependency would be expected but in most cases it was not observed and therefore will be neglected in this work.

The relation between the osmotic coefficient, the activity coefficient of species i and the excess Gibbs energy is expressed by

$$G^{\text{ex}}/w_w = RT \sum_i m_i (1 - \phi + \ln \gamma_i) \quad (21)$$

For pure electrolytes, Pitzer defines the osmotic coefficient as

$$\phi - 1 = (vm)^{-1} \left\{ \begin{aligned} & (If' - f) + m^2 \left[2v_M v_X (\lambda_{MX} + I\lambda'_{MX}) + 2v_M^2 (\lambda_{MM} + I\lambda'_{MM}) \right] \\ & + 2v_X^2 (\lambda_{XX} + I\lambda'_{XX}) \\ & + m^3 (6v_M^2 v_X \mu_{MMX} + 6v_M v_X^2 \mu_{MXX} + 2v_M^3 \mu_{MMM} + 2v_X^3 \mu_{XXX}) + \dots \end{aligned} \right\} \quad (22)$$

From experimentally measured properties for an electrolyte with cation M and anion X, it is only possible to evaluate the bracketed terms of λ as a function of ionic strength and the final term in parentheses for μ . Therefore Pitzer defined the Debye-Hückel term ($If' - f$) and the second and third virial coefficient as f^ϕ , $B^\phi(I)$ and C^ϕ respectively.^[23]

$$f^\phi = (f' - f/I)/2 = -A_\phi I^{1/2} / (1 + bI^{1/2}) \quad (23)$$

$$B_{MX}^\phi = \lambda_{MX} + I\lambda'_{MX} + (v_M/2v_X)(\lambda_{MM} + I\lambda'_{MM}) + (v_X/2v_M)(\lambda_{XX} + I\lambda'_{XX}) \quad (24)$$

$$C_{MX}^\phi = \left[3/(v_M v_X)^{1/2} \right] (v_M \mu_{MMX} + v_X \mu_{MXX}) \quad (25)$$

The Pitzer approach gives expressions for the osmotic coefficient ϕ and mean activity coefficient γ_\pm for binary electrolyte solutions as^[23]

$$(\phi - 1) = -|z_M z_X| A_\phi \frac{I^{1/2}}{(1 + bI^{1/2})} + 2m \frac{v_M v_X}{v} B_{MX}^\phi + 2m^2 \frac{(v_M v_X)^{3/2}}{v} C_{MX}^\phi \quad (26)$$

and

$$\ln \gamma_{\pm} = -|z_M z_X| A_{\phi} \left[\frac{I^{1/2}}{(1+bI^{1/2})} + \frac{2}{b} \ln(1+bI^{1/2}) \right] + 2m \frac{\nu_M \nu_X}{\nu} B_{MX}^{\gamma} + 2m^2 \frac{(\nu_M \nu_X)^{3/2}}{\nu} C_{MX}^{\gamma} \quad (27)$$

where z_M and z_X are the charges and ν_M and ν_X are the stoichiometric coefficients of the cation M and the anion X respectively. A_{ϕ} is the Debye-Hückel parameter for the osmotic coefficient and b is a universal parameter set to $1.2 \text{ mol}^{1/2} \text{ kg}^{-1/2}$. The second and third virial coefficients, λ_{ij} and μ_{ijk} , are expressed as the experimentally determinable quantities B_{MX} and C_{MX} . The mean activity coefficient is defined as

$$\ln \gamma_{\pm} = (\nu_M \ln \gamma_M + \nu_X \ln \gamma_X) / \nu \quad (28)$$

with $\nu = \nu_M + \nu_X$.

Values for the Debye-Hückel parameter A_{ϕ} used in this work were taken from Archer and Wang.^[26] For the solutions of this work are not under pressure, the pressure dependency for A_{ϕ} is not required and its temperature dependency at 0.1 MPa can be described by Eq. (29).^[27]

$$A_{\phi} = a_1 + a_2 T_0 / (T - 222\text{K}) + a_3 T_0^2 / T^2 + a_4 T / T_0 + a_5 T^2 / T_0^2 + a_6 T^4 / T_0^4 \quad (29)$$

The second virial coefficient B_{MX} represents the short-range interactions between two ions. For cation M and anion X, this yields interactions between the three pairs MM, MX and XX. Its ionic strength dependency is given by Eq. (29) but it has to be mentioned, that this written equation is an extended form of Pitzers original equation^[23], where the $\beta_{MX}^{(2)}$ term was introduced only for 2–2 electrolytes to avoid the calculation of association equilibria with a fixed value for $\alpha_2 = 12 \text{ kg}^{1/2} \text{ mol}^{-1/2}$.^[28] Later, Filippov et al.^[29] found an enhancement in the numerical flexibility at higher concentrations as it is mentioned by Steiger et al.^[27] Therefore, this work uses the extended form of Pitzers original equations as introduced by Steiger et al.^[27]

$$B_{MX}^{\phi} = \beta_{MX}^{(0)} + \beta_{MX}^{(1)} \exp(-\alpha_{MX}^{(1)} I^{1/2}) + \beta_{MX}^{(2)} \exp(-\alpha_{MX}^{(2)} I^{1/2}) + \beta_{MX}^{(3)} \exp(-\alpha_{MX}^{(3)} I^{1/2}) \quad (30)$$

$$B_{MX} = \beta_{MX}^{(0)} + \beta_{MX}^{(1)} g(\alpha_{MX}^{(1)} I^{1/2}) + \beta_{MX}^{(2)} g(\alpha_{MX}^{(2)} I^{1/2}) + \beta_{MX}^{(3)} g(\alpha_{MX}^{(3)} I^{1/2}) \quad (31)$$

$$B'_{MX} = 1/I \left[\beta_{MX}^{(1)} g'(\alpha_{MX}^{(1)} I^{1/2}) + \beta_{MX}^{(2)} g'(\alpha_{MX}^{(2)} I^{1/2}) + \beta_{MX}^{(3)} g'(\alpha_{MX}^{(3)} I^{1/2}) \right] \quad (32)$$

The functions g and g' are defined as

$$g(x) = 2/x^2 \left[1 - (1+x) \exp(-x) \right] \quad (33)$$

$$g'(x) = -2/x^2 \left[1 - (1+x+x^2/2) \exp(-x) \right] \quad (34)$$

with $x = \alpha_{MX} I^{1/2}$ for each $\alpha_{MX}^{(i)}$ and $\beta_{MX}^{(i)}$. Pitzer^[23] suggests fixed values for the numerical constants of $\alpha_1 = 1.4 \text{ kg}^{1/2} \text{ mol}^{-1/2}$ and $\alpha_2 = 12 \text{ kg}^{1/2} \text{ mol}^{-1/2}$ for 2–2 electrolytes at 298.15 K. In this work, using the extended set of equations^[27], individually assigned values for each $\alpha_{MX}^{(i)}$

are determined. The additional term of $\beta_{MX}^{(3)}$ with $\alpha_{MX}^{(3)}$ is used when found necessary to improve the data representation.

The third virial coefficient C_{MX} represents the short-range interactions between three particles yielding the possible interactions of MMM, MMX, MXX and XXX. Since electrical repulsions minimize the chance that three ions of the same sign are often close together, the terms for MMM and XXX are expected very small, hence they were neglected.^[23] In this work, values for C_{MX} are tabulated as C_{MX}^ϕ and their relationship is shown by

$$C_{MX} = C_{MX}^\phi / 2 |z_M z_X|^{1/2} \quad (35)$$

$\beta_{MX}^{(0)}$, $\beta_{MX}^{(1)}$, $\beta_{MX}^{(2)}$, $\beta_{MX}^{(3)}$ and C_{MX}^ϕ are referred to as the binary interaction parameters of a salt MX that are dependent on temperature and pressure and have to be determined for every binary system individually from experimental data. This work solely deals with systems that are under atmospheric pressure and therefore only the dependence on temperature will be exemplified.

A great advantage of a consistent parameterization is the possibility to calculate the properties of electrolyte solutions at different temperatures that have not been directly measured. Of course the parameters for each investigated system have to be adjusted to the desired temperature range. This can be done using osmotic and activity coefficients at various temperatures, if available, and in addition with thermochemical data like enthalpies or heat capacities to further increase the internal consistency of the determined parameters. The relation of the enthalpy to the excess Gibbs energy, G^{ex} , is given by

$$L = -T^2 \left(\frac{\partial(G^{ex}/T)}{\partial T} \right)_{p,m} \quad (36)$$

Eq. (21) with the derivations of Eq. (36) yield the relative apparent molar enthalpy ${}^\phi L$ for a binary electrolyte system

$${}^\phi L = \nu |z_M z_X| \frac{A_L}{2b} \ln(1 + bI^{1/2}) - 2\nu_M \nu_X RT^2 [mB_{MX}^L + m^2 (\nu_M z_X) C_{MX}^L] \quad (37)$$

where the quantities A_L , B_{MX}^L and C_{MX}^L are given by

$$A_L = 4RT^2 \left(\frac{\partial A_\phi}{\partial T} \right)_p \quad (38)$$

$$B_{MX}^L = \left(\frac{\partial B_{MX}}{\partial T} \right)_{p,I} = \beta_{MX}^{(0)L} + \beta_{MX}^{(1)L} g(\alpha_{MX}^{(1)} I^{1/2}) + \beta_{MX}^{(2)L} g(\alpha_{MX}^{(2)} I^{1/2}) + \beta_{MX}^{(3)L} g(\alpha_{MX}^{(3)} I^{1/2}) \quad (39)$$

$$\beta_{MX}^{(i)L} = \left(\frac{\partial \beta_{MX}^{(i)}}{\partial T} \right)_p, \quad i = 0, 1, 2, 3 \quad (40)$$

and

$$C_{MX}^L = \left(\frac{\partial C_{MX}}{\partial T} \right)_p \quad (41)$$

Eqs. (39) and (41) show, that the coefficients B_{MX}^L and C_{MX}^L are the first derivatives of B_{MX} and C_{MX} with respect to temperature. Hence, they express the temperature dependency of the binary interaction parameters $\beta_{MX}^{(i)}$, $i = 0, 1, 2, 3$ and C_{MX}^ϕ . To derive these parameters, the relative apparent molar enthalpy of the solute ${}^\phi L$ is necessary if there are no osmotic or activity coefficients at other temperatures available. Nonetheless, in terms of better consistency all available data should be used. Values for ${}^\phi L$ can be derived from molar heat of dilution $\Delta_{dil}H$ data with

$$\Delta_{dil}H(m_1 \rightarrow m_2) = {}^\phi L_2 - {}^\phi L_1 \quad (42)$$

where the relative apparent molar enthalpy of the solute before and after the dilution are given by ${}^\phi L_1$ and ${}^\phi L_2$ respectively. An additional way for the determination of ${}^\phi L_2$ is its calculation from heat of dissolution data with

$$\Delta_{sol}H = {}^\phi L_2 + \Delta_{sol}H^\circ \quad (43)$$

with $\Delta_{sol}H$ and $\Delta_{sol}H^\circ$ being the enthalpy of solution per mole of salt and the enthalpy of solution per mole of salt at infinite dilution.

Heat capacities are defined as the derivative of the enthalpy with respect to the temperature and the relationship to the relative enthalpy is expressed by

$$C_p = \left(\frac{\partial H}{\partial T} \right)_{p,m} = C_p^\circ + \left(\frac{\partial L}{\partial T} \right)_{p,m} \quad (44)$$

where C_p° is the heat capacity of pure water. The equation can be rewritten using Eqs. (17) and (18) yielding

$${}^\phi C_p - \bar{C}_{p_2}^\circ = \left(\frac{\partial {}^\phi L}{\partial T} \right)_{p,m} \quad (45)$$

where $\bar{C}_{p_2}^\circ$ is the partial molar heat capacity at infinite dilution. The derivation of Eq. (37) with respect to the temperature yields the equation for the calculation of the apparent molar heat capacity ${}^\phi C_p$

$${}^\phi C_p = \bar{C}_{p_2}^\circ + \nu |z_M z_X| \frac{A_J}{2b} \ln(1 + bI^{1/2}) - 2\nu_M \nu_X RT^2 [mB_{MX}^J + m^2 (\nu_M z_X) C_{MX}^J] \quad (46)$$

where the quantities A_J , B_{MX}^J and C_{MX}^J are given by

$$A_J = \left(\frac{\partial A_L}{\partial T} \right)_p \quad (47)$$

$$B_{\text{MX}}^J = \left(\frac{\partial^2 B_{\text{MX}}}{\partial T^2} \right)_{p,l} + \frac{2}{T} \left(\frac{\partial B_{\text{MX}}}{\partial T} \right)_{p,l} \quad (48)$$

and

$$C_{\text{MX}}^J = \left(\frac{\partial^2 C_{\text{MX}}}{\partial T^2} \right)_p + \frac{2}{T} \left(\frac{\partial C_{\text{MX}}}{\partial T} \right)_p \quad (49)$$

For the determination of the binary interaction parameters, all suitable thermodynamic data are included in one simultaneous least squares fit. To describe the temperature dependency, this work uses the following expression

$$P(T) = q_1 + q_2 (1/T - 1/T_R) T_0 + q_3 \ln(T/T_R) + q_4 (T - T_R)/T_0 + q_5 (T^2 - T_R^2)/T_0 \quad (50)$$

with $T_R = 298.15$ K and $T_0 = 1$ K. Eq. (50) shows all available parameters for the description of the ion interactions but on most occasions, not all are required for an accurate reproduction of the experimental data.

2.4 The Influence of Pressure on Crystal Growth

Up to this point, the focus of the presented equations is on concentration and temperature dependency. An additional aspect for the phase change behavior is the influence of pressure on the crystals. Here, both the crystallization and hydration pressure will be introduced. In order to do so, it is essential to clearly define the kind that is applied on the crystal and that in both cases, the monitored crystal is under anisotropic stress.

In the case of crystallization pressure, the crystal has to be confined, e.g. in a porous material, and it needs to be surrounded by a supersaturated solution with respect to the unloaded surfaces of the crystal (cf. Fig. 9). Note, that this chapter only treats crystals that are larger than about 100 nm. In this case, the effect of interfacial energies between the crystal–liquid interfaces can be neglected, hence, the crystal has to be in a macroporous material. The unloaded sides of the crystal are under the hydrostatic pressure p_1 of the solution while the loaded sides, that are growing against a pore wall, are under a pressure $p_c > p_1$. The crystal, therefore, is under anisotropic stress $\sigma = -\Delta p$ with $\Delta p = p_c - p_1$. The solution remains under ambient pressure, hence its pressure dependency can be omitted. For the growth of a crystal against the confining wall, a thin layer of solution expected to be only a few nanometers in thickness^[30,31], must be present between the loaded crystal side and the pore wall to act as a diffusion path.

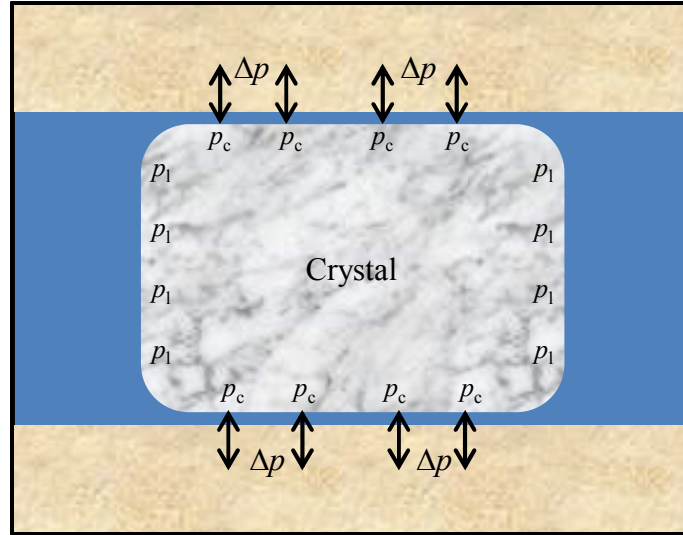


Figure 9: Crystal in a confined Space between two pore walls. Note, that all sides, loaded and unloaded, are in contact with the surrounding solution that is supersaturated with respect to the crystals unloaded sides.

Note, that the approach to describe the potential of crystals to grow against pressure is based on the differences of the chemical potentials of the loaded and unloaded sides of the crystal faces with the basic equations already mentioned in chapter 2.2. A comprehensive derivation of the following equation is given by Steiger.^[31] The resulting equation for the crystallization pressure is

$$\Delta p_{\text{cryst}} = \frac{RT}{V_m} \ln(a/a_0) \quad (51)$$

where Δp is the crystallization pressure, V_m is the molar volume of the solid phase and a and a_0 are the activity of the dissolved species in the supersaturated solution and its activity in the saturated solution, respectively. For a dissociation reaction shown in Eq. (3), the activity of the solid is given by the ion activity product

$$a = a_M^{v_M} a_X^{v_X} a_w^n \quad (52)$$

where a_M , a_X and a_w are the activities of the cation M, the anion X and the water activity respectively. The ion activity product of the saturated solution, a_0 , corresponds to the thermodynamic solubility product. The crystallization pressure is therefore proportional to the logarithmic degree of supersaturation $\ln S = a / a_0$, with a generation of pressure if $S > 1$.

The general hydration–dehydration reaction is given by Eq. (2). The equilibrium constant for a hydration reaction can be expressed by

$$K = p_{w,0} / p_{w,\text{eq}} = 1 / \varphi_{\text{eq}} \quad (53)$$

$p_{w,\text{eq}}$ and $p_{w,0}$ are the equilibrium water vapor partial pressure and the saturation water vapor pressure. φ_{eq} is the relative humidity at equilibrium between the two solid phases containing n_A and n_B molecules of water. If the lower hydrate with n_B moles water is inside a confined space, a hydration reaction can cause the generation of pressure. An expression for the maxi-

mum hydration pressure a hydrated crystal can grow against, Δp_{hydr} , was given by Mortensen^[32] with

$$\Delta p_{\text{hydr}} = \frac{\Delta n RT}{\Delta V_{\text{m}}} \ln(\varphi/\varphi_{\text{eq}}) \quad (54)$$

where $\Delta n = n_{\text{A}} - n_{\text{B}}$ and ΔV_{m} is the molar volume difference of the two solids. φ is the relative humidity at which the hydration reaction proceeds and φ_{eq} is the equilibrium RH at ambient pressure. At a given relative humidity, $\varphi > \varphi_{\text{eq}}$, the hydration pressure is the pressure that must be applied on a hydrating crystal to stop the hydration reaction. This means, that the driving force for the generation of hydration pressure is similar to the driving force of crystallization pressure, which is supersaturation. The difference here is the surrounding gaseous phase, instead of a liquid one, and the water vapor partial pressure is supersaturated with respect to the equilibrium water vapor partial pressure of the equilibrium reaction. In other words, the hydration pressure depends on the ratio of the ambient relative humidity to the equilibrium relative humidity. Note, that if the relative humidity rises above the deliquescence humidity of phase A, the salt absorbs water vapor to form a solution. Hence, above the deliquescence humidity of phase A, phase A cannot exist as a solid anymore and the generation of hydration pressure is no longer possible. In the case of phase B (anhydrous or lower hydrated) being present, an increasing relative humidity above its deliquescence humidity leads to the formation of a solution that is supersaturated with respect to phase A. This leads to a two-step mechanism of dissolution of phase B and the precipitation of phase A. Here the hydrated crystals of phase A generate a crystallization pressure that is limited by the supersaturation controlled by the ratio of dissolution and precipitation.

2.5 Measurement of Activity Data

As mentioned above, the characterization of the properties of electrolyte solutions with the ion interaction approach requires experimental data that can describe the Gibbs energy as a function of temperature and pressure. Common ways are the measurement of such quantities as a function of composition at isothermal and isobaric conditions. These can be supplemented with, e.g. heat of dilutions or heat capacities, from calorimetric measurements to establish a thermodynamically consistent relationship as shown in chapter 2.3.

Two ways exist to measure the activities in electrolyte solutions. On one side, there is the activity of the solute that can be measured in a precise way by measuring the electromotive force (e.m.f.) of a corresponding electrochemical cell. An alternative to the measurement of activity coefficients of the solute is the measurement of the activity of the solvent. For this task, a variety of different techniques are available.

The direct measurement of the vapor pressure of an electrolyte solution can be done in two different ways, static and dynamic. Both ways are capable to generate high quality values but they require very diligent preparations such as the removal of dissolved air from both the liquid and the gaseous phase (static) or a controlled gas flow that generates a saturated gas with respect to the solvent (dynamic). In addition, the measurement of solutions with solute

concentrations of less than 1 mol kg^{-1} yield less accurate values as changes in the vapor pressure of the solution become smaller with decreasing molality.^[33]

Both freezing point depressions and boiling point elevations deliver activities of the solvent as a function of composition but at different temperatures. In the present work this circumstance is not relevant, but the values could be corrected to isothermal conditions with enthalpy and heat capacity data.

A very common method that has been successfully established for the determination of solvent activities in aqueous electrolyte solutions is the isopiestic method. It is a relative method, where two or more solutions are equilibrating through a common vapor phase. For the equilibration process to take place, it is crucial to maintain isothermal conditions. The initial compositions of all solutions are known and when the solutions are in equilibrium with one another, they have the same vapor pressure. For it is a relative method, one or more solutions are reference solutions. The activities of such reference solutions must be known very precisely as a function of temperature and composition and a number of isopiestic reference standard solutions have been established. These reference standards are solutions of NaCl, KCl, H₂SO₄ and CaCl₂. After the equilibrium process and the determination of the solutions molalities, the water activity of the reference solutions can be calculated and, therefore, the water activities of all other solutions are known. A series of such measurements as a function of molality can deliver the solvents activity over a wide range. A more detailed overview about the isopiestic measurement technique is given by Rard and Platford.^[20]

3 Thermodynamic properties of $\text{ZnSO}_4(\text{aq})$ and phase equilibria in the $\text{ZnSO}_4\text{--H}_2\text{O}$ system from 268 K to 373 K¹

3.1 Introduction

Zinc sulfate is the zinc compound that is most frequently used and there is a variety of applications. For example, zinc sulfate is used in the viscose production process, in galvanizing baths, as an additive in fertilizers and animal feeds, as wood preservative and in medicine as an emetic, astringent or disinfectant.^[34] The production of metallic zinc via the hydrometallurgical process is based on acidic zinc sulfate solutions.^[35] The optimization of these processes requires precise knowledge of the binary phase diagram $\text{ZnSO}_4\text{--H}_2\text{O}$ as well as the ternary systems with sulfuric acid and impurities, such as calcium and magnesium.^[36]

Zinc sulfate forms a number of hydrates in the series $\text{ZnSO}_4 \cdot n\text{H}_2\text{O}$ several of which are known minerals, i.e. $\text{ZnSO}_4 \cdot 7\text{H}_2\text{O}$ (goslarite), $\text{ZnSO}_4 \cdot 6\text{H}_2\text{O}$ (bianchite), $\text{ZnSO}_4 \cdot 4\text{H}_2\text{O}$ (boyleite) and $\text{ZnSO}_4 \cdot \text{H}_2\text{O}$ (gunningite). Usually, these minerals occur as alteration products of sphalerite (ZnS) oxidation and are frequently observed as post-mining efflorescences on rocks.^[37] Knowledge of dehydration equilibria of these salts is important to understand their formation under natural conditions. $\text{ZnSO}_4 \cdot 7\text{H}_2\text{O}$ was also considered as a potential material for heat storage purposes either as a phase change material (PCM)^[38] or, more recently, as a thermochemical storage material^[12] utilizing cycles of dehydration and rehydration.

There is a rich literature with experimental solubilities and equilibrium data for the various hydration–dehydration equilibria that were used by different authors to construct the binary phase diagram of the system $\text{ZnSO}_4\text{--H}_2\text{O}$.^[39–41] However, the experimental data are significantly scattered and there is no agreement among different authors regarding the invariant points of the binary system. Moreover, compilations of critically evaluated thermodynamic data^[42,43] are not consistent with each other and with existing experimental data reported for the equilibrium $\text{ZnSO}_4 \cdot 7\text{H}_2\text{O} + \text{ZnSO}_4 \cdot 6\text{H}_2\text{O} + \text{vapor}$.^[41] Recently, using the experimental data of Chou and Seal^[41], Grevel and Majzlan derived adjusted values of the standard entropies and enthalpies of formation of goslarite and bianchite at 298.15 K.^[44]

Experimental data of the water activities of the saturated solutions, i.e. the deliquescence humidities (DRH) of the hydrates, are even more scattered and it is nearly impossible to constrain the phase boundaries $\text{ZnSO}_4 \cdot n\text{H}_2\text{O} + \text{saturated solution}$ in a $\phi\text{--}T$ phase diagram of the binary system. Since there is a reasonable solubility database, it appears to be more promising to calculate the water activities of the saturated solutions using an electrolyte solution model such as the Pitzer ion interaction model.^[23] Such models require thermodynamic data of electrolyte solutions at different temperatures. In the case of $\text{ZnSO}_4(\text{aq})$, while there is a reasonable database at 298.15 K^[45], there is a lack of data at other temperatures. Where thermal data (heat capacities, heats of dilution) and activity data are available at a reference temperature (usually 298.15 K), activity data can be calculated at other temperatures, not too far away from the reference temperature. This approach was used by Königsberger and Erickson^[46] to estimate Pitzer model parameters for $\text{ZnSO}_4(\text{aq})$ at high

temperatures from available parameters at 298.15 K. The same approach was also used recently by Wang et al.^[47]

The major objectives of the present work were to determine the model parameters of an extended Pitzer ion interaction model for $\text{ZnSO}_4(\text{aq})$ and to construct an updated phase diagram of the binary system $\text{ZnSO}_4\text{-H}_2\text{O}$. For that purpose, we have tested the suitability of an automated gravimetric water vapor sorption analyzer for the collection of new isopiestic data. In addition, existing thermodynamic data of $\text{ZnSO}_4(\text{aq})$ were carefully reviewed and used together with the new data to determine the model parameters of an extended Pitzer ion interaction model valid from the temperature of freezing to 373 K. This model was used together with available solubility and hydration–dehydration equilibrium data to determine the phase boundaries in the binary system including the stable phases gunningite, bianchite, goslarite and the metastable monoclinic zinc sulfate heptahydrate. The obtained phase diagram will then be used to overview fields of reaction parameters for a thermochemical heat storage unit operated with $\text{ZnSO}_4 \cdot n\text{H}_2\text{O}$ as storage material. Its theoretical energy density for the hydration from monohydrate to heptahydrate with 2.36 GJ m^{-3} is similar with MgSO_4 (2.3 GJ m^{-3}), a salt that has a very high storage density.

3.2 Experimental

Osmotic coefficients of $\text{ZnSO}_4(\text{aq})$ were determined with a water vapor sorption analyzer SPSx-1 μ (ProUmid, Germany) using $\text{NaCl}(\text{aq})$ as the isopiestic reference. In the vapor sorption analyzer, solutions are placed in dishes positioned in a plate like sample holder for up to 23 samples. The sample tray is placed inside a temperature controlled chamber connected to a humidity generator providing the desired constant water vapor pressure during equilibration of the samples. The atmosphere circulates within the chamber providing uniform temperature and vapor pressure. Each sample can be automatically positioned on the load cell of a micro-balance by turning and lowering the sample tray. All samples are weighed at predefined time intervals (10 minutes in this study) with a reading precision of 10^{-6} g. The analyzer can be operated at temperatures from 278.15 K to 313.15 K and relative pressures 0–0.95. With increasing temperature difference between the inside air and the ambient air the maximum relative pressure declines due to condensation at cold spots.

Zinc sulfate solutions were prepared from $\text{ZnSO}_4 \cdot 7\text{H}_2\text{O}$ (Emsure, Merck, Germany) dehydrated at 723.15 K for 72 h in a furnace. After the thermal treatment, the anhydrous ZnSO_4 was dissolved without further purification in doubly distilled water. The NaCl (Rectapur, VWR, Germany) used for the preparation of the reference solutions was treated in the same way. The major difference to the usual isopiestic technique is that in this setup the water activities of all solutions are determined by the relative humidity in the sorption analyzer as controlled by the humidity generator. Depending on their initial water activities, the solutions equilibrate with the surrounding atmosphere by release or uptake of water vapor resulting in a change in solution molalities. Equilibrations at constant temperature and pressure were continued until the rate of weight change was $< 0.05\%$ during a period of 2 h for all solutions. In this case, isopiestic equilibrium was assumed and the next series of measurements at a

different predefined relative pressure was initiated automatically. Total equilibration times were typically in the order of 35–50 h. Values of the osmotic coefficients ϕ^* of the NaCl(aq) reference solutions were calculated with the equation of Archer^[48] and those of $\text{ZnSO}_4\text{(aq)}$ were calculated using the equation for isopiestic equilibrium

$$\phi = \nu^* m^* \phi^* / \nu m = m^* \phi^* / m \quad (55)$$

where m^* is the equilibrium molality of NaCl(aq) , m is the equilibrium molality of ZnSO_4 and ν^* and ν are the total number of ions formed upon complete dissociation. In this study, $\nu^* = \nu = 2$.

Three solutions of both electrolytes were simultaneously exposed at constant temperature and vapor pressure. Measurements were first carried out at 298.15 K and the osmotic coefficients determined in this series were compared to the values recommended by Albright et al.^[45] Once the results were in satisfactory agreement, the temperature was changed to 288.15 K, 308.15 K and 313.15 K. Due to the problems with condensation mentioned before, measurements were only possible in a very narrow range of ZnSO_4 molalities with water activities from about 0.82–0.90 which is very close to the saturation water activities of $\text{ZnSO}_4\text{(aq)}$ in this temperature range. Therefore, many of the values obtained represent supersaturated solutions.

3.3 Theory and Equations

3.3.1 Phase Equilibria

The thermodynamic solubility product of a hydrate of composition $\text{ZnSO}_4 \cdot n\text{H}_2\text{O}$ is given by

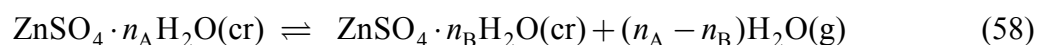
$$\ln K_n = \ln m(\text{Zn}^{2+}) + \ln m(\text{SO}_4^{2-}) + \ln \gamma(\text{Zn}^{2+}) + \ln \gamma(\text{SO}_4^{2-}) + n \ln a_w \quad (56)$$

where m and γ are the saturation molalities and the activity coefficients of the zinc and sulfate ions and a_w is the water activity of the saturated solution. Neglecting the minor influence of the non-ideal behavior of water vapor, at equilibrium, the water activity of a solution is given by Eq. (10). The water activity is related to the osmotic coefficient ϕ . For a binary ZnSO_4 solution of molality m , in analogy to Eq. (11), this yields:

$$\ln a_w = -2m\phi/m_w \quad (57)$$

Here, $m_w = 55.50844 \text{ mol} \cdot \text{kg}^{-1}$ is the molality of water.

Decomposition equilibria between different ZnSO_4 hydrates are given by



where subscripts A and B refer to two different hydrates containing n_A and n_B mol of water, respectively. The equilibrium constant of the decomposition reaction is given by

$$K_{AB} = p_{w,AB} / p_w^\circ = \phi_{AB} \quad (59)$$

where $p_{w,AB}$ and φ_{AB} refer to the equilibrium water vapor partial pressure and the equilibrium relative humidity for the hydration–dehydration equilibrium, i.e. the decomposition humidity of a hydrate. Therefore, values of K_{AB} can be obtained directly from experimental determinations of φ_{AB} . The equilibrium humidity, i.e. the equilibrium constant K_{AB} , is also related to the thermodynamic solubility products of the respective hydrates by

$$\ln K_B = \ln K_A - (n_A - n_B) \ln K_{AB} \quad (60)$$

3.3.2 Ion Interaction Model

In order to represent the available thermodynamic data for aqueous zinc sulfate the ion interaction approach of Pitzer was used.^[23] The Pitzer equations incorporate an extended Debye–Hückel limiting law and a virial expansion representing short range ionic interactions. In its original form, only second and third virial coefficients are considered and the ionic strength dependence of the third virial coefficient is neglected. More recently, numerous variants of Pitzer’s model have been used including extended models with ionic strength dependent third virial coefficients^[48] and higher order terms.^[23] In the present work, we neglect the ionic strength dependence of the third virial coefficient and we omit higher-order terms. However, we use an extension of the original equations to increase the numerical flexibility by including an additional parameter $\beta_{MX}^{(3)}$ to represent the ionic strength dependence of the second virial coefficient B_{MX} . Thus, we use the following expression to represent the ionic strength dependence of B_{MX}^ϕ :

$$B_{MX}^\phi = \beta_{MX}^{(0)} + \beta_{MX}^{(1)} \exp(-\alpha_{MX}^{(1)} I^{1/2}) + \beta_{MX}^{(2)} \exp(-\alpha_{MX}^{(2)} I^{1/2}) + \beta_{MX}^{(3)} \exp(-\alpha_{MX}^{(3)} I^{1/2}) \quad (61)$$

In Eq. (61) I is the ionic strength and $\beta_{MX}^{(0)}$, $\beta_{MX}^{(1)}$, $\beta_{MX}^{(2)}$ and $\beta_{MX}^{(3)}$ are the solute-specific interaction parameters. The parameter $\beta_{MX}^{(3)}$ is not used in the standard version of the Pitzer equations and fixed values are used for the coefficients α only depending on the electrolyte charge type. Moreover, the parameter $\beta_{MX}^{(2)}$ is only used for 2–2 charge type electrolytes to avoid the explicit treatment of association equilibria. In this case, α_2 is assigned a value of $12 \text{ kg}^{1/2} \text{ mol}^{-1/2}$ and $\beta_{MX}^{(2)}$ is related to the association equilibrium constant.^[28] In the extended set of equations used in our previous work^[33,49,50] individual values of $\alpha_{MX}^{(i)}$ were assigned to each electrolyte and the parameter $\beta_{MX}^{(2)}$ was also used for the treatment of other charge types, i.e. 1–1, 2–1 and 1–2 electrolytes. The present work includes both approaches, i.e. the use of the parameter $\beta_{MX}^{(2)}$ to represent ion association in $\text{ZnSO}_4(\text{aq})$ at low ionic strength and an additional parameter $\beta_{MX}^{(3)}$ to improve the model behavior at high ionic strength.

For the virial coefficients are being treated as empirical quantities, they have to be evaluated from experimental data. The temperature dependence of the parameters is expressed by Eq. (50). To represent the temperature dependence of the partial molar heat capacities of the solute at infinite dilution, ${}^\phi C_p^\circ$, Eq. (61) was also used. However, the value of the parameter q_1 , i.e. the value of ${}^\phi C_p^\circ$ at 298.15 K, was fixed at ${}^\phi C_{p,298.15 \text{ K}}^\circ = -301.69 \text{ J K}^{-1} \text{ mol}^{-1}$ which is the sum of the ionic standard partial molar heat capacities recommended by Criss and Millero.^[51]

3.4 Results and Discussion

3.4.1 Experimental Results

The results of the isopiestic measurements are listed in Table 2. The osmotic coefficients at 298.15 K agree with the values recommended by Albright et al.^[45] to within our reported uncertainties which are standard deviations of three replicate samples. Nonetheless, they were not included in the further data treatment due to their significantly larger uncertainty compared to the data of Albright et al.^[45] At 288.15 K, 308.15 K and 313.15 K the values show the right temperature dependent behavior and are consistent with the thermodynamic database for aqueous zinc sulfate solutions listed in Table 3. Measurements at other temperatures and lower molalities were not possible as mentioned before. Attempts to obtain data at higher molalities were unsuccessful due to crystallization from the supersaturated solutions and the formation of a thin crystalline layer covering the solution. These measurements were discarded.

Table 2
Isopiestic molalities and osmotic coefficients of $\text{ZnSO}_4(\text{aq})$.

T/K	$m(\text{NaCl})/$ $\text{mol}\cdot\text{kg}^{-1}$	$m(\text{ZnSO}_4)/$ $\text{mol}\cdot\text{kg}^{-1}$	$a_w^{(a)}$	$\phi(\text{ZnSO}_4)$
298.15	2.893 ± 0.012	3.223 ± 0.009	0.8971	$0.935 \pm 0.006^{(b)}$
298.15	3.974 ± 0.014	3.836 ± 0.011	0.8524	$1.156 \pm 0.008^{(b)}$
288.15	3.612 ± 0.039	3.567 ± 0.022	0.8690	1.093 ± 0.021
288.15	4.051 ± 0.039	3.787 ± 0.023	0.8503	1.189 ± 0.022
288.15	4.513 ± 0.036	$3.997^{(c)}$	0.8300	$1.294 \pm 0.022^{(c)}$
308.15	3.401 ± 0.012	3.614 ± 0.006	0.8757	1.019 ± 0.003
308.15	4.025 ± 0.006	3.962 ± 0.009	0.8493	1.144 ± 0.004
308.15	4.668 ± 0.012	4.295 ± 0.013	0.8211	1.274 ± 0.007
313.15	4.894 ± 0.009	4.470 ± 0.009	0.8108	1.302 ± 0.003
313.15	4.465 ± 0.011	4.250 ± 0.004	0.8299	1.217 ± 0.003
313.15	4.030 ± 0.011	4.014 ± 0.005	0.8489	1.133 ± 0.003

^(a) Calculated with the equation of Archer.^[48]

^(b) Data not included in further treatment.

^(c) Crystallization occurred in two solutions. The standard deviation is assumed to be close to the other solutions at 288.15 K.

3.4.2 Pitzer Model Parameters for $\text{ZnSO}_4(\text{aq})$

Albright et al.^[45] reported careful isopiestic measurements for $\text{ZnSO}_4(\text{aq})$ and critically evaluated isopiestic and e.m.f. data available in the literature. They provided recommended values of osmotic coefficients and mean activity coefficients at 298.15 K. Using an extended Pitzer type equation with an ionic strength dependent third virial coefficient and an additional fourth virial coefficient, they successfully represented the experimental data. In the present study, we have accepted their recommended values of osmotic coefficients and mean activity coefficients that were directly used as tabulated by them at round molalities. Additional data used

for the determination of the ion interaction parameters for $\text{ZnSO}_4(\text{aq})$ as described below are listed in Table 3.

Yang et al.^[52,53] made isopiestic measurements at 323.15 K and 373.15 K using $\text{CaCl}_2(\text{aq})$ and $\text{H}_2\text{SO}_4(\text{aq})$ as isopiestic reference electrolytes. They calculated osmotic coefficients of $\text{ZnSO}_4(\text{aq})$ using the equations of Anathaswamy and Atkinson for $\text{CaCl}_2(\text{aq})$ ^[54] and of Clegg et al. for $\text{H}_2\text{SO}_4(\text{aq})$.^[55] Deviations of their tabulated osmotic coefficients and those calculated using the equation of Holmes et al.^[56] do not exceed the expected experimental uncertainty. Therefore, their data were used as reported by them and were given full weight in the least squares treatment. Test calculations showed that the osmotic coefficients of the present study (cf. Tab. 2) are systematically high by about $\Delta\phi = 0.005$ to $\Delta\phi = 0.03$. The data at temperatures different from 298.15 K were included in the fit with reduced weight.

Osmotic coefficients from freezing temperatures^[57-61] were calculated using the equation of Klotz and Rosenberg^[62]. Freezing temperatures of Hausrath^[59] and of Brown and Prue^[61] for dilute solutions form a consistent database of osmotic coefficients. Though the available data at higher concentrations ($0.1\text{--}2.7\text{ mol kg}^{-1}$) show significant scatter, the data of Kahlenberg^[57], Rüdorff^[58] and de Coppet^[60] are consistent both with each other and with the remaining data. Most of their data were included in the fit with reduced weight. In contrast, osmotic coefficients calculated from the freezing point depressions of Jones and Getman^[63] were systematically low and had to be rejected.

Boiling temperatures were reported by Plake^[64] at low concentrations and by Kahlenberg^[57], Gerlach^[65] and Johnston^[66] at high molalities. Osmotic coefficients were calculated using the equation of Smith.^[67] Apart from the vapor pressure measurements of Tammann^[68] and the isopiestic measurements of Yang et al.^[53], these data are the only source of osmotic coefficients at high temperatures. Test calculations have shown that only the data of Plake^[64] and Kahlenberg^[57] are consistent with the remaining data, thus data from references^[65,66] were not used in the further data treatment.

Direct vapor pressure measurements for $\text{ZnSO}_4(\text{aq})$ solutions were reported by several authors.^[68-73] In most studies both the water vapor pressure p over aqueous ZnSO_4 solutions and the saturation vapor pressure p_0 , or, the relative lowering of the vapor pressure p/p_0 are recorded. In these cases, osmotic coefficients were calculated using Eqs. (26) and (27) of Rard and Platford^[20] for non-ideal vapor pressure correction. Molar volumes of water were calculated using an equation of Kell.^[74] Only in one study^[72], the saturation vapor pressures were not listed and were calculated using the equation of Wexler and Greenspan^[75] for the ITPS-48 temperature scale. In the relevant temperature range the IPTS-27 and ITPS-48 temperature scales are identical. Most of the old vapor pressure measurements show significant scatter and several datasets are inconsistent with the remaining data. Hence, the vapor pressures reported by Tamman^[68,69], Sidgwick and Eubank^[70], Emden^[72] and Dieterici^[73] were not used in the least squares treatment. Osmotic coefficients calculated from the vapor pressure measurements at 293.15 K and 298.15 K reported by Kangro and Groeneveld^[71] show a slight systematic deviation. The data at 293.15 K were included in the fit with reduced weight. As

mentioned before, the only data used at 298.15 K were the values recommended by Albright et al.^[45]

Thermochemical data are listed in Table 3. Lange et al.^[76] report heats of dilution for initial molalities from $1.0 \text{ mol}\cdot\text{kg}^{-1}$ to $0.003 \text{ mol}\cdot\text{kg}^{-1}$ at 298.15 K. Additional measurements at 298.15 K and higher molalities were carried out by Giauque et al.^[77] Data at lower temperature (273 K–295 K) and initial molalities $<0.25 \text{ mol kg}^{-1}$ were provided by Plake.^[78] All heat of dilution data are consistent with each other and were given full weight in the least squares treatment.

Isobaric heat capacities of $\text{ZnSO}_4(\text{aq})$ were reported by Giauque et al.^[77], Marignac^[79] and Cohen et al.^[80] covering temperature and molality ranges from 294 K to 308 K and 0.1– $3.5 \text{ mol}\cdot\text{kg}^{-1}$, respectively. Heat capacities were converted to apparent molar heat capacities using the heat capacities of pure water calculated from the equation of Wagner and Pruß.^[7] The data of Cohen et al.^[80] and Giauque et al.^[77] are in good agreement with each other and with the remaining data. The much older values of Marignac^[79] showed a systematic deviation and were not included in the final data treatment.

Table 3
 Literature sources for activities and thermal properties of $\text{ZnSO}_4(\text{aq})$.

Property ^(a)	T/K	$m/\text{mol kg}^{-1}$	$N^{(b)}$	$\sigma_{\text{est}}^{(c)}$	$\sigma_{\text{fit}}^{(c)}$	Reference
$\phi(\text{isop.})$	288.15–313.15	3.6–4.5	9 (11)	0.01	0.019	This work
$\phi(\text{isop.})$	298.15	0.01–4.3	34 (34)	0.002	0.002	[45] ^(d)
$\phi(\text{isop.})$	323.15	0.1–4.7	23 (24)	0.005	0.005	[52]
$\phi(\text{isop.})$	373.15	0.2–3.7	14 (15)	0.005	0.007	[53]
$\phi(\text{f.t.})$	271.23–272.89	0.1–1.0	6 (6)	0.05	0.057	[57]
$\phi(\text{f.t.})$	268.04–272.55	0.3–2.1	9 (9)	0.05	0.020	[58]
$\phi(\text{f.t.})$	273.11–273.15	0.0002–0.01	17(17)	0.05	0.016	[59]
$\phi(\text{f.t.})$	263.05–271.50	0.9–2.7	10 (10)	0.05	0.051	[60]
$\phi(\text{f.t.})$	272.93–273.14	0.005–0.1	25 (25)	0.01	0.011	[61]
$\phi(\text{f.t.})$	268.04–272.55	0.05–2.0	0 (10)	0.05	0.048	[63]
$\phi(\text{b.t.})$	373.23–374.21	0.2–2.8	15 (15)	0.05–0.1	0.058	[57]
$\phi(\text{b.t.})$	373.15–373.29	0.0008–0.3	9 (9)	0.05	0.018	[64]
$\phi(\text{b.t.})$	373.65–378.15	0.8–5.3	0 (10)	0.1	0.147	[65]
$\phi(\text{b.t.})$	373.22–373.45	0.1–1.0	0 (7)	0.1	0.194	[66]
$\phi(\text{v.p.})$	373.15	0.5–4.0	0 (5)	0.1	0.039	[68]
$\phi(\text{v.p.})$	314.32–373.37	1.9–3.3	0 (40)	0.1	0.048	[69]
$\phi(\text{v.p.})$	278.15	0.7–2.6	0 (3)	0.2	0.217	[70]
$\phi(\text{v.p.})$	293.15–298.15	0.9–3.9	6 (12)	0.01	0.016	[71]
$\phi(\text{v.p.})$	292.94–368.98	0.9–1.7	0 (46)	0.2	0.383	[72]
$\phi(\text{v.p.})$	273.15	0.5–2.6	0 (5)	0.1	0.115	[73]
$\ln\gamma_{\pm}^{(d)}$	298.15	0.01–4.3	34 (34)	0.002	0.002	[45]
${}^{\phi}L(\Delta_{\text{dil}}H)$	298.15	0.003–1.0	18 (18)	0.04–0.1	0.027	[76]
${}^{\phi}L(\Delta_{\text{dil}}H)$	298.15	1.4–3.5	5 (5)	0.070	0.076	[77]
${}^{\phi}L(\Delta_{\text{dil}}H)$	273.38–294.67	0.03–0.3	18 (18)	0.15	0.12	[78]
${}^{\phi}C_p$	297.58–308.15	0.8–3.5	27 (27)	0.012	0.005	[77]
${}^{\phi}C_p$	309.15	0.3–1.1	0 (3)	0.02	0.024	[79]
${}^{\phi}C_p$	294.15	0.1–3.2	6 (6)	15	0.007	[80]

^(a) Quantity and experimental technique (isop.: isopiestic; v.p.: vapor pressure; f.t.: freezing temperature; b.t.: boiling temperature).

^(b) Number of data used in fit (total number of measurements in brackets).

^(c) Standard errors σ_{est} and σ_{fit} for ${}^{\phi}L$ in $\text{kJ}\cdot\text{mol}^{-1}$ and for ${}^{\phi}C_p$ in $\text{kJ}\cdot\text{mol}^{-1}\cdot\text{K}^{-1}$.

^(d) Recommended smoothed values at round molalities after normalization (see Ref.^[45]).

The final database for aqueous zinc sulfate covers the temperature range from 265.9 K to 373.25 K with an upper molality limit of $4.7 \text{ mol}\cdot\text{kg}^{-1}$. In order to properly weight the different types of experimental data in the least squares treatment the estimated standard errors listed in column 5 of Table 3 were used. The error estimates are based on the reported experimental errors, the internal consistency and scatter of each dataset and the compatibility with the remaining datasets. All experimental data were included in one simultaneous least squares fit to the ion interaction equations for ϕ , $\ln\gamma$, ${}^{\phi}L$ and ${}^{\phi}C_p$ to determine the parameters of Eq. (50). Values of the Debye-Hückel parameters, A_{ϕ} , A_L and A_J , were taken from Archer and Wang^[26]

Initial calculations with the original equations for 2–2 electrolytes showed insufficient reproduction of the data if the usual value of $\alpha_2 = 12 \text{ kg}^{1/2} \cdot \text{mol}^{-1/2}$ was used. Though using smaller values for α_2 as in our previous work with other charge types improved the quality of the fit, the reproduction of the experimental osmotic coefficients at low molalities was not satisfactory. In addition, the calculated heat of dilutions showed unsatisfactory large deviations from the experimental data. Therefore, the extended form of the ion interaction equations including the $\beta^{(3)}$ terms was used in the further data treatment. Values of $\alpha_1 = 1.3 \text{ kg}^{1/2} \text{ mol}^{-1/2}$, $\alpha_2 = 17 \text{ kg}^{1/2} \text{ mol}^{-1/2}$ and $\alpha_3 = 0.5 \text{ kg}^{1/2} \text{ mol}^{-1/2}$ were fixed after trial calculations. The final model parameters are listed in Table 4.

A plot of the differences between osmotic coefficients from isopiestic data and calculated values of ϕ is shown in Figure 10. At 298.15 K, there is only a slight cyclic deviation of the calculated values from both the experimental data at 298.15 K and those calculated with the equation of Albright et al.^[45] which contains one parameter more than our equation. Nonetheless, the root mean square deviation between the two equations is only $\sigma_{\text{fit}} = 0.002$. There is also very good agreement with the isopiestic data of Yang et al. at 323.15 K^[52] and 373.15 K.^[53] In contrast, the osmotic coefficients based on the vapor pressure data of Kangro and Groeneveld^[71] are systematically high by about $\Delta\phi = 0.01$. As mentioned before, also our own isopiestic measurements are systematically high by $\Delta\phi = 0.005$ to $\Delta\phi = 0.03$. We assume that temperature gradients in the water vapor sorption analyzer and insufficient equilibration times are the major sources of error.

There is also very good agreement between the model calculated activity coefficients at 298.15 K and the values recommended by Albright et al.^[45] ($\sigma_{\text{fit}} = 0.002$ for $\ln\gamma_{\pm}$). Also all thermal data at low temperatures, i.e. the heats of dilutions at (273–298) K^[76–78] and the apparent molar heat capacities at (294–308) K^[77,80] are reproduced to within the estimated experimental uncertainty. Hence, the model is well defined at temperatures near 298 K. At high temperature, the model is constrained by the isopiestic data of Yang et al.^[52,53] and the boiling temperature data.^[57,64] At low temperature, there is a lack of reliable data as the heat of dilution measurements of Plake^[78] at (273–294) K only extend to about 0.25 mol kg^{-1} . Therefore, the model at low temperature is largely constrained by the freezing temperature data^[57,58,60,61] which are rather scattered at higher molalities, however.

Table 4
Parameters of Eq. (50) for the temperature dependence of the ion interaction parameters for $\text{ZnSO}_4(\text{aq})$.

	$\beta^{(0)}$	$\beta^{(1)}$	$\beta^{(2)}$	$\beta^{(3)}$	C^ϕ	${}^\phi C_p^\circ$
q_1	1.003626E-01	-1.204427E+02	2.386703E+00	2.093528E-010	4.754695E-02	3.0169E+02 ^(a)
q_2	-2.756292E+03	-5.229934E+05	-1.067103E+05	3.639162E+04	8.466135E+01	0
q_3	0	-1.910545E+03	-6.864893E+02	2.339189E+02	0	0
q_4	-7.636266E-02	0	1.116155E+00	-3.803884E-01	0	-6.735E+070
q_5	8.095423E-05	0	0	0	0	0

(a) value taken from Ref.^[51]

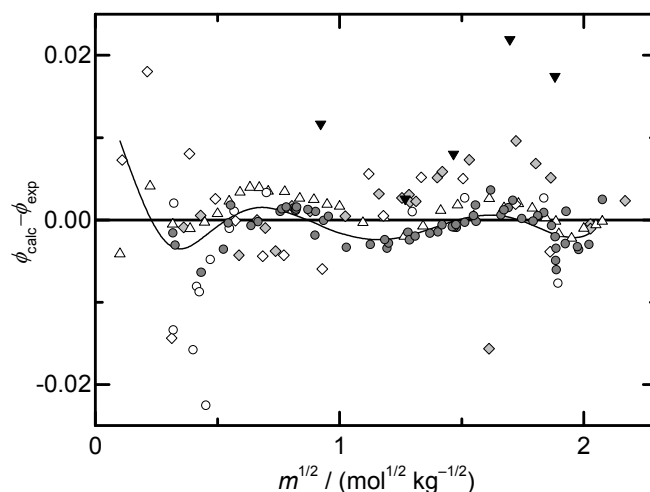


Figure 10: Deviations of the osmotic coefficients at 293.15 K^[71] (solid inverted triangles), 298.15 K^[45] (grey circles) and 323.15 K^[52] (grey diamonds) and 373.15 K^[53] (open diamonds) from the present model equation; $\Delta\phi = \phi_{\text{calc}} - \phi_{\text{exp}}$.^[45,52,71,81] The solid line represents the recommended values of Albright et al.^[45] and white circles show isopiestic data not used in their data treatment.

3.4.3 Solubility Products of $\text{ZnSO}_4 \cdot n\text{H}_2\text{O}$

According to Eqs. (56) and (60), both solubility data and equilibrium relative humidities are suitable for the calculation of the thermodynamic solubility products of the various hydrates. The available literature data of solubilities and equilibrium relative humidities for the decomposition reaction of the hydrates are listed in Tables 5 and 6 and were critically evaluated. Older data listed in the compilation of Timmermans^[82] are not consistent with the remaining data and were not considered further. In general, most of the available solubilities of the two heptahydrate phases and of the hexahydrate are in very good agreement. A selection of solubilities that form a consistent database for the determination of the thermodynamic solubility products is depicted in Figure 11. In contrast, agreement of solubilities of $\text{ZnSO}_4 \cdot \text{H}_2\text{O}$ reported by different authors is less satisfactory (cf. Fig. 11).

Using the ion interaction parameters of Table 4, activity coefficients and water activities of the saturated solutions of $\text{ZnSO}_4 \cdot n\text{H}_2\text{O}$ were calculated yielding, values of the thermodynamic solubility products of these solids according to Eq. (56).

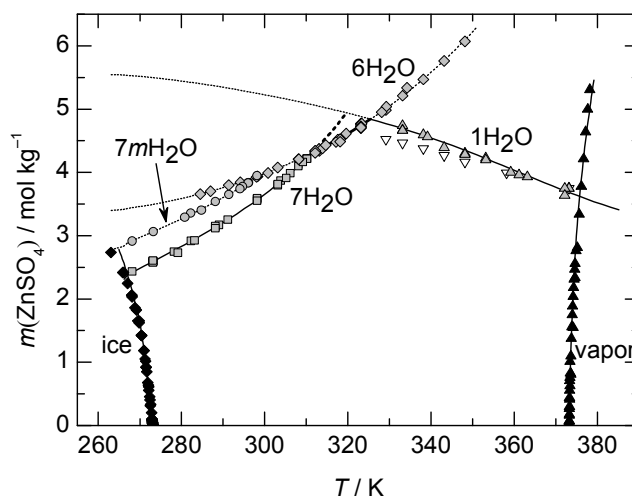


Figure 11: Solubilities in the system $\text{ZnSO}_4\text{-H}_2\text{O}$. Symbols represent experimental solubility data taken from the literature (see Table 5); grey squares: orthorhombic $\text{ZnSO}_4\cdot 7\text{H}_2\text{O}$; grey circles monoclinic $\text{ZnSO}_4\cdot 7\text{H}_2\text{O}$; grey diamonds: $\text{ZnSO}_4\cdot 6\text{H}_2\text{O}$; gray triangles: $\text{ZnSO}_4\cdot 1\text{H}_2\text{O}$ ^[83–85] inverted triangles: $\text{ZnSO}_4\cdot 1\text{H}_2\text{O}$ ^[86]; solid diamonds and triangles depict freezing^[57–61,63] and boiling^[57,64–66] temperatures respectively. Solid and dashed lines represent calculated stable and metastable solubilities.

Solubilities of the two heptahydrate phases from several studies are in excellent agreement with each other (cf. Fig. 11). The goslarite solubilities of Callendar and Barnes^[87], Cohen^[88], Cohen and Hetterschij^[89], Caven and Johnston^[90], Schröder^[85], Rohmer^[86] and Albright^[45] yielded the thermodynamic solubility products $\ln K_{70}$ of goslarite pictured in Figure 12a. A fit of Eq. (50) to these values yielded the parameters listed in Table 7 that represent the temperature dependence $\ln K_{70}$ from about 268 K to 310 K. The calculated solubilities using these parameters give a root mean square deviation of the saturation molalities of $0.013 \text{ mol}\cdot\text{kg}^{-1}$ (cf. Fig. 11).

Table 5
Solubility data base for the system $\text{ZnSO}_4\text{-H}_2\text{O}$.

Solid phase ^(a)	T/K	$N^{(b)}$	Reference
7 H_2O	298.15	1 (1)	[45]
1 H_2O	353.15–373.15	2 (2)	[83]
1 H_2O	333.15–373.15	8 (8)	[84]
7 H_2O	273.15–310.15	4 (4)	[85]
6 H_2O	317.15–323.15	3 (3)	
1 H_2O	333.15–372.15	4 (4)	
7 H_2O	303.15–309.15	3 (3)	[86]
6 H_2O	313.15–348.15	7 (7)	
1 H_2O	329.15–373.15	0 (7)	
7 H_2O	273.15–303.85	6 (6)	[87]
6 H_2O	313.07–323.35	9 (9)	
7 H_2O	268.15–308.15	6 (6)	[88]
$m\text{-}7\text{H}_2\text{O}$	268.15–298.15	5 (5)	
6 H_2O	303.15–312.15	4 (4)	
7 H_2O	273.15–310.15	9 (9)	[89]
6 H_2O	312.15–328.15	4 (4)	
7 H_2O	298.15	1 (1)	[90]
$m\text{-}7\text{H}_2\text{O}$	280.78–296.09	7 (7)	[91]
6 H_2O	284.50–334.25	11 (11)	
7 H_2O	273.15–303.15	0 (4)	[92]
7 H_2O	279.15	0 (1)	[93]
1 H_2O	451.15–530.15	2 (8)	[94]

(a) 7 H_2O : $\text{ZnSO}_4 \cdot 7\text{H}_2\text{O}$ (goslarite), $m\text{-}7\text{H}_2\text{O}$: monoclinic $\text{ZnSO}_4 \cdot 7\text{H}_2\text{O}$,
6 H_2O : $\text{ZnSO}_4 \cdot 6\text{H}_2\text{O}$ (bianchite), 1 H_2O : $\text{ZnSO}_4 \cdot \text{H}_2\text{O}$ (gunningite).

(b) Number of data used in least squares fit (total number of experimental data).

The determination of the solubility products of the monoclinic heptahydrate is based on the solubility data of Cohen^[88] and Bury^[91] that cover the range from 268.15 K to 298.15 K. Both datasets are in good agreement with each other. The solubility products $\ln K_{7m}$ calculated from their data are shown in Figure 12b and were used to determine the parameters of Eq. (50) that are listed in Table 7. The calculation of the solubilities with these values of $\ln K_{7m}$ gives a root mean square deviation of $0.011 \text{ mol} \cdot \text{kg}^{-1}$ (cf. Fig. 11).

Table 6
Sources of experimental data for the equilibrium humidities in the system $\text{ZnSO}_4\text{-H}_2\text{O}$.

Phase boundary	T/K	$N^{(a)}$	Reference
$7\text{H}_2\text{O-6H}_2\text{O}$	300.80–308.89	4 (4)	[41]
$7\text{H}_2\text{O-6H}_2\text{O}$	299.15–309.53	6 (6)	[93] ^(c)
$7\text{H}_2\text{O-1H}_2\text{O}$	269.95–295.07	0 (20)	
$6\text{H}_2\text{O-1H}_2\text{O}$	296.99–324.24	21 (21)	
$7\text{H}_2\text{O-6H}_2\text{O}$	284.75–307.65	0 (7)	[95]
$7\text{H}_2\text{O-6H}_2\text{O}$	291.15–303.10	5 (5)	[96]
$6\text{H}_2\text{O-1H}_2\text{O}$	291.00–304.85	6 (6)	
$7\text{H}_2\text{O-6H}_2\text{O}$	276.60–287.20	0 (5)	[97]
$7\text{H}_2\text{O-6H}_2\text{O}$	293.15	0 (1)	[98]
$7\text{H}_2\text{O-6H}_2\text{O}$	307.35	1 (1)	[99]
$7\text{H}_2\text{O-6H}_2\text{O}$	288.85–291.75	0 (6)	[100]
$6\text{H}_2\text{O-1H}_2\text{O}$	293.35	0 (1)	
$7\text{H}_2\text{O-6H}_2\text{O}$	298.15	0 (1)	[101]
$6\text{H}_2\text{O-1H}_2\text{O}$	298.15	1 (1)	
$6\text{H}_2\text{O-1H}_2\text{O}$	298.15	1 (1)	[102]
$7\text{H}_2\text{O-6H}_2\text{O}$	278.59	1 (1)	[103]
$7\text{H}_2\text{O-6H}_2\text{O}$	298.15	1 (1)	[104]
$7\text{H}_2\text{O-6H}_2\text{O}$	298.15	1 (1)	[105]
$6\text{H}_2\text{O-1H}_2\text{O}$	298.15	1 (1)	
$7\text{H}_2\text{O-6H}_2\text{O}$	283.15–298.15	4 (4)	[106]
$6\text{H}_2\text{O-1H}_2\text{O}^{(b)}$	283.15–298.15	0 (4)	
$7\text{H}_2\text{O-6H}_2\text{O}$	298.15–308.15	3 (3)	[107]
$7\text{H}_2\text{O-1H}_2\text{O}$	31.15–323.15	4 (4)	[108]
$7\text{H}_2\text{O-6H}_2\text{O}$	298.15	0 (2)	[109]
$6\text{H}_2\text{O-1H}_2\text{O}$	298.15	0 (2)	

(a) Number of data used in least squares fit (total number of experimental data).

(b) In the original paper^[106] this value was assigned to a $6\text{H}_2\text{O-5H}_2\text{O}$ phase boundary.

(c) Data retrieved from a vapor pressure diagram in Ref.^[93]

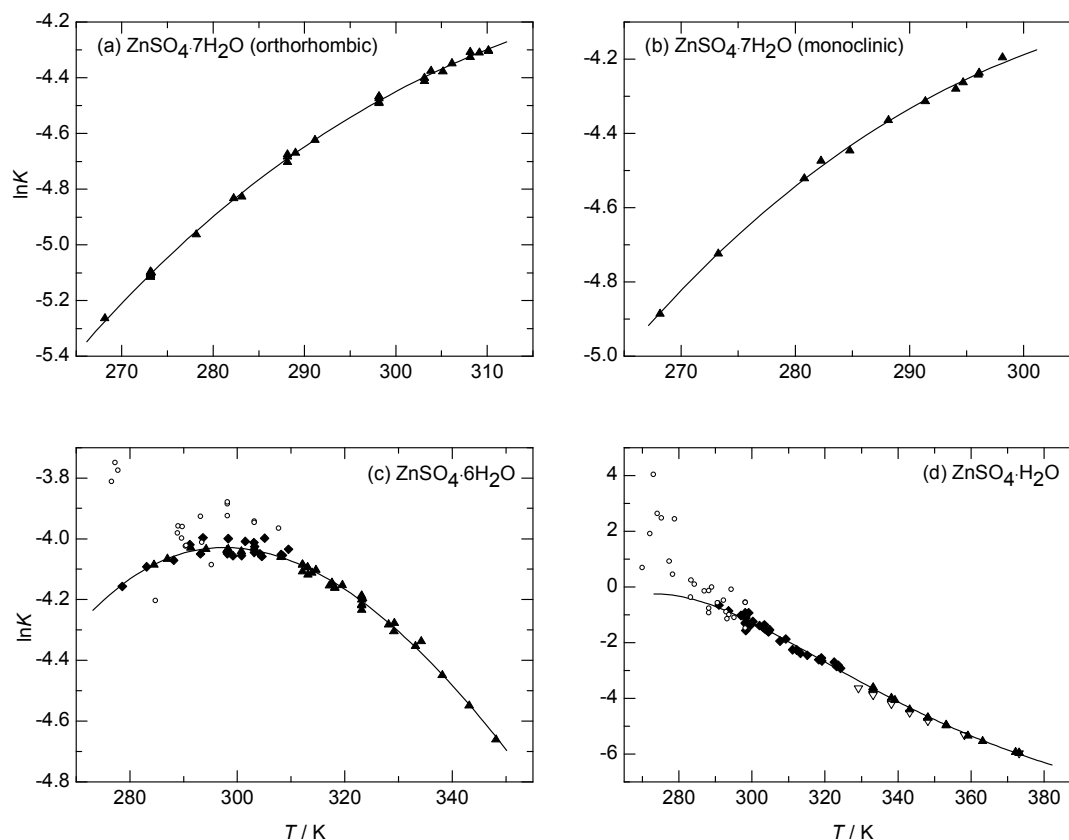


Figure 12: Thermodynamic solubility products, $\ln K$, of (a) $o\text{-ZnSO}_4\cdot 7\text{H}_2\text{O}$ (goslarite), (b) $m\text{-ZnSO}_4\cdot 7\text{H}_2\text{O}$, (c) $\text{ZnSO}_4\cdot 6\text{H}_2\text{O}$ (bianchite) and (d) $\text{ZnSO}_4\cdot \text{H}_2\text{O}$ (gunningite). Solid curves depict solubility products calculated with Eq. (50) and parameters listed in Table 7. Symbols represent experimental data (solid triangles: solubilities; solid diamonds: hydration–dehydration equilibrium humidities for the goslarite–bianchite, goslarite–gunningite and bianchite–gunningite equilibrium; white circles: data not used in least square treatment; inverted triangles: $\text{ZnSO}_4\cdot \text{H}_2\text{O}$ solubility data of Rohmer^[86] that were not used in the least squares fit).

The available solubility data of bianchite, $\text{ZnSO}_4\cdot 6\text{H}_2\text{O}$ ^[85–89,91], cover the temperature range from 285–348 K, thus, data also exist at temperatures where it is metastable with respect to the formation of goslarite (< 311 K), $m\text{-ZnSO}_4\cdot 7\text{H}_2\text{O}$ (< 298 K) and gunningite (> 325 K). As mentioned before, there is good agreement of the hexahydrate solubilities reported by different authors. The values of the solubility product $\ln K_6$ of bianchite calculated from the solubility data are shown as black triangles in Figure 12c. Additional values of $\ln K_6$ were calculated from the available data of the $7\text{H}_2\text{O}\text{-}6\text{H}_2\text{O}$ hydration–dehydration equilibrium using Eq. (60) together with the parameters of Eq. (50) for the solubility product of goslarite. These data are shown as black diamonds in Figure 12c. Though the experimental data for the decomposition equilibria are significantly more scattered, there is reasonable agreement of the calculated solubility products with those calculated from the solubility data. For the final least squares treatment, we accepted the data of Chou and Seal^[41], Copeland and Short^[93], Frowein^[96], Linebarger^[99], Schumb^[104], Ishikawa and Murooka^[105], Bonell and Burrige^[106] and Bell.^[107] Other decomposition humidities were inconsistent with the remaining data and were not used in the fit.^[95,97,98,100,101,109] The least squares fit yielded the coefficients listed in Table 7. Recalculation of the solubilities with these parameters together with the ion interaction equations yields nice agreement with a root mean square deviation of $0.025 \text{ mol}\cdot\text{kg}^{-1}$ (cf. Fig. 11).

The available data for the determination of the monohydrate solubility product partly disagree with each other, particularly in the temperature range between 329 K and 373 K (cf. Fig. 11). Rohmer^[86], on the one side, reported lower solubilities intersecting the solubility curve for the hexahydrate at 322 K. On the other side, Benrath^[83,84] and Schröder^[85] consistently report higher solubilities intersecting the hexahydrate curve at (327–328) K. The two monohydrate solubility curves approach each other with increasing temperature until they meet at temperatures around 373 K.

Additional data that can be used to constrain the thermodynamic solubility product of gunningite at low temperature come from the equilibrium humidities of the dissociation reactions. For the $7\text{H}_2\text{O}\text{-1H}_2\text{O}$ equilibrium, only two datasets exist, the vapor pressure measurements of Copeland and Short^[93] in the temperature range (268–324) K and those of Kohler and Zäske^[108] at (311–323) K. The values of Copeland and Short^[93] had to be discarded for they predict too low decomposition humidities. The values of Kohler and Zäske^[108] are consistent with the solubility data and were included in the fit. For the $6\text{H}_2\text{O}\text{-1H}_2\text{O}$ equilibrium, there exist internally consistent data^[93,96,101,102,105] that agree with each other to within the respective measurement uncertainties. Only the decomposition humidities of Müller-Erzbach^[100] and Uvaliev and Motornaya^[109] were not in line with the remaining data and were not considered further.

The thermodynamic solubility products of gunningite calculated from these data are also in line with those calculated from the data of Kohler and Zäske^[108] for the $7\text{H}_2\text{O}\text{-1H}_2\text{O}$ equilibrium and those obtained from the monohydrate solubilities of Benrath^[83,84] and Schröder^[85] but not with those reported by Rohmer^[86] which were, therefore, not included in the least squares treatment (cf. Fig. 12d). In addition, two solubilities at 476.15 K and 492.15 K were also included in the least squares fit although the calculation of the activity products of these values required significant extrapolation of our equation for $\text{ZnSO}_4(\text{aq})$. Nonetheless, including these data ensures a smooth extrapolation to higher temperatures where increasing deviations in the calculation of the activities are compensated by adjusted values of the thermodynamic solubility product. The parameters of Eq. (50), describing the temperature dependence of $\ln K_1$ are listed in Table 7. Recalculation of the accepted solubilities between 333 K and 373 K with these parameters yields nice agreement with a root mean square deviation of $0.045 \text{ mol}\cdot\text{kg}^{-1}$ (cf. Fig. 11).

Table 7

Parameters of Eq. (50) for the temperature dependence of the logarithmic thermodynamic solubility products.

	o- $\text{ZnSO}_4\cdot 7\text{H}_2\text{O}$	m- $\text{ZnSO}_4\cdot 7\text{H}_2\text{O}$	$\text{ZnSO}_4\cdot 6\text{H}_2\text{O}$	$\text{ZnSO}_4\cdot \text{H}_2\text{O}$
q_1	-4.480622E+00	-4.211082E+00	-4.028401E+00	-1.152275E+00
q_2	-8.355210E+03	-1.010144E+04	-9.396178E+03	-2.761181E+05
q_3	-2.288444E+01	-3.064689E+01	-2.559929E+01	-2.242679E+03
q_4	0	0	-2.110495E-02	5.801853E+00
q_5	0	0	0	-2.438235E-03

3.4.4 Phase Diagram $\text{ZnSO}_4\text{--H}_2\text{O}$

The complete phase diagram of the binary system $\text{ZnSO}_4\text{--H}_2\text{O}$ calculated using the present model is shown in Figure 13. It pictures the phase boundaries of the three stable phases goslarite, bianchite and gunningite as well as the metastable monoclinic heptahydrate. Only those experimental data for the dissociation equilibria are shown that were included in the final model parameterization. Copeland and Short^[93] also reported a phase diagram which was based essentially on their own vapor pressure measurements between 270 K and 324 K. As their values show significant scatter and since they did not include other data, the present evaluation is considered more reliable. D'Ans et al.^[39] reported phase boundaries based on vapor pressure data and solubilities in the binary system and the two ternary systems $\text{ZnSO}_4\text{--ZnCl}_2\text{--H}_2\text{O}$ and $\text{KCl--ZnSO}_4\text{--H}_2\text{O}$. However, their evaluation is obviously based on erroneous vapor pressure data, most likely those of reference^[106], resulting in significant deviations of their phase boundaries from the most reliable data (cf. Fig. 14a).

More recently, the $7\text{H}_2\text{O--}6\text{H}_2\text{O}$ phase boundary was investigated by Chou and Seal^[41] and, subsequently, by Grevel and Majzlan.^[44] The phase boundary proposed by Chou and Seal^[41] is based on their own measurements in the temperature range (300–308) K and extrapolation to both higher and lower temperature assuming a temperature independent enthalpy of reaction. Grevel and Majzlan^[44] also used the data of Chou and Seal^[41] but additionally included the standard enthalpies of formation and the standard entropies of goslarite and bianchite at 298.15 K as adjustable parameters. Also in their treatment, the enthalpy of reaction is assumed to be constant.

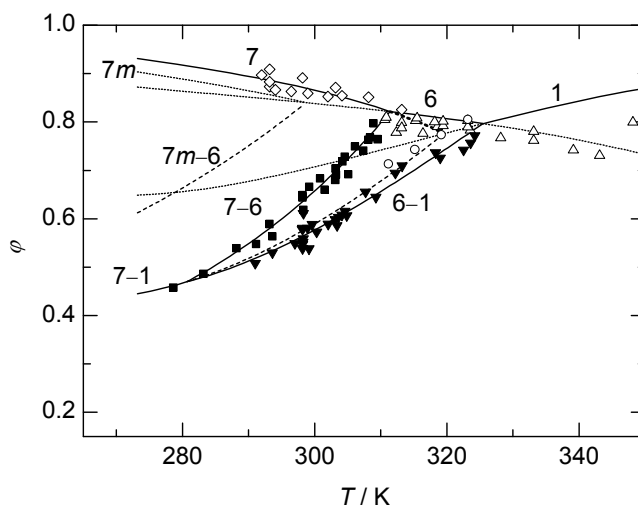


Figure 13: Experimental and calculated phase boundaries in the system $\text{ZnSO}_4\text{-H}_2\text{O}$ from 273.15 K to 373.15 K. Solid lines represent deliquescence humidities and hydration–dehydration equilibria of $\text{ZnSO}_4\cdot 7\text{H}_2\text{O}$ (denoted as 7), $\text{ZnSO}_4\cdot 6\text{H}_2\text{O}$ (6) and $\text{ZnSO}_4\cdot \text{H}_2\text{O}$ (1); dashed lines show metastable phase boundaries $\text{ZnSO}_4\cdot 7\text{H}_2\text{O}\text{-ZnSO}_4\cdot \text{H}_2\text{O}$ (7–1) and $m\text{-ZnSO}_4\cdot 7\text{H}_2\text{O}\text{-ZnSO}_4\cdot 6\text{H}_2\text{O}$ (7m–6); dotted lines represent metastable deliquescence humidities (1, 6, 7, 7m). Symbols represent experimental data and have the following meaning: deliquescence humidities of $\text{ZnSO}_4\cdot 7\text{H}_2\text{O}$ (diamonds), deliquescence humidities of $\text{ZnSO}_4\cdot 6\text{H}_2\text{O}$ (triangles), $\text{ZnSO}_4\cdot 7\text{H}_2\text{O}\text{-ZnSO}_4\cdot 6\text{H}_2\text{O}$ equilibrium humidities (squares), $\text{ZnSO}_4\cdot 7\text{H}_2\text{O}\text{-ZnSO}_4\cdot \text{H}_2\text{O}$ equilibrium humidities (circles), $\text{ZnSO}_4\cdot 6\text{H}_2\text{O}\text{-ZnSO}_4\cdot \text{H}_2\text{O}$ equilibrium humidities (inverted triangles). Only those experimental data for the dissociation equilibria are shown that were included in the final model parameterization.

As shown in Figure 14a, the $7\text{H}_2\text{O}\text{-}6\text{H}_2\text{O}$ phase boundary proposed by both Chou and Seal^[41] and Grevel and Majzlan^[44] is in good agreement with the present calculations. The maximum deviation of $\Delta\varphi = 0.019$ from the experimental values of Chou and Seal^[41] largely reflects the scatter of the experimental data at temperatures above about 290 K. At lower temperatures where the values of Chou and Seal are obtained by extrapolation it appears that our model provides a better representation of the experimental data. As they are based on the same experimental data, the values of Grevel and Majzlan^[44] show the same temperature dependence as those of Chou and Seal.^[41] There is a small systematic deviation between the two treatments as a result of the slightly different values of the standard Gibbs energy of reaction at 298.15 K of $\Delta_r G = 9.634 \text{ kJ mol}^{-1}$ ^[41] and $\Delta_r G = 9.570 \text{ kJ mol}^{-1}$ ^[44] used in both studies. Therefore, the deviation of our model from that of Grevel and Majzlan^[44] at high temperatures is slightly larger with a maximum deviation of $\Delta\varphi = 0.022$ at 308 K. As mentioned before, the $7\text{H}_2\text{O}\text{-}6\text{H}_2\text{O}$ phase boundary proposed by D’Ans and Freund^[40] reveals significant deviations from the most reliable experimental data.

Our predicted equilibrium humidities for the goslarite–gunningite and the bianchite–gunningite transition are in good agreement with those experimental data that were found to be consistent with the gunningite solubilities (cf. Fig. 14b and c). In contrast, the equation of D’Ans and Freund^[40] is obviously based on the data of Bonnell and Burrige^[106] (cf. Fig. 14c) that are not compatible with the solubility data (cf. Fig. 12d). Similarly, our calculated equilibrium humidities for the goslarite–gunningite transition are in reasonable agreement with the data of Kohler and Zäske^[108] which are consistent with the gunningite solubilities (cf. Fig. 14b). As mentioned before, the experimental data at low temperatures are badly scat-

tered and inconsistent with the solubility data. The equation reported by D'Ans and Freund^[40] is not in agreement with any of the experimental data.

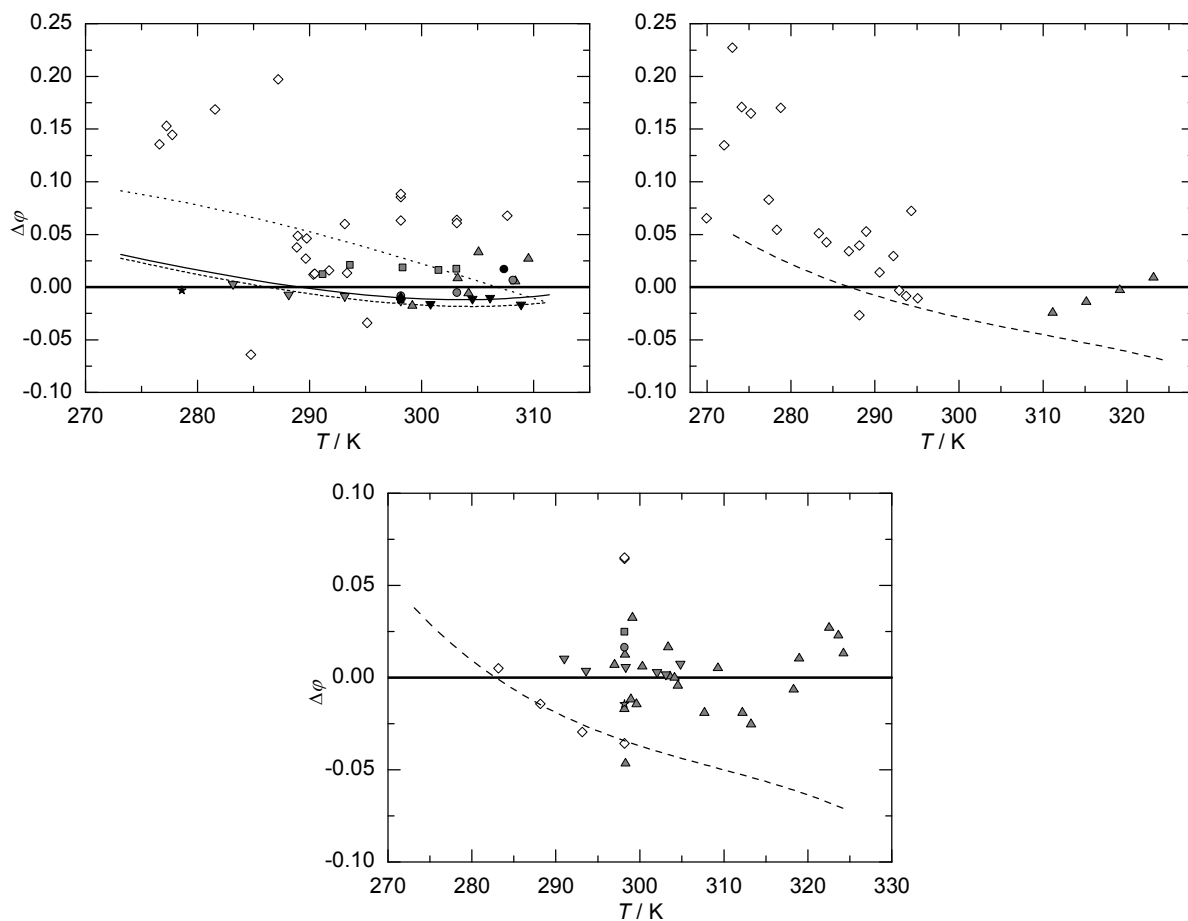


Figure 14: Differences ($\Delta\varphi = \varphi_{\text{calc.}} - \varphi_{\text{exp.}}$) between equilibrium humidities calculated with the present model and experimental data for the goslarite–bianchite ($7\text{H}_2\text{O}-6\text{H}_2\text{O}$) equilibrium (a), the goslarite–gunningite ($7\text{H}_2\text{O}-1\text{H}_2\text{O}$) equilibrium (b) and the bianchite–gunningite ($6\text{H}_2\text{O}-1\text{H}_2\text{O}$) equilibrium (c). Symbols represent experimental data: *open diamonds*: data not used in the least square treatment (cf. Tab. 6), *open circles*^[106] (rejected), *grey triangles*^[93], *grey diamonds*^[96], *grey squares*^[107], *grey inverted triangle*^[103], *grey stars*^[105], *grey circles*^[106], *black triangle*^[104], *black diamonds*^[41], *black square*^[9], *black inverted triangles*^[101], *black stars*^[108], *black circle*^[102]. Dashed, solid and dotted lines represent deviations of values calculated with equations of^[40,41,44], respectively.

A comparison of deliquescence humidities of goslarite and bianchite calculated using the present model with selected experimental data is shown in Figure 13. Experimental deliquescence humidities, i.e. vapor pressures over saturated solutions, typically show significantly higher scatter than experimental data of vapor pressures over undersaturated solutions. This is due to the fact that in such measurements both vapor–liquid and solid–liquid equilibria have to be established.^[50] The available deliquescence humidities of goslarite and bianchite also show significant scatter and were not included in the database for the determination of the ion interaction parameters of $\text{ZnSO}_4(\text{aq})$. The data of Kohler and Zäske^[108] and the deliquescence humidities of goslarite reported by Copeland and Short^[93] were found to be inconsistent with both the remaining data and with the present model equations. Data reported by Ishikawa and Murooka^[105], Diesnis^[110] and Kou and Schmidt^[111] agree to within the estimated experimental uncertainty with our calculated values (cf. Fig. 13). Similarly, the deliquescence humidities of

bianchite reported by Copeland and Short^[93] and by Wiedemann^[95] show reasonable agreement with the model calculations up to 343 K.

Invariant points of the system $\text{ZnSO}_4\text{-H}_2\text{O}$ obtained in this study are listed in Table 8. Our value for the equilibrium temperature of the assemblage $\text{ZnSO}_4\cdot 7\text{H}_2\text{O} + \text{ZnSO}_4\cdot 6\text{H}_2\text{O} + \text{solution} + \text{vapor}$ (311.8 K) is in good agreement with literature data^[41,86,87,89,93,112] reporting transition temperatures from 311.1 K to 311.3 K. Most of these values were determined by interpolation from either solubility or decomposition humidities. Direct experimental determinations were only attempted in two studies where transition temperatures of (311.25–311.35) K^[113] and 311.28 K^[112] were found which are in good agreement with the present value.

For the assemblage $\text{ZnSO}_4\cdot 7\text{H}_2\text{O} + \text{ZnSO}_4\cdot \text{H}_2\text{O} + \text{solution} + \text{vapor}$, the transition temperatures of D’Ans and co-workers ranging from 316 K^[40] to 328 K^[39] are rough estimates only. As discussed before, their treatment is not consistent with most of the available experimental data. The present transition temperature of 319.7 K appears to be much more reliable.

Our calculated equilibrium temperature for the $\text{ZnSO}_4\cdot 6\text{H}_2\text{O} + \text{ZnSO}_4\cdot \text{H}_2\text{O} + \text{solution} + \text{vapor}$ invariant point is 325.4 K while transition temperatures reported previously^[38,77,84–86,93] cover the range from 322 K to 333 K. This large uncertainty reflects the scatter in both the available solubility data of $\text{ZnSO}_4\cdot \text{H}_2\text{O}$ and the $7\text{H}_2\text{O}\text{-}1\text{H}_2\text{O}$ and $6\text{H}_2\text{O}\text{-}1\text{H}_2\text{O}$ phase boundaries. The calculated invariant point of the assemblage $m\text{-ZnSO}_4\cdot 7\text{H}_2\text{O} + \text{ZnSO}_4\cdot \text{H}_2\text{O} + \text{solution} + \text{vapor}$ of 298.7 K is in good agreement with the transition temperature of 297.95 K obtained by Bury^[91] from interpolation of solubility data.

The largest uncertainties remain for the quadruple invariant point $\text{ZnSO}_4\cdot 7\text{H}_2\text{O} + \text{ZnSO}_4\cdot 6\text{H}_2\text{O} + \text{ZnSO}_4\cdot \text{H}_2\text{O} + \text{vapor}$ which is the lower limit of the stable existence of $\text{ZnSO}_4\cdot 6\text{H}_2\text{O}$. Our model predicts the quadruple point at 275.5 K and $\varphi = 0.424$. In contrast, much higher transition temperatures were derived by Copeland and Short^[93], D’Ans et al.^[39] and D’Ans and Freund^[40] who estimated the transition temperature from solubility data in ternary systems ($\text{H}_2\text{SO}_4\text{-ZnSO}_4\text{-H}_2\text{O}$, $\text{ZnCl}_2\text{-ZnSO}_4\text{-H}_2\text{O}$ and $\text{ZnSO}_4\text{-KCl-H}_2\text{O}$, respectively). Their reported values of (295–299) K are in reasonable agreement with each other. However, such a high transition temperature is clearly not consistent with the available experimental data (cf. Fig. 13) and it was pointed out before that the phase boundaries of both references^[39,40] show large deviations from most experimental data (cf. Fig. 14).

Table 8
Invariant points in the system $\text{ZnSO}_4\text{-H}_2\text{O}$.

Phase assemblage	T / K	$m / \text{mol}\cdot\text{kg}^{-1}$	φ
$7\text{H}_2\text{O} + 6\text{H}_2\text{O} + \text{solution} + \text{vapor}$	311.8	4.328	0.8226
$7\text{H}_2\text{O} + 1\text{H}_2\text{O} + \text{solution} + \text{vapor}$	319.7	4.936	0.7750
$6\text{H}_2\text{O} + 1\text{H}_2\text{O} + \text{solution} + \text{vapor}$	325.4	4.834	0.7982
$m\text{-}7\text{H}_2\text{O} + 6\text{H}_2\text{O} + \text{solution} + \text{vapor}$	298.7	3.950	0.8406
$7\text{H}_2\text{O} + 6\text{H}_2\text{O} + 1\text{H}_2\text{O} + \text{vapor}$	275.5	–	0.4242

Chou and Seal^[41] calculated the quadruple point at 285 K and $\varphi = 0.494$ using standard thermodynamic data tabulated by Wagman et al.^[43] The difference between their values and our modeled values reflect the uncertainty of the scatter in the available experimental data. The uncertainty is the result of the small angle at which the phase boundaries $7\text{H}_2\text{O}\text{-}6\text{H}_2\text{O}$, $7\text{H}_2\text{O}\text{-}1\text{H}_2\text{O}$ and $6\text{H}_2\text{O}\text{-}1\text{H}_2\text{O}$ intersect each other at the transition point. The experimental data of the latter two phase boundaries are significantly scattered and the phase boundaries are less well constrained. Minor deviations in the curves intersecting at a small angle may cause a shift of the intersection point by a large amount.

3.5 Conclusion

An automatic vapor sorption analyzer may be a suitable method for the isopiestic determination of water vapor pressures. However, condensation problems restrict the application of this technique to a rather narrow temperature range and to very concentrated solutions of low water activity. The advantage of the method is the automatic and very fast acquisition of data, about 48 h per value in this study. A comparison to available high quality isopiestic data showed reasonable agreement at 298.15 K. Temperature gradients and inappropriate equilibration times may affect the accuracy of the results at other temperatures.

The Pitzer ion interaction model provides an accurate representation of the thermodynamic properties of aqueous ZnSO_4 over wide ranges of temperature and concentration. To make this possible, an extended form of the original model had to be used, namely by implementation of a third $\beta_{\text{MX}}^{(i)}$ term to represent the ionic strength dependence of the second virial coefficient.

The combination of solubility data with data from hydration–dehydration measurements published in the literature allowed for the calculation of consistent thermodynamic solubility products. With all data combined, the phase change behavior of $\text{ZnSO}_4\cdot\text{H}_2\text{O}$, $\text{ZnSO}_4\cdot 6\text{H}_2\text{O}$ and of orthorhombic and monoclinic $\text{ZnSO}_4\cdot 7\text{H}_2\text{O}$ can be represented in the temperature range 266 K to 378 K. Some of the experimental data show significant scatter and uncertainties remain regarding the solubility product of the monohydrate and the related equilibria, namely the invariant points $\text{ZnSO}_4\cdot 6\text{H}_2\text{O} + \text{ZnSO}_4\cdot\text{H}_2\text{O} + \text{solution} + \text{vapor}$ and $\text{ZnSO}_4\cdot 7\text{H}_2\text{O} + \text{ZnSO}_4\cdot 6\text{H}_2\text{O} + \text{ZnSO}_4\cdot\text{H}_2\text{O} + \text{vapor}$.

From the thermodynamical point of view, a thermochemical energy storage system based on ZnSO_4 hydration/dehydration reactions is not suited for a house heating application where temperatures around 333 K are desired. The stability field of the hexahydrate with an upper temperature limit of 324.67 K is too low. For applications below 320 K, the system would work although high relative humidities are required for a discharge of the storage unit.

4 Thermodynamic properties of $\text{CuSO}_4(\text{aq})$ and phase equilibria in the $\text{CuSO}_4\text{-H}_2\text{O}$ system from 271 K to 373 K²

4.1 Introduction

As for zinc sulfate, copper sulfate has an extensive range of uses in major industries.^[114] Its bactericidal and fungicidal properties for example are used in the treatment of diseases like foot rot of cloven hoofed animals or the preparation of Bordeaux (CuSO_4 , $\text{Ca}(\text{OH})_2$) mixtures as an approved organic preventative fungicide. As a very soluble copper compound, it is also used as a nutrition additive or fertilizer to counteract copper deficiency in animals or soils respectively. In very dilute solutions, it is used to control algae and bacteria growth in water supplies or swimming pools due to its herbicidal and bactericidal nature.

Despite the several applications as an additive in very diverse industries, e.g. in the production of bookbinding pastes and glues, concrete, coloring ingredients, photography, fireworks, it is also used as an analytical reagent for Fehlings and Benedicts solutions and to test for proteins in form of the Biurent reagent. The use as an emetic is obsolete as it is considered as too toxic.

It can be concluded, that copper sulfate is a compound with various fields of application but the major user of copper sulfate solutions is the metal processing industry where it is a key component in the processes of copper recovery from ores, its refining and the electroplating finish. Depending on the initial minerals available, there exist two different extraction methods, hydrometallurgical and pyrometallurgical extraction.^[115] The hydrometallurgical extraction is a growing method where oxidized copper minerals (carbonates, hydrosilicates or sulfates) are used that cannot be roasted. The mineral is first leached with sulfuric acid, then the leach solution is removed while the ions are bound in an Cu-specific organic extractant and back extracted in an aqueous acidic phase to generate an electrolyte solution with a high copper content. In the form of a concentrated copper sulfate solution it can then be used in the electrolysis to produce electroplated copper cathodes.^[116] The pyrometallurgical extraction uses sulfide ore minerals that are not ready for leaching. These are first concentrated by flotation, then smelted to matte (copper enriched sulfide melt) and converted to blister copper by oxidation. Finally, the copper is electrochemically refined to high purity copper cathodes.^[115]

Copper sulfate forms different hydrates of which three occur as stable phases in the $\text{CuSO}_4\text{-H}_2\text{O}$ system. Two of them are the secondary minerals chalcantite ($\text{CuSO}_4\cdot 5\text{H}_2\text{O}$) and bonattite ($\text{CuSO}_4\cdot 3\text{H}_2\text{O}$) which are typically found as oxidation products of sulfide minerals such as chalcopyrite (CuFeS_2).^[117] Bonattite is a rare mineral and its tendency to form chalcantite by hydration is in agreement with the chalcantite stability field^[37,117] The monohydrate is found in nature as $(\text{Cu},\text{Fe})\text{SO}_4\cdot \text{H}_2\text{O}$ (poitevinite) with a Cu:Fe ratio close to 1:1.^[118] Apart from the three stable hydrates, there also exists the heptahydrate $\text{CuSO}_4\cdot 7\text{H}_2\text{O}$ (boothite) which is a very unstable ephemeral mineral that dehydrates rapidly and may only form at low temperature.^[117] For a better understanding, in this work the hydrates will not be addressed with their mineral names but with their amount of water, pentahydrate, trihydrate, monohydrate and anhydrate while the heptahydrate will not be mentioned further.

One goal of this work was the creation of the phase diagram of the binary system $\text{CuSO}_4\text{-H}_2\text{O}$ to establish a thermodynamic groundwork to enable a forecast of its suitability as a material to be used in thermochemical heat storage through solid–gas reaction and to predict possible experimental conditions for future investigations. Recent studies have shown, that CuSO_4 is capable of cycling but the optimal conditions have not been established yet^[119], therefore, it was considered as too slow.^[12] Its theoretical energy density of 2.17 GJ m^{-3} for the hydration from the monohydrate to the pentahydrate is comparable with other sulfates like MgSO_4 or ZnSO_4 .

The literature is rich with experimental data of phase boundaries and solubilities. In addition, there are publications evaluating the $5\text{H}_2\text{O-3H}_2\text{O}$ phase boundary thermodynamically^[44,120] and these authors showed, that the compilations of thermodynamic data^[42,43] are not in agreement with each other. Grevel and Majzlan^[44] have derived adjusted parameters for the standard entropies and enthalpies of formation of chalcantite and bonattite at 298.15 K using the experimental data of Chou and Seal.^[120] To get a thoroughly, internally consistent $\varphi\text{-}T$ phase diagram for the different hydrate phases of copper(II) sulfate, the original form of the Pitzer ion interaction model^[23] for 2–2 electrolytes was used. This allowed to merge all available data to a consistent relationship and to calculate metastable phase boundaries, e.g. the deliquescence humidity of the trihydrate below 367 K, where no experimental data are available. As for aqueous copper sulfate solutions, there exists a reasonable database at 298.15 K^[121–123], at 323.15 K^[52] and 373.15 K^[53] as well as at the freezing^[58,60,61] and boiling^[57] temperatures. At 298.15 K, thermal data in form of heat capacities^[124] and heats of dilution^[76,125] are available as well.

As the main objectives of this work are the generation of model parameters $\text{CuSO}_4(\text{aq})$ to be used in the Pitzer ion interaction model and to create the phase diagram of the binary system $\text{CuSO}_4\text{-H}_2\text{O}$, additional measurements were carried out. A Seteram C80 calorimeter was tested if the determined heat capacities between 307 K and 329 K would be accurate enough for the model calculations. The new data were carefully evaluated together with the existing data of $\text{CuSO}_4(\text{aq})$ to establish the ion interaction model parameters in the temperature range 271–373 K. Together with the dissociation humidities and solubility data reported in the literature, the phase boundaries of the pentahydrate, the trihydrate and the monohydrate were determined.

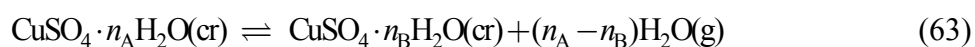
4.2 Theory and Equations

4.2.1 Phase Equilibria

The thermodynamic solubility product of a hydrate of composition $\text{CuSO}_4 \cdot n\text{H}_2\text{O}$ is given by

$$\ln K_n = \ln m(\text{Cu}^{2+}) + \ln m(\text{SO}_4^{2-}) + \ln \gamma(\text{Cu}^{2+}) + \ln \gamma(\text{SO}_4^{2-}) + n \ln a_w \quad (62)$$

where m and γ are the saturation molalities and the activity coefficients of the copper and sulfate ions and a_w is the water activity of the saturated solution. Neglecting the minor influence of the non-ideal behavior of water vapor, at equilibrium, the water activity of a solution is given by Eq. (10) and its relation to the osmotic coefficient ϕ is expressed by Eq. (57) as for ZnSO_4 . The decomposition equilibria between different CuSO_4 hydrates are given by



where subscripts A and B refer to two different hydrates containing n_A and n_B mol of water, respectively. The equilibrium constant of the decomposition reaction is given by Eq. (59) and the equilibrium constant K_{AB} , is also related to the solubility products of the respective hydrates by Eq. (60).

4.2.2 Apparent Molar Heat Capacity

The apparent molar heat capacity ${}^\phi C_p$ describes the part of the heat capacity of the solution carried by the solute, in this case copper sulfate. It is accessible, if the heat capacities of both the solvent and the solute are available and can be defined by the following equation

$${}^\phi C_p = C_p - C_p^\circ / n_2 = C_p - n_1 C_{p,m}^\circ / n_2 \quad (64)$$

where C_p is the heat capacity of the solution, C_p° is the heat capacity and $C_{p,m}^\circ$ is the partial molar heat capacity of the solvent, in this case water. n_1 and n_2 are the amounts of substance of the solvent and the solute respectively.

4.2.3 Ion Interaction Model

To represent the available thermodynamic data for aqueous copper sulfate, the ion interaction approach^[23] was used. A more detailed discussion of the models equations is provided in chapter 2.3. This part restricts to the notification, that despite the various variants of the model^[45,48], aqueous copper sulfate can be described in the temperature range of 271 K to 373 K, using the Pitzer model in its original form. Hence we use only second and third virial coefficients and neglect the ionic strength dependence of the latter. Additionally, the expression for the second virial coefficient is the one originally introduced by Pitzer^[23] for 2–2 electrolytes as shown in Eq. (30) without the term for $\beta_{MX}^{(3)}$.

With the achieved temperature dependent values of the ion interaction parameters the osmotic and the activity coefficients of a copper sulfate solution can be calculated. Using these values, Eq. (62) yields the solubility products using available experimental solubility data.

4.3 Experimental

A caloric investigation of aqueous copper sulfate solutions at different molalities was carried out to measure heat capacities. Integrated in the thermodynamic database of the Pitzer ion interaction model, these data enable an improved basis for the prediction of the electrolytes properties, especially at elevated temperatures. The measurements have been carried out between 306 K and 329 K using temperature steps at intervals of 7.5 K. The heating rate in between steps was set to 0.1 K min^{-1} and copper sulfate solutions with four different molalities close to 0.5, 0.75, 1 and 1.25 mol kg^{-1} were investigated. Copper sulfate solutions were prepared from anhydrous CuSO_4 (Emsure, Merck, Germany) dried in an oven at 523.15 K over 48 h. After the treatment, the anhydrous CuSO_4 was dissolved in doubly distilled water without further purification. For each molality, about 5–6 g of solution (cf. column 2 of Tab. 9) were prepared and the measurements took place in a Setaram C80 calorimeter. The heat capacity of each solution was calculated using the software Calisto Processing (Setaram).

4.4 Results and Discussion

4.4.1 Experimental Results

The results of the calorimetric measurements are listed in Table 9. The apparent molar heat capacities of copper sulfate in solution were calculated using the equation for the heat capacity of water provided by the IAPWS–IF97^[22] and Eq. (64). Figure 15a and b show both C_p and ${}^\phi C_p$ in comparison to the measured values of Akilan.^[124]

Recalculating the values of Akilan^[124] with the IAPWS–IF97 equation^[22] and Eq. (64) resulted in very small deviations for ${}^\phi C_p$ at lower and higher molalities. Therefore the data were used as tabulated by Akilan. In direct comparison to the literature data, Figure 15b shows a systematic deviation of the measured values of this work. Values of the apparent molar heat capacity increase with rising temperature but even though the measurements of this work reflect the trend, the yield was mostly lower values, especially at smaller concentrations. Therefore it is assumed, that this works data show a systematic deviation, hence it will not be used in the continuing data treatment.

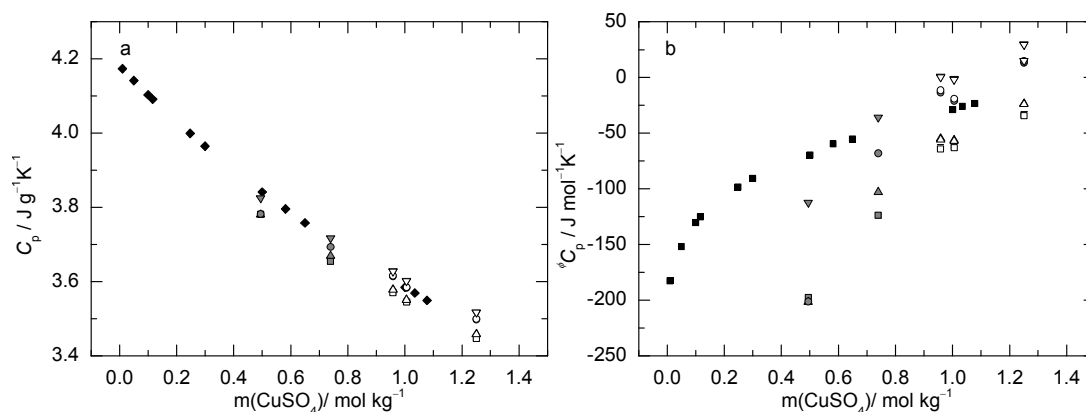


Figure 15: Heat capacities (a) and apparent molar heat capacities (b) of $\text{CuSO}_4(\text{aq})$. Symbols represent experimental data of this works series 1 (grey) and 2 (white) with temperatures around; square(307 K), triangle(314 K), circle(321 K) and inverted triangle (329 K) as well as literature data (black).^[124]

Table 9
 Heat capacities of $\text{CuSO}_4(\text{aq})$.

T K	Solution g	m mol kg^{-1}	C_p $\text{J g}^{-1}\text{K}^{-1}$	${}^\phi C_p^{(a)}$ $\text{J mol}^{-1}\text{K}^{-1}$
Series 1				
306.60			3.782	-200.29
314.02			3.780	-201.96
321.47	5.377	0.494	3.782	-199.66
328.90			3.825	-109.98
306.64			3.655	-125.44
314.05			3.669	-103.03
321.48	5.559	0.740	3.693	-67.13
328.89			3.717	-34.27
306.66			3.571	-64.34
314.08			3.579	-54.94
321.48	5.926	0.958	3.614	-12.82
328.89			3.628	2.10
306.64			3.546	-63.15
314.06			3.551	-56.33
321.48	5.846	1.006	3.583	-20.44
328.91			3.602	-0.06
306.64			3.448	-34.43
314.05			3.459	-23.55
321.48	5.936	1.251	3.498	13.72
328.9			3.518	30.88
Series 2				
306.66			3.570	-65.58
314.08			3.578	-55.95
321.48	5.965	0.958	3.616	-10.67
328.89			3.628	1.51
306.64			3.545	-64.36
314.06			3.551	-57.32
321.48	5.846	1.006	3.585	-18.36
328.91			3.602	-0.64
306.64			3.447	-35.42
314.05			3.458	-23.99
321.48	5.936	1.251	3.500	15.42
328.9			3.517	30.41

^(a) Calculated with the molar heat capacity of water given by the equation of the IAPWS-IF97.^[22]

4.4.2 Parameterization of $\text{CuSO}_4(\text{aq})$

The data used for the determination of the ion interaction parameters for $\text{CuSO}_4(\text{aq})$ are listed in Table 10. There are several studies that reported isopiestic vapor pressure data for $\text{CuSO}_4(\text{aq})$.^[52,53,121–123,126] In the four studies at 298.15 K either NaCl ^[121,123] or KCl ^[122,126] were used as isopiestic reference electrolytes. Osmotic coefficients were calculated from the isopiestic molalities reported in these studies using the equations of Archer for $\text{NaCl}(\text{aq})$ ^[48] and $\text{KCl}(\text{aq})$.^[127] Yang et al.^[52,53] used CaCl_2 as the isopiestic reference in their isopiestic studies at higher temperatures. Osmotic coefficients were calculated from their data using the equation for $\text{CaCl}_2(\text{aq})$ of Holmes et al.^[56] The very careful measurements of Downes and Pitzer^[121] and Miller et al.^[123] at 298.15 K are in excellent agreement with each other and were accepted as reference data. The remaining data at that temperature^[52,122,126] show small but significant systematic deviations and were, consequently, not used in the further data treatment. At higher temperatures (323 K, 373 K) the isopiestic data of Yang et al.^[52,53] are the most important source of data for the determination of the ion interaction parameters.

The only available direct vapor pressure measurements are the very old data tabulated in the compilation of Timmermans.^[82] However, it was found that these data are inconsistent with the remaining data and they were not considered further. Freezing point measurements^[57–61,63,128] provide additional osmotic coefficients at low temperatures. Osmotic coefficients were calculated from the freezing temperatures using the equation of Klotz and Rosenberg.^[62] Full weight in the subsequent treatment was given to the careful measurements of Brown and Prue^[61] at low molalities ($<0.22 \text{ mol kg}^{-1}$) that are also consistent with isopiestic and thermal data as pointed out by Miller et al.^[123] Larger uncertainties are expected for several of the older data. Nonetheless, the freezing temperatures reported by Rüdorff (above 0.4 mol kg^{-1})^[58] and those of Kahlenberg (above 0.2 mol kg^{-1})^[57] are in reasonable agreement with the remaining data and were included in the database with reduced weight. In contrast, the osmotic coefficients calculated from the freezing temperatures of de Coppet^[60] are systematically low. The freezing temperatures at low molalities of Hausrath^[59] and of Hovorka and Rodebush^[128] are considered as less reliable than the more recent data of Brown and Prue^[61] and were, therefore, not used in the least squares fit.

Boiling temperature measurements provide additional data at high temperature.^[57,64,65] Osmotic coefficients were calculated from experimental boiling temperatures using the equation of Smith.^[67] The careful measurements of Plake^[64] at low molalities are consistent with the isopiestic data of Yang et al.^[53] at 373.15 K. In contrast, the older data^[57,65] show larger deviations and were not considered further.

Most of the studies reporting electrochemical cell potentials (emf)^[129–133] were restricted to 298.15 K and were carefully evaluated previously by Miller et al.^[123] We closely followed their evaluation and only those data that were accepted by them are listed in Table 10. In these studies various variants of Cu amalgam electrodes were used together in a cell with an $\text{Hg-Hg}_2\text{SO}_4$ electrode. Though, in general, there is reasonable agreement between the data from different authors, the deviations slightly exceed the expected experimental uncertainties of the respective studies. Following Miller et al.^[123], the data of Wetmore and Gordon^[131] were

treated as reference values and the remaining data were corrected by a constant value ΔE which accounts for differences in the electrode preparations, i.e. a small bias in the standard cells potentials E° . In order to avoid corrections of the solubility of Hg_2SO_4 , only data with CuSO_4 concentrations above 0.025 molal were considered. The corrected data were then used in an isothermal fit to the ion interaction equations at 298.15 K together with the most reliable isopiestic data^[121,123] at the same temperature. Test calculations were carried out both treating the standard potential E° of the $\text{Cu(Hg)|CuSO}_4(\text{m})\text{Hg}_2\text{SO}_4|\text{Hg}$ cell as an adjustable parameter, and, using the recommended value $E^\circ = 0.26970\text{ V}$.^[123] As already noted by others^[28,123], the determination of meaningful values of E° and $\beta_{\text{MX}}^{(2)}$ is difficult and requires very accurate experimental data. The reason is that there are obvious collinearity problems in the least squares regression resulting in significant uncertainties of the estimated parameters E° and $\beta_{\text{MX}}^{(2)}$ which are not independent of each other. This is also confirmed by the present calculations. A minor variation of E° results in a large change of $\beta_{\text{MX}}^{(2)}$ and vice versa. Pitzer and Mayorga^[28] pointed out that the value of $\beta_{\text{MX}}^{(2)}$ has a negligible effect on the osmotic coefficient above 0.1 molal but significantly affects the calculation of activity coefficients at high concentration. Therefore, the determination of the parameter $\beta_{\text{MX}}^{(2)}$ requires very accurate emf data or, preferably, accurate osmotic coefficients at low molalities ($<0.1\text{ mol kg}^{-1}$). In the present treatment, we accepted the value of E° recommended by Miller et al.^[123] which was found by them to be consistent with the freezing temperatures of Brown and Prue.^[61]

Based on the isothermal fits at 298.15 K it turned out that the data reported by Nielsen and Brown^[129] and by Getman^[130] are more scattered than those of Wetmore and Gordon^[131] and Müller and Reuther.^[132,133] Consequently, the data of the references^[129,130] were not included in the final fit. A residual plot of both isopiestic and emf data at 298.15 K is shown in Figure 16. Electrochemical cell potentials at temperatures different from 298.15 K were not included in the least squares calculations to determine the ion interaction parameters. They were rather used to determine values of E° at the other temperatures as described below.

Available thermal data include heats of dilution^[76,78,125] from (273–298) K and heat capacities^[124,134] at 298.15 K. The heats of dilution of Plake^[78] and those of Lange et al.^[76,125] are consistent with each other and with the activity data and were given full weight in the subsequent treatment. The reported heat capacities do not agree with each other. We accepted the recent careful measurements of Akilan.^[124] In contrast, the heat capacities reported by Kapustinskii et al.^[134] were not consistent with the remaining data and were not considered further. Apparent molar heat capacities were calculated using the value for pure water taken from IAPWS-IF97^[22] ($4.1819\text{ J g}^{-1}\text{ K}^{-1}$) as was done in the original work of Akilan.^[124] Test calculations using different values for pure water, particularly with the value of Kell^[135] ($4.1793\text{ J g}^{-1}\text{ K}^{-1}$), resulted in large differences in the calculated apparent molar heat capacities at low molalities. Due to this large effect at the lowest molalities and due to the fact that the value of Kell was widely used in earlier heat capacity studies, we did not use the recommended value of Criss and Millero^[51] for the apparent molar heat capacity of the solute at infinite dilution (${}^\phi C_p^\circ$) but rather treated ${}^\phi C_p^\circ$ as an adjustable parameter.

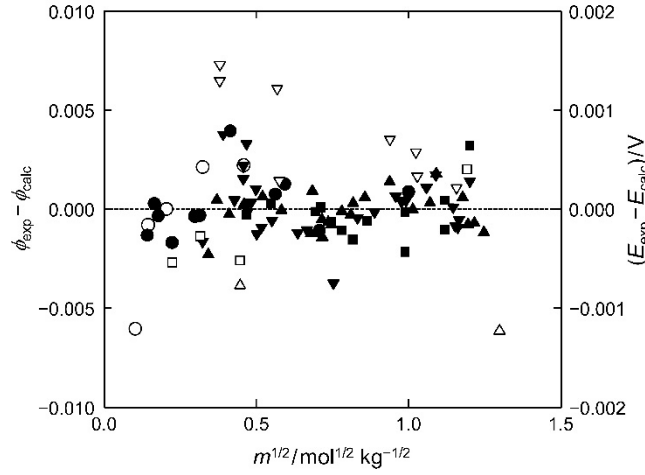


Figure 16: Residual plot of the osmotic coefficients (triangles and inverted triangles) and the cell potentials (circles and squares) at 298.15 K; symbols have the following meaning: black triangles^[121], inverted black triangles^[123], white triangles^[52], inverted white triangles^[122], black circles^[131], black squares^[132,133], white circles^[130] and white squares.^[129] One value of Nielsen and Brown^[129] and one of Getman^[130] with larger deviations ($\Delta E = 0.003$ V and $\Delta E = 0.006$ V, respectively) are not shown. Data plotted as white symbols were not included in the least squares fit.

The final database used in the least squares treatment covers the temperature range (270–377) K. First, the coefficients q_1 of Eq. (50) were fixed for each of the parameters $\beta_{\text{MX}}^{(0)}$, $\beta_{\text{MX}}^{(1)}$, $\beta_{\text{MX}}^{(2)}$ and C_{MX}^ϕ in the isothermal fit at 298.15 K as described before. Subsequently, the temperature dependence of the interaction parameters as given by the coefficients q_2 – q_5 of Eq. (8) was determined in a single weighted least squares fit including the activity data at other temperatures and the thermal data as listed in Table 10. To weight the different types of experimental data the estimated standard errors listed in column 5 of Table 10 were used. Error estimates are based on reported uncertainties, the scatter of each data set and the compatibility with the remaining data sets. The final model parameters are summarized in Table 11 and the resulting standard errors of the fit are listed in column 6 of Table 10.

A residual plot of the osmotic coefficients from isopiestic measurements at 323.15 K and 373.15 K and from freezing and boiling temperatures is shown in Figure 17. In all cases, there is agreement to within the expected experimental uncertainty for the data that were included in the least squares fit. As mentioned before, the cell potentials at temperatures different from 298.15 K were not included in the least squares treatment. However, the cell potentials E were used together with the final model parameters to determine the standard potentials E° according to:

$$E = E^\circ - RT/F \ln(m/m^\circ) - RT/F \ln \gamma_\pm \quad (65)$$

A simple linear temperature dependence of the form was used to represent the temperature dependence of E° :

$$E_T^\circ = E_{298.15\text{K}}^\circ + q(T - T_R) / T_0 \quad (66)$$

Here, $E_{298.15\text{K}}^\circ = 0.26970$ V, the value recommended by Miller et al.^[123], and $q = (-0.00084 \pm 0.00001)$ V was determined by least squares regression of the values of E_T°

calculated with Eq. (65) using the parameters listed in Table 11 to calculate $\ln\gamma_{\pm}$. Deviations between calculated and measured cell potentials are higher than in the isothermal fit at 298.15 K and are slightly larger than the expected experimental uncertainty of this cell (0.2 mV, cf. Tab. 10).

Though a minor inconsistency between the heats of dilution and the apparent molar heat capacities was noted, there is also very good agreement between the model calculated heats of dilution and apparent molar heat capacities and the experimental data^[76,78,124,125] which are reproduced by the model equations to within the expected experimental error (cf. Tab. 10). The least squares estimated value of the partial molar heat capacity of the solute at infinite dilution at 298.15 K is $-282.6 \text{ J K}^{-1} \text{ mol}^{-1}$ which may be compared with the sum of the ionic standard partial molar heat capacities recommended by Criss and Millero^[51] ($-300.2 \text{ J K}^{-1} \text{ mol}^{-1}$). As mentioned before, the difference between these values largely reflects the differences in the calculation of apparent molar heat capacities at low molalities resulting from different values of the heat capacity of pure water.

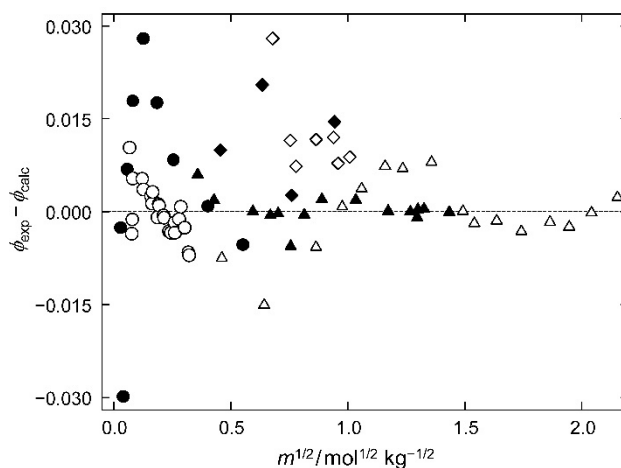


Figure 17: Residual plot of the osmotic coefficients at temperatures different from 298.15 K. Triangles represent isopiestic data at 323.15 K^[52] (black) and 373.15 K^[53] (white); freezing temperature data are shown as white circles^[61], black diamonds^[57] and white diamonds^[58]; black circles represent boiling temperature data^[64]; all data shown were used in least squares fit.

Table 10

 Literature sources for activities and thermal properties of $\text{CuSO}_4(\text{aq})$.

Property ^(a)	T/K	$m/\text{mol kg}^{-1}$	$N^{(b)}$	$\sigma_{\text{est}}^{(c)}$	$\sigma_{\text{fit}}^{(c)}$	Reference
$\phi(\text{isop.})$	298.15	0.2, 1.7	0 (2)	0.005	0.0050	[52]
$\phi(\text{isop.})$	323.15	0.13–2.06	15 (15)	0.005	0.0028	[52]
$\phi(\text{isop.})$	373.15	0.21–4.87	16 (17)	0.005	0.0054	[53]
$\phi(\text{isop.})$	298.15	0.12–1.56	24 (24)	0.002	0.0009	[121]
$\phi(\text{isop.})$	298.15	0.15–1.34	0 (8)	0.005	0.0044	[122]
$\phi(\text{isop.})$	298.15	0.11–1.44	27 (27)	0.002	0.0015	[123]
$\phi(\text{isop.})$	298.15	0.1–1.4	0 (12)	0.006	0.0057	[126]
$\phi(\text{f.t.})$	271.58–272.85	0.12–0.89	4 (5)	0.05	0.0087	[57]
$\phi(\text{f.t.})$	271.35–272.5	0.39–1.02	7 (8)	0.05	0.0085	[58]
$\phi(\text{f.t.})$	273.14	0.0002–0.015	0 (22)	0.03	0.030	[59]
$\phi(\text{f.t.})$	269.25–272.43	0.39–1.7	0 (7)	0.05	0.031	[60]
$\phi(\text{f.t.})$	272.93–273.14	0.005–0.10	23 (23)	0.005	0.0046	[61]
$\phi(\text{f.t.})$	271.41–272.98	0.07–1.19	0 (6)	0.1	0.051	[63]
$\phi(\text{f.t.})$	273.12–273.15	0.001–0.01	0 (6)	0.05	0.035	[128]
$\phi(\text{b.t.})$	373.24–377	0.21–4.62	0 (16)	0.1	0.046	[57]
$\phi(\text{b.t.})$	373.15–373.29	0.0008–0.3	9 (9)	0.02	0.036	[64]
$\phi(\text{b.t.})$	373.65–377.35	1.33–5.15	0 (9)	0.1	0.045	[65]
$E(\text{emf})$	298.15	0.05–1.38	0 (5)	0.2	0.5	[129]
$E(\text{emf})$	298.15	0.04–0.21	0 (6)	0.2	0.5	[130]
$E(\text{emf})$	288.2–318.1	0.02–1	26 (26)	0.2	0.3–1	[131]
$E(\text{emf})$	284.65–323.15	0.51–1.25	17 (17)	0.2	0.1–0.5	[132]
$E(\text{emf})$	283.15–323.15	0.22–1.44	24 (24)	0.2	0.3–1	[133]
${}^\phi L(\Delta_{\text{dil}}H)$	298.15	0.003–0.1	19 (19)	0.2	0.19	[76]
${}^\phi L(\Delta_{\text{dil}}H)$	273.4–294.9	0.025–0.25	10 (18)	0.2	0.07–0.14	[78]
${}^\phi L(\Delta_{\text{dil}}H)$	298.15	0.06–1.22	7 (7)	0.2	0.27	[125]
${}^\phi C_p$	306.6–328.86	0.49–1.25	0 (32)	0.15	0.07	This work
${}^\phi C_p$	298.15	0.01–1.08	12 (12)	0.005	0.010	[124]
${}^\phi C_p$	298.15	0.26–0.88	0 (5)	0.025	0.036	[134]

(a) Quantity and experimental technique (isop.: isopiestic; v.p.: vapor pressure; f.t.: freezing temperature; b.t.: boiling temperature; emf: electrochemical cell potentials).

(b) Number of data used in fit (total number of measurements in brackets).

(c) The units of the standard errors σ_{est} and σ_{fit} are mV for E , $\text{kJ}\cdot\text{mol}^{-1}$ for ${}^\phi L$ and $\text{kJ}\cdot\text{mol}^{-1}\cdot\text{K}^{-1}$ for ${}^\phi C_p$.

Table 11

Parameters of Eq. (50) for the temperature dependence of the ion interaction parameters for $\text{CuSO}_4(\text{aq})$; parameter q_5 was not required to reproduce the experimental data ($q_5 = 0$).

	$\beta^{(0)}$	$\beta^{(1)}$	$\beta^{(2)}$	C^ϕ
q_1	2.085622E-01	2.658671E+00	-5.829201E+01	1.924375E-02
q_2	-3.046663E+01	-5.339021E+04	0	3.097869E+01
q_3	0	-3.457024E+02	1.469412E+03	0
q_4	0	5.715721E-01	-5.365478E+00	0

4.4.3 Solubility Products of $\text{CuSO}_4 \cdot n\text{H}_2\text{O}$

Similar to the work on the system of $\text{ZnSO}_4\text{-H}_2\text{O}$, solubility data and equilibrium relative humidities have been evaluated to conclude a consistent relationship between the two types of data utilizing Eqs. (60) and (62). Available literature data of solubilities and equilibrium relative humidities are listed in Table 12 and Table 13, respectively. First, solubility products were calculated from solubility data using Eq. (62). The activity coefficients needed and water activities of the saturated solutions of $\text{CuSO}_4 \cdot n\text{H}_2\text{O}$ were calculated with the ion interaction parameters listed in Table 11.

The solubility diagram is shown in Figure 18. The pentahydrate has the largest field of stability in the temperature range from 273 K – 373 K followed by a small increment of the trihydrate. In general, the available solubility data of the pentahydrate are in good agreement and could be used as a very good initial position for the determination of the solubility products of the lower hydrates.

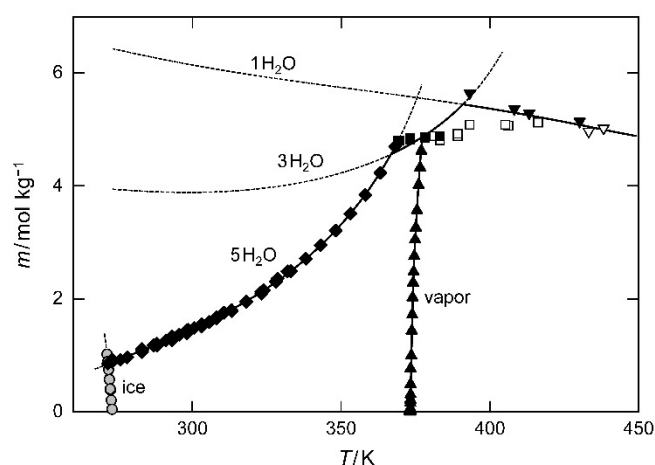


Figure 18: Solubilities in the system $\text{CuSO}_4\text{-H}_2\text{O}$. Symbols represent experimental solubility data taken from the literature that were either used (black) or rejected (white) in the least squares fit (see Table 12); diamonds: $\text{CuSO}_4 \cdot 5\text{H}_2\text{O}$ (chalkanthite); squares: $\text{CuSO}_4 \cdot 3\text{H}_2\text{O}$ (bonattite); inverted: $\text{CuSO}_4 \cdot 1\text{H}_2\text{O}$; grey circles and black triangles depict freezing and boiling temperatures, respectively. Solid lines represent calculated stable solubilities, freezing-point depressions and boiling point elevations. Metastable solubilities are shown as dashed lines.

Table 12
Sources of solubility data in the system $\text{CuSO}_4\text{-H}_2\text{O}$.

Phase ^(a)	<i>T</i> /K	N ^(b)	Reference
5 H ₂ O	298.15	1 (1)	[125]
5 H ₂ O	273.15–373.15	0 (11)	[136]
5 H ₂ O	273.15–327.15	0 (4)	[137]
5 H ₂ O	273.15	0 (1)	[138]
5 H ₂ O	288.15	0 (1)	[139]
5 H ₂ O	284.15–287.15	0 (3)	[140]
5 H ₂ O	273.15–363.15	6 (10)	[141] ^(c)
5 H ₂ O	298.15	1 (1)	[142]
5 H ₂ O	273.15–353.15	0 (24)	[143]
3 H ₂ O	373.15–413.15	0 (8)	
1 H ₂ O	433.15–453.15	0 (4)	
5 H ₂ O	291.15	1 (1)	[144]
5 H ₂ O	288.15	1 (1)	[145]
5 H ₂ O	289.85	0 (1)	[146]
5 H ₂ O	273.15–293.15	5 (5)	[147]
5 H ₂ O	303.15	0 (1)	[148]
5 H ₂ O	273.15, 308.15	2 (2)	[149]
5 H ₂ O	285.15, 298.15	1 (3)	[150]
5 H ₂ O	286.95–331.95	7 (7)	[151]
5 H ₂ O	271.75–373.15	0 (13)	[152]
5 H ₂ O	273.15–310.65	3 (3)	[153]
5 H ₂ O	288.15–298.15	11 (11)	[154]
3 H ₂ O	370.15	0 (1)	[155]
5 H ₂ O	273.15	1 (1)	[156]
5 H ₂ O	273.15–328.15	2 (3)	[157]
5 H ₂ O	273.15–328.15	0 (4)	[158]
5 H ₂ O	273.15–328.15	1 (2)	[159]
5 H ₂ O	271.65–369.05	23 (23)	[160]
3 H ₂ O	369.05–383.15	5 (5)	
5 H ₂ O	288.15–308.15	3 (3)	[161]
1 H ₂ O	393.15–461.15	5 (5)	[162]
5 H ₂ O	293.15–308.15	7 (7)	[163] ^(d)

^(a) 5 H₂O: $\text{CuSO}_4 \cdot 5\text{H}_2\text{O}$ (chalkanthite), 3 H₂O: $\text{CuSO}_4 \cdot 3\text{H}_2\text{O}$ (bonattite), 1 H₂O: $\text{CuSO}_4 \cdot \text{H}_2\text{O}$.

^(b) Number of data used in regression (Number of experimental data).

^(c) nature of solid phase not given in the original paper.

^(d) Values adopted from the compilation of Timmermans.^[82]

Table 13

 Sources of experimental data for the equilibrium humidities in the system $\text{CuSO}_4\text{-H}_2\text{O}$.

Phase boundary	T/K	$N^{(a)}$	Reference
$5\text{H}_2\text{O-3H}_2\text{O}$	287.1–312.85	7 (7)	[96]
$5\text{H}_2\text{O-3H}_2\text{O}$	283.15–373.15	0 (2)	[98]
$3\text{H}_2\text{O-1H}_2\text{O}$	303.15–373.15	0 (2)	
$1\text{H}_2\text{O-Anhydrous}$	436.15–493.15	0 (2)	
$5\text{H}_2\text{O-3H}_2\text{O}$	307.35	1 (1)	[99]
$5\text{H}_2\text{O-3H}_2\text{O}$	290.65	0 (1)	[100]
$3\text{H}_2\text{O-1H}_2\text{O}$	290.95	0 (1)	
$5\text{H}_2\text{O-3H}_2\text{O}$	298.15	0 (1)	[101]
$3\text{H}_2\text{O-1H}_2\text{O}$	298.15	0 (1)	
$1\text{H}_2\text{O-Anhydrous}$	298.15	0 (1)	
$5\text{H}_2\text{O-3H}_2\text{O}$	298.15	1 (1)	[104]
$5\text{H}_2\text{O-3H}_2\text{O}$	278.68	0 (1)	[103]
$3\text{H}_2\text{O-1H}_2\text{O}$	278.77	0 (1)	
$5\text{H}_2\text{O-3H}_2\text{O}$	293.15	2 (2)	[110]
$5\text{H}_2\text{O-3H}_2\text{O}$	297.21–341.17	4 (4)	[120]
$5\text{H}_2\text{O-3H}_2\text{O}$	351–372.75	0 (5)	[164]
$5\text{H}_2\text{O-3H}_2\text{O}$	292.95–327.25	0 (10)	[165]
$5\text{H}_2\text{O-3H}_2\text{O}$	288.15	0 (1)	[166]
$5\text{H}_2\text{O-3H}_2\text{O}$	289.35–325.05	0 (7)	[167]
$3\text{H}_2\text{O-1H}_2\text{O}$	308.35–343.45	0 (7)	
$3\text{H}_2\text{O-1H}_2\text{O}$	316.15–323.15	0 (2)	[168]
$5\text{H}_2\text{O-3H}_2\text{O}$	292.05	0 (1)	[169]
$1\text{H}_2\text{O-Anhydrous}$	290.95	0 (1)	
$5\text{H}_2\text{O-3H}_2\text{O}$	355.2–373.7	0 (2)	[170]
$5\text{H}_2\text{O-3H}_2\text{O}$	293.25–299.05	0 (2)	[171]
$5\text{H}_2\text{O-3H}_2\text{O}$	283.15–303.15	0 (3)	[172]
$3\text{H}_2\text{O-1H}_2\text{O}$	303.15–313.15	0 (3)	
$5\text{H}_2\text{O-3H}_2\text{O}$	298.15	1 (1)	[173]
$1\text{H}_2\text{O-Anhydrous}$	372.15–420.4	5 (5)	[174]
$5\text{H}_2\text{O-3H}_2\text{O}$	298.15	1 (1)	[175]
$5\text{H}_2\text{O-3H}_2\text{O}$	298.15	1 (1)	[176]
$3\text{H}_2\text{O-1H}_2\text{O}$	298.15	1 (1)	
$5\text{H}_2\text{O-3H}_2\text{O}$	298.15–363.19	15 (15)	[177]
$3\text{H}_2\text{O-1H}_2\text{O}$	298.15–353.2	7 (7)	
$5\text{H}_2\text{O-3H}_2\text{O}$	298.15–308.15	3 (3)	[178]
$3\text{H}_2\text{O-1H}_2\text{O}$	298.1–420.4	6 (6)	[179]
$5\text{H}_2\text{O-3H}_2\text{O}$	308.15	1 (1)	[180]
$3\text{H}_2\text{O-1H}_2\text{O}$	308.15	1 (1)	
$1\text{H}_2\text{O-Anhydrous}$	308.15	1 (1)	
$5\text{H}_2\text{O-3H}_2\text{O}$	308.15	1 (1)	[181]
$3\text{H}_2\text{O-1H}_2\text{O}$	308.15	1 (1)	
$1\text{H}_2\text{O-Anhydrous}$	308.15–348.15	2 (2)	
$1\text{H}_2\text{O-Anhydrous}$	298.15	1 (1)	[182]
$5\text{H}_2\text{O-3H}_2\text{O}$	321.5–355.6	8 (8)	[183]

$5\text{H}_2\text{O--3H}_2\text{O}$	298.15	1 (1)	[184]
$3\text{H}_2\text{O--1H}_2\text{O}$	298.15	0 (1)	
$5\text{H}_2\text{O--3H}_2\text{O}$	303.15–363.15	4 (4)	[185]
$3\text{H}_2\text{O--1H}_2\text{O}$	298.15–388.15	7 (7)	
$5\text{H}_2\text{O--3H}_2\text{O}$	295.65–305.45	0 (6)	[186]
$5\text{H}_2\text{O--3H}_2\text{O}$	308.15	0 (1)	[187]
$3\text{H}_2\text{O--1H}_2\text{O}$	308.15	0 (2)	
$5\text{H}_2\text{O--3H}_2\text{O}$	293.15–313.15	5 (5)	[188]

^(a) Number of data used in least squares fit (total number of experimental data).

In an initial evaluation of the solubility data of $\text{CuSO}_4 \cdot 5\text{H}_2\text{O}$ only those data ^[136–140,146,158] with an obvious large deviation from the remaining solubilities were rejected. Due to their large systematic deviations and the scatter of the data at high temperatures the values of Patrick and Aubert^[141], Etard^[143] and those of Agde and Schimmel^[152] were also not considered further although few data points reported by those authors are in agreement with the remaining data at low temperature. The origin of the value of Koppel^[146] is unclear as well as its unit. After the first evaluation, the remaining data show only slight inconsistencies around 273 K. In this work the lower solubilities in the range of $0.88\text{--}0.93 \text{ mol kg}^{-1}$ were accepted.^[141,147,153,159,160] The rejected data are not shown in Figure 18. The solubilities at 298 K^[142] and 293 K^[156] were converted from molarity to molality using the 298 K densities reported by Puchalska et al.^[189], accepting the unit mentioned in the text ($\text{g}/100\text{ccm}$) instead of the table ($\text{g}/200\text{ccm}$) for Trevor.^[142] The remaining data were used to calculate values of the thermodynamic solubility product of the pentahydrate using Eq. (62) and the model calculated activities. The resulting values of $\ln K_5$ are depicted in Figure 19a. At this stage, two additional solubility values at 273.15 K^[153,157] were rejected (white symbols in Fig. Figure 19a). Using the remaining data, the temperature dependence of $\ln K_5$ from 271 K to about 373 K was represented by a fit to Eq. (50) yielding the coefficients listed in Table 14.

The only existing solubility data for the trihydrate are in the temperature range from 373 K to 430 K. In addition, with the known solubility products of the pentahydrate, the experimental dissociation relative humidities of the $\text{CuSO}_4 \cdot 5\text{H}_2\text{O--CuSO}_4 \cdot 3\text{H}_2\text{O}$ dissociation equilibrium provide additional data for the determination of the solubility product $\ln K_3$ of the trihydrate according to Eq. (60). The data reported by Frowein^[96], Carpenter and Jette^[177], Sano^[183], Collins and Menzies^[185], Hepburn^[188] and Chou and Seal^[120] are reasonably consistent with each other and cover a broad temperature range. They were included in the least squares treatment together with few additional values from other studies as listed in Table 13.

Values of $\ln K_3$ calculated from solubility data and from the dissociation humidities are shown in Figure 19b. There is an obvious inconsistency between the two types of data around (263–269) K. A fit of the data to Eq. (50) yielded the coefficients listed in Table 14 represented by the solid curve in Figure 19b. The calculated dissociation humidities are in excellent agreement with literature solubilities (cf. Fig. 20), the agreement with the solubilities reported by Miles and Menzies^[160] is less well but still acceptable (cf. Fig 18). As mentioned before, the data of Etard^[143] are expected to be systematically low.

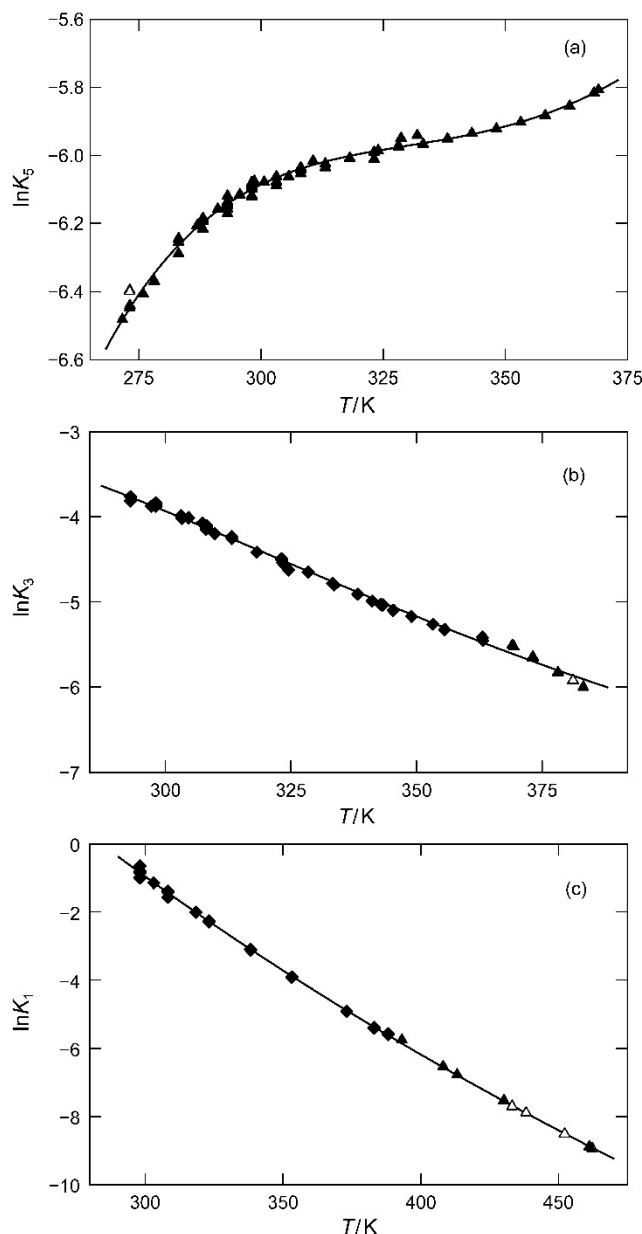


Figure 19: Thermodynamic solubility products of $\text{CuSO}_4 \cdot 5\text{H}_2\text{O}$ (a), $\text{CuSO}_4 \cdot 3\text{H}_2\text{O}$ (b) and $\text{CuSO}_4 \cdot \text{H}_2\text{O}$ (c) calculated from solubilities (triangles) and from dissociation equilibrium humidities (diamonds); only data shown as black symbols were used in the least squares fit.

Solubility data of the monohydrate are only available from two very old sources^[143,162] at temperatures above 393 K but there is a reasonable data base for the dissociation equilibria $\text{CuSO}_4 \cdot 3\text{H}_2\text{O} - \text{CuSO}_4 \cdot \text{H}_2\text{O}$. The values reported by Carpenter and Jette^[177], Menzies and Hitchcock^[179] and Collins and Menzies^[185] cover the temperature range from (298–420) K and are in excellent agreement with each other. These data together with three additional values^[176,180,181] lead to values of $\ln K_1$ that are consistent with those calculated from the solubility data (cf. Fig. 19c) and were used to determine the parameters of Eq. (50) for the monohydrate that are listed in Table 14. Using these parameters, the calculated solubilities are in very good agreement with the experimental data.

Table 14

Parameters of Eq. (50) for the temperature dependence of the logarithmic thermodynamic solubility products.

	$\text{CuSO}_4\cdot 5\text{H}_2\text{O}$	$\text{CuSO}_4\cdot 3\text{H}_2\text{O}$	$\text{CuSO}_4\cdot \text{H}_2\text{O}$	$\text{CuSO}_4^{(a)}$
q_1	-6.09837E+00	-3.88918E+00	-8.43798E-01	5.40313E+00
q_2	-5.01273E+04	-1.98427E+04	-1.34904E+03	0
q_3	-3.03742E+02	-1.23311E+02	-2.22005E+01	0
q_4	4.62454E-01	1.66429E-01	0	-7.32701E-02

(a) These parameters may not be used for solubility calculation of anhydrous CuSO_4 as explained in text.

To conclude, the parameters of Eq. (50), describing the temperature dependence for the solubility products of the penta-, tri- and monohydrate are listed in Table 14. The reliable experimental data cover the temperature ranges of 271 K to 369 K for the pentahydrate, 287 K to 383 K for the trihydrate and 298 K to 461 K for the monohydrate. These temperature ranges can be used to calculate the phase diagram of the binary system $\text{CuSO}_4\text{--H}_2\text{O}$ which will be discussed in the next section.

4.4.4 Phase Diagram of $\text{CuSO}_4\text{--H}_2\text{O}$

The complete phase diagram of the $\text{CuSO}_4\text{--H}_2\text{O}$ system is shown in Figure 20. There is excellent agreement between calculated and experimental dissociation equilibrium humidities for the $\text{CuSO}_4\cdot 5\text{H}_2\text{O}\text{--CuSO}_4\cdot 3\text{H}_2\text{O}$ and the $\text{CuSO}_4\cdot 3\text{H}_2\text{O}\text{--CuSO}_4\cdot \text{H}_2\text{O}$ phase boundaries. The deviations do not exceed the experimental errors which is confirmed by the root mean square (*rms*) deviations of $\sigma_{\text{rms}}(\varphi) = 0.0085$ and $\sigma_{\text{rms}}(\varphi) = 0.0086$ for the two phase boundaries, respectively. In the case of the $\text{CuSO}_4\cdot 5\text{H}_2\text{O}\text{--CuSO}_4\cdot 3\text{H}_2\text{O}$ boundary, there is also good agreement between the present model and the calculations of both Chou and Seal^[120] and Grevel and Majzlan.^[44] To our knowledge, no modeling studies exist that include the remaining phase boundaries in the system.

Also shown in Figure 20 is the calculated phase boundary for the $\text{CuSO}_4\cdot \text{H}_2\text{O}\text{--CuSO}_4$ transition which is calculated using the experimental data of Siggel^[174], Logan^[180], Menzies and Miles^[181] and of Prutton^[182] (cf. Tab. 13). In principle, this calculation yields the thermodynamic solubility product of anhydrous CuSO_4 and the corresponding parameters of Eq. (50) are listed in Table 14. However, the calculation of metastable solubilities of CuSO_4 would require such a significant extrapolation of our ion interaction equations to very high molalities that such calculations are not recommended. Nonetheless the parameters for $\text{CuSO}_4\cdot \text{H}_2\text{O}$ and CuSO_4 can be used to calculate the dissociation humidities of the $\text{CuSO}_4\cdot \text{H}_2\text{O}\text{--CuSO}_4$ phase boundary from (298–420) K using Eq. (60) ($\sigma_{\text{rms}}(\varphi) = 0.0011$).

There is also excellent agreement between calculated solubilities of $\text{CuSO}_4\cdot 5\text{H}_2\text{O}$ and the best experimental data as indicated by the *rms* error of the saturation molalities of $\sigma_{\text{rms}}(m) = 0.015 \text{ mol kg}^{-1}$. Experimental water activities of saturated solutions (φ_{sat}), i.e. the deliquescence humidities (DRH) of $\text{CuSO}_4\cdot 5\text{H}_2\text{O}$, were not included in the least squares treatment as such data are considered as much less reliable than, for example, isopiestic

data.^[50] Available data^[105,110,181,185,190] are compared to our calculated saturation water activities in Figure 20. Though the agreement may be considered as satisfactory, it is obvious that the experimental values are systematically low by about $\Delta\varphi_{\text{sat}} = 0.01$ compared to the calculated DRH. Since the present calculations are based on both very accurate solubilities and thermodynamic data of $\text{CuSO}_4(\text{aq})$, the calculated saturation humidities are considered much more reliable than the experimental data.

Collins and Menzies^[185] also report saturation humidities for $\text{CuSO}_4\cdot 3\text{H}_2\text{O}$ and $\text{CuSO}_4\cdot \text{H}_2\text{O}$ which are also shown in Figure 20. Again, the experimental values are significantly lower than the calculated ones. In this case, however, it is less obvious which of the data are more reliable. The calculated saturation humidities are affected by the uncertainty regarding the solubility of $\text{CuSO}_4\cdot 3\text{H}_2\text{O}$, particularly at high temperatures. It should be also noted that significant extrapolation of the ion interaction equations for the calculation of the activity coefficients and water activities in the saturated solutions is required. Therefore, the deviations between experimental and calculated values, ranging from $\Delta\varphi_{\text{sat}} = 0.005$ at 373.15 K to $\Delta\varphi_{\text{sat}} = 0.05$ at 398.15 K, seems to reflect the combined uncertainties. Despite of these uncertainties, our calculated transition temperature for the invariant point $\text{CuSO}_4\cdot 3\text{H}_2\text{O} + \text{CuSO}_4\cdot \text{H}_2\text{O} + \text{solution} + \text{vapor}$ is 390.9 K which is in good agreement with the 389.8 K reported by Collins and Menzies.^[185] This transition temperature is also consistent with the strong increase of the $\text{CuSO}_4\cdot 3\text{H}_2\text{O}$ solubility with temperature predicted by the model. In contrast, a much higher transition temperature than determined by Collins and Menzies^[185] is derived from the experimental solubilities of Miles and Menzies^[160] and, particularly, Etard^[143] (cf. Fig. 18).

Finally, our calculated transition temperature for the $\text{CuSO}_4\cdot 5\text{H}_2\text{O} + \text{CuSO}_4\cdot 3\text{H}_2\text{O} + \text{solution} + \text{vapor}$ invariant point at 366.9 K is slightly lower than the value of 389.9 K reported by Collins and Menzies.^[185] Again, this deviation reflects the uncertainties of both the experimental data, especially the solubility of $\text{CuSO}_4\cdot 3\text{H}_2\text{O}$, and the model parameters.

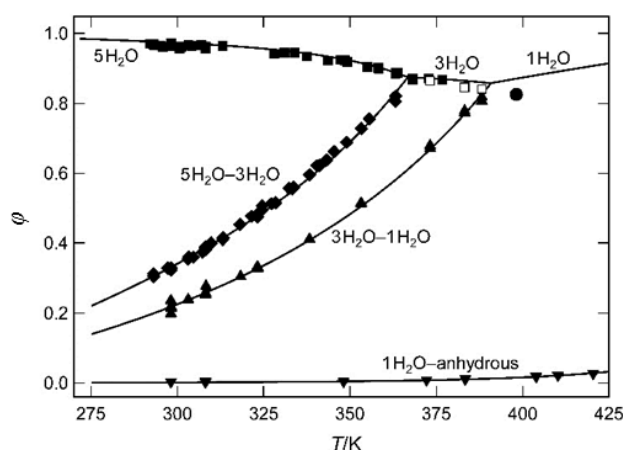


Figure 20: Experimental (symbols) and calculated (curves) hydration–dehydration equilibria (dissociation humidities) and saturation humidities (DRH) in the system $\text{CuSO}_4\text{-H}_2\text{O}$. Symbols represent critically evaluated experimental data of the $\text{CuSO}_4\cdot 5\text{H}_2\text{O}\text{-CuSO}_4\cdot 3\text{H}_2\text{O}$ equilibrium ($5\text{H}_2\text{O}\text{-}3\text{H}_2\text{O}$: diamonds), the $\text{CuSO}_4\cdot 3\text{H}_2\text{O}\text{-CuSO}_4\cdot \text{H}_2\text{O}$ equilibrium ($3\text{H}_2\text{O}\text{-}1\text{H}_2\text{O}$: triangles), the $\text{CuSO}_4\cdot \text{H}_2\text{O}\text{-CuSO}_4$ equilibrium ($1\text{H}_2\text{O}\text{-anhydrous}$: inverted triangles) and the deliquescence humidities of the penta- ($5\text{H}_2\text{O}$: black squares), tri- ($3\text{H}_2\text{O}$: white squares) and monohydrates ($1\text{H}_2\text{O}$: circle).

Conclusively, the presented phase diagram (cf. Fig. 20) represents a good reproduction of the available experimental data in the range of 273 K to 388 K. The solubility data and deliquescence humidities of the pentahydrate are in excellent agreement as well as the two phase boundaries of the $5\text{H}_2\text{O--3H}_2\text{O}$ and $3\text{H}_2\text{O--1H}_2\text{O}$ equilibria. In addition, the stable $1\text{H}_2\text{O--anhydrous}$ phase boundary is reported as well.

4.5 Conclusion

The Pitzer ion interaction model provides accurate activity coefficients and water activities for aqueous copper sulfate solutions over a wide range of temperature and concentration. This was possible by using the available thermodynamic data of $\text{CuSO}_4(\text{aq})$ from an internally consistent database in the temperature range (268–377) K that can be represented by the original version of the Pitzer ion interaction equations for 2–2 charge type electrolytes. Additional thermochemical data in form of specific heat capacities of $\text{CuSO}_4(\text{aq})$ were measured using a Setaram C80 calorimeter. The results, especially at lower concentration of the investigated solution, are less accurate than in classical flow calorimeters, hence the values were not used in the described data treatment.

The combination of solubility data and decomposition temperatures resulted in internally consistent thermodynamic solubility products of the penta-, tri- and monohydrates in the temperature range from 273 K to 388 K with minor limitations at temperatures above 377 K. In addition, the phase boundary of the $\text{CuSO}_4\cdot\text{H}_2\text{O--CuSO}_4$ equilibrium is reported. The phase diagram of the binary system $\text{CuSO}_4\text{--H}_2\text{O}$ was established enabling a better prediction for experimental conditions in the testing of its suitability as a thermochemical energy storage material.

From the thermodynamical point of view, a thermochemical energy storage system based on CuSO_4 hydration/dehydration reactions is very well suited for a house heating application where temperatures around 333 K are desired. The stability field of the pentahydrate with an upper temperature limit of 367 K and the deliquescence humidity of the monohydrate at 333 K being 19% RH higher than the 5–3 equilibrium at the same temperature, leaves much room for optimizing reaction conditions. Another great advantage is the low relative humidity required for the hydration reaction which is lower than observed for other sulfates.

As an example, if copper sulfate is brought into a porous matrix to create a composite material with a remaining storage density of let's say 60% of the bulk, a density of 1.3 GJ m^{-3} is available. State of the art materials with MgSO_4 are able to store 0.93 GJ m^{-3} ^[15] and are stable during cycling. A single house with 100 m^2 and $120 \text{ kWh m}^{-2} \text{ a}^{-1}$ needs 43.2 GJ a^{-1} that would result in a storage unit with a size of 33.2 m^{-3} . New buildings with optimized insulation usually require less than $50 \text{ kWh m}^{-2} \text{ a}^{-1}$, reducing the size of the storage unit to 13.8 m^{-3} that can easily be fitted in a cellar. Another advantage of copper sulfate is that the hydration to the pentahydrate at 333 K would only stop if the relative humidity in the storage unit drops below 56% RH while the hydration to $\text{MgSO}_4\cdot 6\text{H}_2\text{O}$ requires at least 72% RH.

5 Determination of the thermodynamic properties of $\text{CaSO}_4(\text{aq})$ solution with few available data and definition of the phase boundaries in the System $\text{CaSO}_4\text{--H}_2\text{O}$

5.1 Introduction

Gypsum ($\text{CaSO}_4 \cdot 2\text{H}_2\text{O}$), insoluble anhydrite (CaSO_4) and bassanite ($\text{CaSO}_4 \cdot 0.5\text{H}_2\text{O}$) or α -hemihydrate can be found in various environments as natural occurring minerals since calcium sulfate is the most common sulfate mineral. The binary system $\text{CaSO}_4\text{--H}_2\text{O}$ has been investigated by numerous authors during the last century, mostly with a geochemical interest as it appears with other salts in deposits of marine origin. Clear knowledge about phase stabilities is needed to determine the environmental conditions under which these minerals were formed. In the recent past, the research is focused on industrial processes, e.g. for the hydrometallurgical method, dealing with Ca^{2+} and SO_4^{2-} ions in aqueous solution where knowledge of the precipitation of the phases is needed. Lately, two additional fields joined the research as CaSO_4 hydration on one hand is considered a serious threat to modern civil engineering projects but on the other hand is considered as a potential thermochemical energy storage material.^[11]

The discussion about the transition temperature of gypsum to insoluble anhydrite has a long history starting with the first value at 336 K.^[191] Patridge and White^[192] criticized the value as being too high and suggested a value close to 313 K based on solubility measurements. D'Ans and Höfer^[193] mentioned the highest value at 336.75 K in agreement with Van't Hoff^[191] but corrected it 18 years later.^[194] Hill^[195] and Posnjak^[196] argued, that the phase transition in pure water is located at the lower temperature around 315 ± 2 K on the basis of their careful solubility measurements. D'Ans et al.^[194] critically discussed the large discrepancy and included additional solubility data resulting in the support of the lower transition temperature as suggested by Hill^[195] and Posnjak^[196]. The results of Bock^[197] also agree with the lower value at 315 K. Zen^[198] argued, that the thermodynamic data used by Kelley^[199], resulting in a transition at 313 K, was not internally consistent. Instead, Zen^[198] suggested a temperature of 319 ± 25 K, based on calculated anhydrite solubilities as own solubility measurements failed. Hardie^[200] published the results of his substantial experimental work, naming the transition point to be at 331 ± 2 K. The following publications of Blount and Dockson^[201] as well as Knacke and Gans^[202], supported a higher temperature, naming the value at 329 ± 3 K and 328.65 ± 1.5 K, respectively. In addition to these new higher values, Zdanovskii and Vlasov^[203] as well as Kruchenko and Beremzhanov^[204] published their temperatures to be at 318 K and 319 K respectively. In the work of Innorta et al.^[205], a new transition temperature at 322.65 ± 1.5 K determined by extrapolation of their own anhydrite solubility measurements was published. In a thermodynamic approach, the researchers Weare, Harvie, Eugster, Møller and Greenberg used the ion interaction approach to calculate activity coefficients and water activities in multicomponent systems also containing Ca^{2+} and SO_4^{2-} ions first at 298 K.^[206,207] In 1988, Møller^[208] published the results of a hybrid between the ion interaction

and ion association model, suggested by Whitfield^[209], at temperatures higher than 298 K. A transition point of 322 K was determined through calculated solubilities. In a following attempt Raju and Atkinson^[210] parameterized the thermodynamic quantities of aqueous CaSO_4 and calculated that the transition temperature should be found at 333 K. Azimi^[211] used the mixed solvent electrolyte (MSE) model to predict the solubility of calcium sulfate in the binary system $\text{CaSO}_4\text{-H}_2\text{O}$ and in ternary and quaternary systems for a better characterization of solutions used in hydrometallurgical processes. Here a transition temperature of 313 ± 2 K was found for the gypsum-anhydrite equilibrium.

Despite the ongoing discussion about the transition temperature, the phase transition gained new interest when it takes place in confined spaces leading to the development of damages on constructions like tunnels^[212], a railway bridge^[213] or even parts of a village.^[214] These damages have their origin in the swelling of geological formations containing anhydrite which will hydrate to gypsum when in contact with water. Better knowledge is needed about the conditions under which these swellings take place and what can be done to prevent them.

In this work, a reinvestigation of the binary system $\text{CaSO}_4\text{-H}_2\text{O}$ on a comprehensive analysis of the existing data is carried out. At first a parameterization of aqueous CaSO_4 is achieved for temperatures between 273 K and 373 K to calculate activity coefficients and water activities, using the ion interaction approach of Pitzer.^[23] With these quantities and carefully evaluated solubility data, a thermodynamic consistent phase diagram could be established and was supplemented with additional dissociation humidity data from mixed solutions, which is then discussed with the above mentioned articles. Despite the ongoing discussion about the transition temperature, it is crucial to know its value for an evaluation of what phase change in the $\text{CaSO}_4\text{-H}_2\text{O}$ system is suitable for the reaction as a thermochemical heat storage material as its storage density for, e.g. a soluble anhydrite hydration to gypsum, is already lower (1.52 GJ m^{-3}) as for the previously investigated salts.

5.2 Theory

5.2.1 CaSO_4 Phases

On the first look the system of calcium sulfate and its hydrates looks quite simple. It has three different phases, gypsum ($\text{CaSO}_4 \cdot 2\text{H}_2\text{O}$), bassanite (hemihydrate $\text{CaSO}_4 \cdot 0.5\text{H}_2\text{O}$) and anhydrite. These three phases can crystallize, if CaSO_4 is in contact with water but it has to be said, that hemihydrate is always metastable with respect to gypsum or anhydrite. Of course there are a number of factors that have a significant impact on which phase will crystallize, for example the relative humidity or the temperature as well as additional ions if in a solution.

Hemihydrate can be separated in two varieties, the α - and β -hemihydrate. Produced by the industry, it depends on the surrounding conditions if α - or β -hemihydrate is achieved. The α -hemihydrate crystallizes when dehydrating gypsum under humid conditions, for example at temperatures between 353 K and 393 K hydrothermally in a steam autoclave. The addition of acids or salts can reduce the needed temperature to about 318 K.^[215] The β -hemihydrate forms its crystals during gypsum dehydration under dry conditions, for example in an oven at

temperatures of 333 K in the magnitude of days. With increasing temperature the time needed for dehydration can be reduced to a few hours at about 403 K. The soluble anhydrite, also referred to as γ -anhydrite or A(III), owns the same crystal structure as the hemihydrate.^[216] The crystal water of the hemihydrate is located in cannels, which are embedded in its crystal structure, making the dehydration a rapid process. Depending on the variety of the hemihydrate, the resulting α - or β -A(III) is achieved. Due to its strong hygroscopic behavior, the rehydration is a very fast process that leads to the hemihydrate variety it was gained from if any water vapor is available.^[217]

The natural occurring anhydrite is the insoluble anhydrite, also referred to as β -anhydrite or A(II). According to Posnjak^[196] and Ostroff^[218], insoluble anhydrite does not precipitate directly from gypsum which can only form hemihydrate at the transition temperature at 370.65 ± 1 K. Hence, gypsum represents a persistent metastable phase between the anhydrite and hemihydrate transition point. Natural anhydrite can be found in geological formations of former evaporation sites together with gypsum and other salts.^[219] Under dry climates insoluble anhydrite persists for a very long time and when in contact with liquid water a rehydration to gypsum can occur. If the soluble anhydrite is heated up to 1453 K, the high temperature variety of anhydrous calcium sulfate, the α -anhydrite or A(I) becomes thermodynamically stable.

5.2.2 Phase Equilibria

To predict the solubility products of an electrolyte solution three different types of data are needed. At first the saturation molality of the electrolyte in moles per kg of solvent, in this case water. Second is the water activity of the present solution and at last the activity coefficients of the present cations and the anions. If these values are known at the desired temperatures, the corresponding thermodynamic solubility products, $\ln K_{sp}$, can be calculated using Eq. (67).

$$\ln K_n = \ln m(\text{Ca}^{2+}) + \ln m(\text{SO}_4^{2-}) + \ln \gamma(\text{Ca}^{2+}) + \ln \gamma(\text{SO}_4^{2-}) + n \ln a_w \quad (67)$$

If the solubility products at isothermal conditions are known for the different salt phases, it is possible to calculate $a_{w,eq}$, the water activity at the equilibrium state between the phases, using Eq. (60).

5.3 Results and Discussion

5.3.1 Parameterization of $\text{CaSO}_4(\text{aq})$

In order to calculate the thermodynamic solubility product of calcium sulfate and its hydrates from solubility data, the ion interaction parameters $\beta_{MX}^{(i)}$ and C^ϕ for aqueous calcium sulfate solutions need to be defined. Here, the parameters were calculated for the binary system $\text{CaSO}_4\text{-H}_2\text{O}$ what proved quite difficult. At first there is almost no data at high ionic strengths so the Pitzer equation needs to be extrapolated very far. Further there are no available data at other temperatures than 298 K and 273 K.

Table 15

Parameters of Eq. (50) for the temperature dependence of the ion interaction parameters for $\text{CaSO}_4(\text{aq})$; parameters q_4 and q_5 were not required.

	$\beta^{(0)}$	$\beta^{(1)}$	$\beta^{(2)}$	C^ϕ
q_1	1.95740E-01	3.17495E+00	-5.89024E+01	2.18037E-02
q_2	-1.50689E+02	3.97655E+03	-5.56548E+05	7.44580E+01
q_3	-2.16602E-01	1.56647E+01	-1.90789E+03	8.02029E-02

Refining the plausible method suggested by Raju and Atkinson^[210] an equation for CaSO_4 was developed. This was achieved, estimating that both the activity and osmotic coefficients in supersaturated solutions act similar to other 2-2 sulfate electrolytes, as it was published by Pitzer.^[220] To find a fitting isotherm that can represent the CaSO_4 activity coefficients tabulated^[220] for 298 K, an isotherm close to 333 K of MgSO_4 derived with the parameters from Steiger et al.^[13] showed the best results. Since the MgSO_4 equation^[13] used $\alpha_1=1.3$ and $\alpha_2=15$, the parameters were recalculated to adjust them to $\alpha_1=1.2$ and $\alpha_2=12$. To get temperature dependent parameters, a method suggested by Königsberger^[221] was used, presuming that apparent molar heat capacities and the apparent molar enthalpies of CaSO_4 and MgSO_4 are very similar to each other. Following this suggestion, it was assumed that the parameters for $\beta^{(i)L}$, C^L and $\beta^{(i)J}$, C^J for $\text{CaSO}_4(\text{aq})$ and $\text{MgSO}_4(\text{aq})$ were identical. Combining these two methods yielded the following parameters tabulated in Table 15. The temperature dependency is expressed by Eq. (50).

5.3.2 Solubility Products of $\text{CaSO}_4 \cdot n\text{H}_2\text{O}$

Suitable data for the determination of solubility products of the different phases in the system $\text{CaSO}_4\text{-H}_2\text{O}$ exists only in form of solubility data. The solubility data of the System $\text{CaSO}_4\text{-H}_2\text{O}$ show a large variance and are being strongly discussed in the literature. In this approach to find acceptable values, the solubility data for gypsum, taken from the table of D'Ans^[222] and additional literature (cf. Tab. 16), has been statistically evaluated by erasing all values that deviated more than three times of the standard deviation. This procedure was repeated several times until a recent fit was achieved. For the natural anhydrite another approach was chosen because the elimination based on the standard deviation erased the low solubilities that were, according to their authors^[194,196] the most consistent values. Despite their work, problems with the measurement of anhydrite solubility were also mentioned by Hill^[223] who tried several ways to get anhydrite through dehydration of gypsum in order to get reliable solubility figures. For α -hemihydrate the selection of good data is even more complicated. According to D'Ans et al.^[194] as well as Power and Fabuss^[224], early solubility measurements could have been defective because the investigated phase has been β -hemihydrate or even soluble anhydrite resulting in too high solubilities. In Table 16, the available and selected solubility data from the literature is listed. Supplementary to the literature values, solubility data was collected from the compilation of D'Ans^[222] and Silcock.^[225]

Table 16
 Solubility data for the system $\text{CaSO}_4\text{-H}_2\text{O}$.

Phase ^(a)	<i>T</i> /K	N ^(b)	Reference
0.5H ₂ O	372 – 470	39 (39)	[192]
A(II)	372 – 476	2 (35)	
2H ₂ O	293	1 (1)	[194]
0.5H ₂ O	271 – 356	4 (4)	
A(II)	273	1 (1)	
2H ₂ O	308	1 (1)	[195]
A(II)	298 – 338	4 (18)	
2H ₂ O	273 – 365	16 (16)	[196]
0.5H ₂ O	374	1 (1)	
A(II)	299 – 365	10 (10)	
2H ₂ O	298 – 323	2 (4)	[197]
A(II)	298 – 323	4 (4)	
2H ₂ O	308 – 343	1 (22)	[198]
A(II)	308 – 343	0 (7)	
2H ₂ O	298 – 323	1 (3)	[203]
2H ₂ O	293 – 333	3 (5)	[204]
A(II)	293 – 333	0 (5)	
2H ₂ O	298 – 338	4 (14)	[205]
A(II)	313 – 338	0 (14)	
2H ₂ O	298 – 388	12 (12)	[224]
0.5H ₂ O	318 – 378	4 (4)	
A(II)	318 – 358	6 (6)	
Various	308 – 383	0 (19)	
2H ₂ O	273 – 259	6 (9)	[226]
0.5H ₂ O	291 – 372	0 (2)	
2H ₂ O	299 – 355	1 (2)	[227]
2H ₂ O	295 – 299	3 (3)	[228]
2H ₂ O	273 – 348	11 (11)	[229]
0.5H ₂ O	298 – 337	0 (2)	
2H ₂ O	298 – 316	1 (2)	[230]
2H ₂ O	298	1 (1)	[231]
2H ₂ O	298	1 (1)	[232]
2H ₂ O	291 – 373	3 (3)	[233]
A(II)	373 – 471	1 (3)	
2H ₂ O	298	3 (3)	[234]
A(II)	293	0 (1)	[235]
2H ₂ O	313 – 373	3 (3)	[223]
A(II)	373	1 (1)	
2H ₂ O	298 – 348	3 (3)	[236]
A(II)	348	1 (1)	
2H ₂ O	298 – 348	4 (4)	[237]
2H ₂ O	298 – 308	2 (2)	[238]
A(II)	298	1 (1)	
2H ₂ O	293 – 323	7 (7)	[239]
A(II)	293 – 308	4 (4)	

$2\text{H}_2\text{O}$	358 – 373	3 (3)	[240]
$2\text{H}_2\text{O}$	313 – 333	3 (3)	[241]
$0.5\text{H}_2\text{O}$	398	3 (3)	
$2\text{H}_2\text{O}$	298 – 368	6 (6)	[242]
A(II)	308 – 358	0 (4)	
$2\text{H}_2\text{O}$	301 – 363	5 (6)	[243]
$2\text{H}_2\text{O}$	274 – 363	10 (12)	[244]
$2\text{H}_2\text{O}$	298 – 358	2 (5)	[245]
A(II)	373	0 (1)	
$2\text{H}_2\text{O}$	298	1 (1)	[246]
$0.5\text{H}_2\text{O}$	298	0 (1)	
A(II)	298	0 (1)	
Various	298	0 (5)	
$2\text{H}_2\text{O}$	298 – 368	1 (4)	[247]
$0.5\text{H}_2\text{O}$	298 – 368	0 (4)	
$2\text{H}_2\text{O}$	323	1 (1)	[248]
A(II)	323	0 (1)	
$2\text{H}_2\text{O}$	298 – 323	1 (2)	[249]
A(II)	398 – 423	0 (2)	[250]
$2\text{H}_2\text{O}$	333	0 (1)	[251]
$2\text{H}_2\text{O}$	313	1 (1)	[252]
$2\text{H}_2\text{O}$	303	0 (1)	[253]
$2\text{H}_2\text{O}$	308	0 (1)	[254]
$2\text{H}_2\text{O}$	283 – 353	5 (5)	[255]

(a) $2\text{H}_2\text{O}$: $\text{CaSO}_4 \cdot 2\text{H}_2\text{O}$ (gypsum), $0.5\text{H}_2\text{O}$: $\alpha\text{-CaSO}_4 \cdot 0.5\text{H}_2\text{O}$ (bassanite),
 A(II): CuSO_4 (insoluble anhydrite), Various: umbrella term for A(I), soluble anhydrite
 A(III) and/or $\beta\text{-CaSO}_4 \cdot 0.5\text{H}_2\text{O}$.

(b) Number of data used in regression (Number of experimental data).

In the case of the System $\text{CaSO}_4\text{-H}_2\text{O}$, opposite to the other systems investigated in this work, measurements of equilibrium humidities are not available for the determination of solubility products. Therefore, this work relies entirely on solubility data of the investigated phases. The whole and sorted solubility data are pictured in Figures 21a and b respectively.

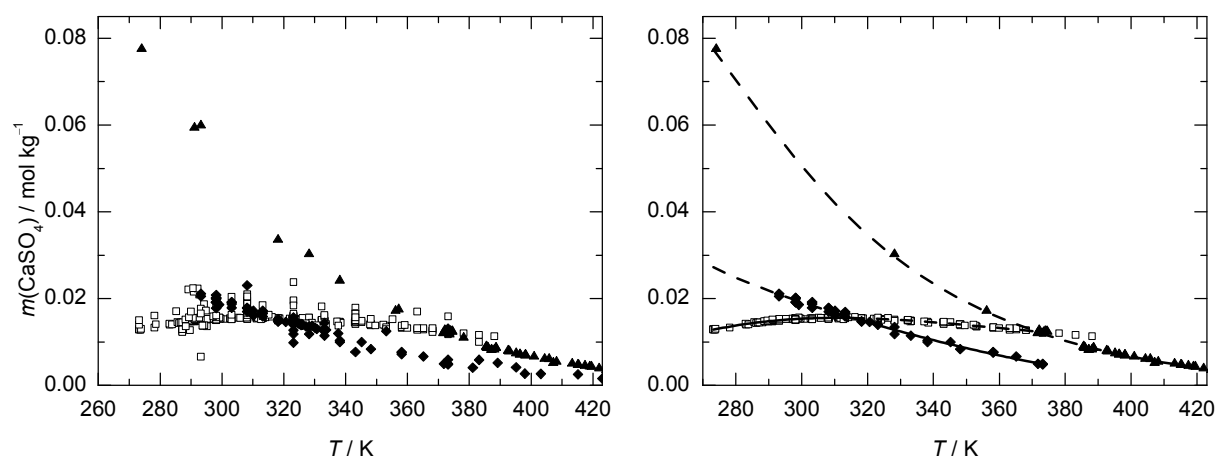


Figure 21: a) Solubilities in the system $\text{CaSO}_4\text{-H}_2\text{O}$. b) Solubility data of the same system after evaluation (see text). Symbols in both diagrams have the following meaning: open squares: $\text{CaSO}_4 \cdot 2\text{H}_2\text{O}$ (gypsum); solid diamonds: CaSO_4 (insoluble anhydrite); solid triangles: $\alpha\text{-CaSO}_4 \cdot 0.5\text{H}_2\text{O}$ (bassanite). Solid and dashed lines represent calculated stable and metastable solubilities respectively, based on the evaluated solubility products.

Table 17

Parameters of Eq. (50) for the temperature dependence of the logarithmic thermodynamic solubility products of the CaSO_4 phases gypsum, α -hemihydrate and insoluble anhydrite.

	$\text{CaSO}_4 \cdot 2\text{H}_2\text{O}$	$\text{CaSO}_4 \cdot 0.5\text{H}_2\text{O}$	CaSO_4
q_1	-1.05746E+01	-9.09670E+00	-1.02595E+01
q_2	-2.79391E+04	-1.81110E+04	1.82270E+04
q_3	-1.41335E+02	-9.37963E+01	1.41390E+02
q_4	1.59465E-01	8.54392E-02	-2.89558E-01

With the sorted solubility data and the previously obtained pitzer parameters for aqueous CaSO_4 solutions, the development of equations for the solubility products of the phases gypsum, insoluble anhydrite and α -hemihydrate according to Eq. (67) is possible. The parameters are listed in Table 17 and are to be used in Eq. (50).

5.3.3 Equilibria in Mixed Solutions

With the above determined parameters for the solubility products of CaSO_4 phases, it is possible to determine the hydration–dehydration equilibrium humidities. As this calculation relies entirely on solubility data, an additional method for the validation is preferable. A method has been successfully used for the system $\text{CaSO}_4\text{-H}_2\text{O}$ by Zen^[198] and Hardie^[200] who suggested that the low solubility of CaSO_4 and its according effect on the water activity of the investigated solution is negligible in comparison to the dominant influence of the present salt or acid. This means, that mixtures containing CaSO_4 can be treated as simple binary systems. An example is pictured in Figure 22 with the solubilities of calcium sulfate in calcium chloride solutions at 298 K.^[256]

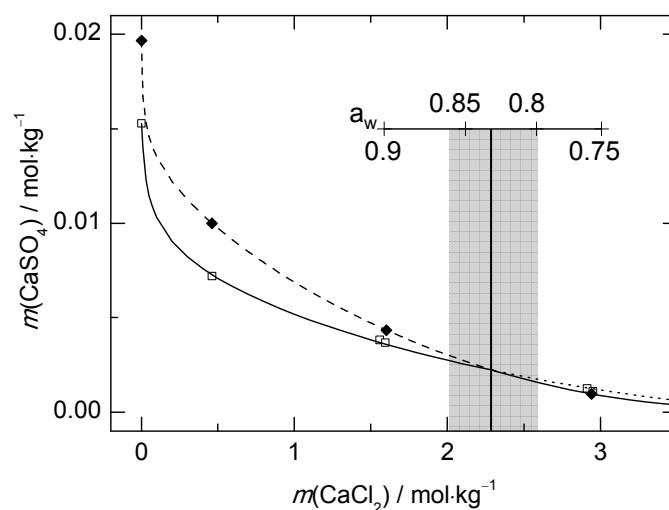


Figure 22: Solubility of $\text{CaSO}_4 \cdot 2\text{H}_2\text{O}$ (gypsum) and CaSO_4 (insoluble anhydrite) in solutions of CaCl_2 at 298 K measured by Mel'nikova.^[256] Solid square symbols represent solubilities of gypsum and solid diamonds denote insoluble anhydrite. The dashed, dotted and solid curves represent calculated solubilities of metastable insoluble anhydrite, metastable gypsum and the corresponding stable phase. The curves intersect with a very low angle at a CaCl_2 concentration of $2.31 \pm 0.3 \text{ mol} \cdot \text{kg}^{-1}$. At this point the water activity of the given solution is 0.83 ± 0.032 calculated with the equation of Rard et al.^[257]

The change in stability of the corresponding CaSO_4 phases is determined by the intersection of the respective solubilities as a function of the CaCl_2 concentration. From the determined CaCl_2 concentration, the water activity of a pure CaCl_2 solution can be calculated revealing the phase transition of the investigated solids at the investigated temperature.

5.3.4 Phase Diagram

The phase transition behavior of CaSO_4 in matters of relative humidity and temperature is shown in the phase diagram (cf. Fig. 23). Below 315 ± 2 K gypsum can be identified as the thermodynamically stable phase and at higher temperatures gypsum is relieved by insoluble anhydrite. As a metastable phase, α -hemihydrate is formed at temperatures higher than 371.95 K. Even though insoluble anhydrite is considered stable above 315 K its formation is kinetically hindered.^[219] This phenomenon can be explained as follows. For the formation of persistent insoluble anhydrite, nuclei in a supersaturated solution are needed. By taking a close look on the solubility diagram (cf. Fig. 21) it is obvious, that close to the transition point the solubility of gypsum is only marginal higher than that of anhydrite. This means, that supersaturation of the solution with respect to gypsum and therefore formation of gypsum nuclei can easily occur. Hence, the calcium and sulfate ions in solution will readily crystallize as gypsum so measurements close to the transition point are very difficult and can lead to erroneous results.

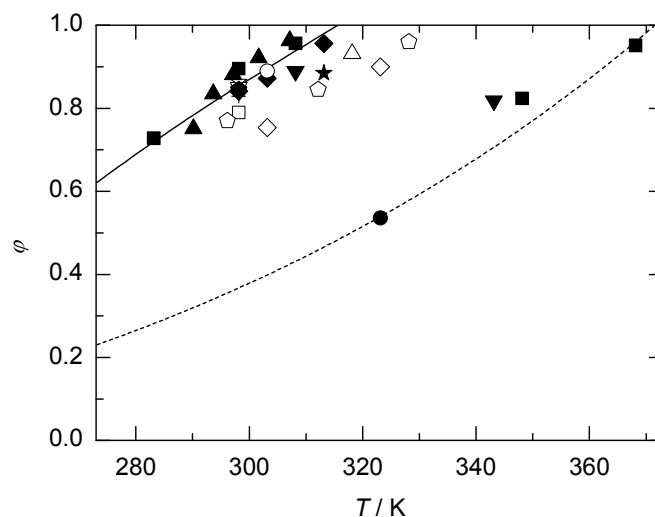


Figure 23: Phase diagram for the system $\text{CaSO}_4\text{-H}_2\text{O}$. The solid and the dashed line represent the gypsum-anhydrite and the metastable gypsum- α -hemihydrate equilibrium, respectively. Symbols represent experimental solubility data in different solutions and have the following notation: *solid triangle*: in NaCl solutions^{[194]¹}; *solid inverted triangle*: in NaCl solutions^{[198]³}; *solid square*: in H_2SO_4 solutions^{[247,258]²} values at 348 K and 368 K⁴; *cross*: in H_2SO_4 and Na_2SO_4 solutions^{[200]¹}; *solid diamond*: in NaCl solutions at 298 K, 303 K and 313 K^{[197]³}; *open square*: in H_3PO_4 solutions^{[193]¹}; *open circle*: in synthetic seawater^{[259]¹}; *solid circle*: in HNO_3 solutions^{[204]²}; *open triangle*: in Na_2SO_4 solutions^{[237]¹}; *open inverted triangle*: in NaCl solutions of different authors evaluated in Charola et al.^[219]; *open diamond*: in NaCl (at 303 K) and NaBrO_3 (at 323 K) solutions^{[191]¹}; *solid star*: in H_3PO_4 solutions Tamperova and Shulgina¹; *open star*: in NaCl solutions^{[238]¹}; *solid pentagon*: in H_3PO_4 solutions Tamperova¹; *open pentagon*: in CaCl_2 solutions^{[256]⁵}.

¹ Water activities taken from Hardie^[200]

² Water activities calculated with the E-AIM Modell I^[260,261,262]

³ Water activities calculated with the E-AIM Modell IV^[260,261,263]

⁴ Water activities calculated with vapor pressure data^[264]

⁵ Water activities calculated with the CaCl_2 equation of Rard et al.^[257]

The results presented in this paper stand in agreement with the authors determining the transition point for the transition temperature of gypsum to insoluble anhydrite between 313 K and 317 K.^[192,194–196,199,211] In the phase diagram of the System $\text{CaSO}_4\text{-H}_2\text{O}$ the points representing phase transitions in mixed systems show some scatter around the calculated curve of the gypsum-anhydrite equilibrium within their center. These deviations will be paid close attention in the following part. In addition to that, the work of Hardie^[200] and the first attempts of modeling the phase equilibria in the present system will be discussed.

The first value of the gypsum-anhydrite phase transition temperature in pure water was mentioned to be at 336 K.^[191] It was determined by two methods, the thermodynamic examination of solubility data and direct vapor pressure measurements of saturated salt solutions containing calcium sulfate. The solubility method, as also used in this work, is a very precise method if the used data is accurate but according to Partridge and White^[192] the data used by Van't Hoff et al.^[191] for anhydrite solubility was misinterpreted. In the discussion of D'Ans et al.^[194] it is also mentioned, that the used material in the vapor pressure measurements was not exactly defined as one of the thermodynamically stable phases and therefore must be considered as a mixture of both stable and metastable phases. This well-founded criticism leaves the value at 336 K very questionable. Partridge and White^[192] tried to determine the gypsum-anhydrite transition temperature from solubility measurements and quote it

to be near 313 K. A more exact determination was not possible back then since the lack of anhydrite solubility data at lower temperatures. From their experiments they also reported an interesting anomaly that gypsum does not directly convert into anhydrite below 371 K but converts rapidly into hemihydrate between 371 K and 373 K. Unfortunately, their experiments were incomplete but indicate that hemihydrate is converted slowly into anhydrite. 9 years later, this behavior was also reported by Posnjak.^[196]

Hill^[195] postulated a transition temperature of 315 K for the gypsum anhydrite equilibrium in aqueous solution. Careful solubility measurements from both the undersaturated and the supersaturated side were performed in his study. It was already mentioned, that both natural and synthetic anhydrite are problematic as they produced volatile results.^[223] Several ways were tried and the most successful proved to be the boiling of gypsum in solutions containing 15% to 20% sulfuric acid for three days. Solutions with 5% of potassium sulfate were also successful but required more time. The results of this preparation study turned out to be very useful as Hill^[195] encountered problems in the measurement of anhydrite solubility below 338 K but at that temperature the measured anhydrite solubility was clearly below that of gypsum, indicating a lower transition temperature. The addition of small, differing amounts of potassium sulfate to the investigated solutions solved this problem.

The values of the gypsum anhydrite phase transition published by D'Ans et al.^[194] left unanswered questions with respect to the differences between the binary $\text{CaSO}_4\text{-H}_2\text{O}$ calculated from his equation and the $\text{CaSO}_4\text{-NaCl-H}_2\text{O}$ system transition points. D'Ans himself quoted, that the curve of the points in NaCl solution showed unexpected behavior, to be clear a convex instead of a concave curve progression. His explanation was a correlation between the rising CaSO_4 solubility in low concentrated NaCl solutions and its influence on the vapor pressure of the given solution but even though the solubility of CaSO_4 is at its maximum about three times higher the resulting effect in the vapor pressure of the solution is still insignificant. A similar behavior can be found in the publication of D'Ans and Höfer^[193] where the solubilities of CaSO_4 had been determined in solutions of H_3PO_4 . That there were uncertainties in this value were reported^[194] but no further explanation followed except that these values needed additional evaluation.

The data published by Bock^[197] shows very good agreement with this work, but the circumstances how he achieved these values is not very well documented. In his experimental description is written, that he used synthetic gypsum from which he produced anhydrite thermally. This usually leads to anhydrite crystals of very fine grain size. A further treatment similar to the one described above is not mentioned. According to D'Ans et al.^[194] these fine grained A(II) crystals tend to have a higher solubility than larger crystals and due to the slow recrystallization achieve supersaturation, the main problem with the measurement of the solubility of anhydrite because the gypsum and anhydrite solubilities are located so close together. Additionally, experimental times of only 48 hours were reported. After that time no more change was observed and equilibrium was assumed. According to Hill^[223], anhydrite can reach states of no reaction over long periods and the addition of sodium chloride leads only to hemihydrate formation.

Zen^[198] tried to determine the transition points in the $\text{CaSO}_4\text{-H}_2\text{O}$ System at temperatures of 308, 323 and 343 K in NaCl solutions similar to Bock^[197]. The previous work of Kelley et al.^[199] is criticized for using inconsistent data and earlier solubility measurements for only measuring from the undersaturated side what is wrong in the case of Hill^[195]. Unfortunately Zen^[198] encountered difficulties in directly measuring the anhydrite solubility so he calculated the solubility by using an extended form of the Debye-Hückel theory. Comparing the derived solubility for anhydrite with the measured data of other authors, it is obvious that the values are too high resulting in a larger NaCl concentration of the intersection point and therefore in a water activity that is too low. The transition point of gypsum to hemihydrate at 343 K was, according to Zen, hard to pin down because of the high amount of NaCl present in the solution that made it hard to identify small amounts of hemihydrate and of the closeness to the NaCl saturation. Therefore Zen^[198] concludes a high uncertainty for this value. The results of the present work predict no transformation of gypsum to hemihydrate in a saturated sodium chloride solution until 347 K.

Solubilities in sulfuric acid solutions publicized by Zdanovskii and Vlasov^[203] as well as Marshall and Jones^[258] showed some awkward results. If the H_2SO_4 concentration is extrapolated to zero, the transition points match more or less with the published results in this paper but the reduction of the transition temperature of gypsum to anhydrite or hemihydrate with rising H_2SO_4 concentration is higher than expected. The solubilities of ^[258] used to determine the transition point were only for gypsum at temperatures of 298 K and 323 K. Their experimental section showed no obvious sources of error and a comparison of the value at 298 K measured in water showed only a deviation of $-0.001 \text{ mol}\cdot\text{kg}^{-1}$. In the experimental description of Zdanovskii and Vlasov^[203], the exact specifications of their starting material, natural or synthetic origin, and the analysis of the solid remaining at the bottom of the solution are not mentioned. Comparing these values measured in water, similar as above, they only show slightly higher values for all isotherms except the one at 368 K. This indicates the usage of fine grained material resulting in higher solubilities but this cannot be the reason for this irregularity because a higher solubility for anhydrite would result in a larger area where gypsum is the thermodynamically stable phase. Here we have the opposite. If the results are compared with the measurements in sulfate containing solutions^[200,237], there is an interesting common ground visible in Figure 23. According to sulfate containing solution measurements there would be no phase transitions below a water activity of 0.6 at any given temperature. This stands in conflict with the results of Beremzhanov and Kruchenko^[249] as well as Kruchenko and Beremzhanov^[204] which are in good agreement with the results of this work. Obvious is the rising difference between the calculated values in pure water and the measured ones with increasing sulfate content in the solution. A reasonable explanation for this behavior in sulfate containing solutions is yet unavailable.

Hardie^[200] reported a transition temperature of the gypsum-anhydrite equilibrium of $331 \pm 2 \text{ K}$ in water. He came to this conclusion through a series of long term experiments, measuring the transition of gypsum to anhydrite and the other way around in various aqueous solutions either containing sulfuric acid or sodium sulfate at different concentrations, saturated limewater or just water. 10 g of solid, consisting of anhydrite, gypsum or mixtures of

both phases were combined with 190 to 240 g of one of the above mentioned solutions and afterwards tempered. For the examination, Hardie^[200] considered only runs where a change of the phase has occurred. The transition temperature was determined by extrapolating a curve based on three measured data points considered to be at the phase equilibrium. From the experimental point of view this approach sounds very logical, but the fact that runs where ignored where no change had occurred is very questionable since Hill^[195] objected, that anhydrite in solution can remain under- or supersaturated for months. On the one hand argumentation was, that there could exist persistent metastable phases, on the other hand, that when a transition is happening the fact was neglected, that metastable phases can crystallize if kinetically benefited. From the experimental runs in water, it is clear that the formation of insoluble anhydrite is kinetically hindered. This phenomena was also mentioned by Charola et al.^[219] Even at the run at 343 K no anhydrite is formed after 359 days from a mixture of gypsum and anhydrite, although it was considered the stable phase under these conditions according to Hardie.^[200] This indicates that in this case, gypsum is a persistent metastable phase with respect to anhydrite. Interesting is to mention, that at 313 K in the water runs anhydrite readily transformed to gypsum, while at higher temperatures, there were no changes at all. Under these higher temperatures gypsum is able to remain as a metastable phase but does not precipitate anymore. This indicates a transition temperature between 313 K and 323 K, what stands in good agreement with this works result and that of other authors.^[192,194-196,198,203-205,208,211] But still the question remains, why Hardies^[200] results show such a large difference to the above mentioned authors. A reasonable answer was suggested by D'Ans^[248], where the problem was pinned to the grain size of the anhydrite crystals used by Hardie.^[200] The effect of using small crystals had been pointed out before by Posnjak^[259] and D'Ans et al.^[194] resulting in a higher amount of solid dissolving what would create a supersaturation. According to D'Ans et al.^[194] the powdered anhydrite needs to be artificially altered by boiling it in diluted hydrochloric acid for at least 14 days up to 3 months. It is also mentioned, that anhydrite produced thermally from gypsum yields unreliable solubilities and suggested a synthesis of anhydrite from gypsum by boiling it in sulfuric acid for about 3 days.^[223] In Figure 21b, it is evident that both the solubilities of gypsum and anhydrite run extremely nigh close to the transition point. A solution supersaturated with respect to anhydrite may easily be supersaturated with respect to gypsum as well and gypsum crystallizes very readily.^[259] As mentioned above this would result in a larger area where gypsum would seem to be the stable phase. By paying close attention to the conditions of every run containing sulfuric acid it is obvious that all transitions of anhydrite to gypsum at temperatures higher than 303 K are located in the area where according to this paper anhydrite is considered to be the stable phase. If sorted with respect to the starting composition of the solid, only mixtures of gypsum and anhydrite at a ratio of 1:1 can be found. Comparable runs containing only anhydrite as starting material remain unchanged. This indicates that the presence of gypsum crystals leads to the formation of gypsum as a persistent metastable phase with respect to anhydrite. The question why gypsum runs manage to transform completely into anhydrite without a recrystallization to gypsum stands, apart from thermodynamic reasons, unanswered.

Additional support for the transition temperature of Hardie^[200] was published by Blount and Dickson.^[201] They supposed a transition at 329 ± 3 K by determination of the intersection of gypsum and anhydrite solubility. Highly questionable is the achievement of the anhydrite data, because it was extrapolated from 343 K downwards. Knacke and Gans^[202] made a different attempt to determine the transition temperature of the gypsum-anhydrite equilibrium. Using the benefited crystallization kinetics of gypsum, they prepared anhydrite solutions at 326 K and 331 K. After several weeks, when it was decided that the conductivity of the given solution has reached the equilibrium, the addition of gypsum should reveal which phase has the lowest solubility at the investigated temperatures. At 326 K the conductivity decreased, what they interpreted as proof, that gypsum is the stable phase. The increase of the conductivity at 331 K lead to the assumption, that the transition temperature can be pointed to 328.65 ± 1.5 K. Freyer and Voigt^[265] criticized, that the saturation of anhydrite is normally achieved after 20 to 30 days, leaving the question why the conductivity in their experiment is still increasing after this period of time. In addition to that, it is never mentioned, if the solid has been investigated after the experiment was finished. If compared with the experiments of Hardie^[200] in pure water, the result is questionable as no change in the water runs between 323 K and 343 K was observed even though both gypsum and anhydrite were present in the solution.

The group of Innorta^[205] tried to determine the transition temperature of gypsum to anhydrite through solubility measurements from both, supersaturated and undersaturated solutions. Even though they achieved similar values for gypsum and anhydrite solubility from both sides, their solubilities are in error. If compared to other solubility data, the measured gypsum solubility must be considered as too low and on the other hand, the anhydrite solubilities were too high. Possible explanations for the divergence can be the short duration of the runs of at most one week in the case of anhydrite until equilibrium is assumed and the usage of synthetic anhydrite attained thermally from gypsum. It is mentioned that anhydrite can reach a state of no reaction over long periods^[223] and argued, that anhydrite dissolution kinetics can lead to equilibration times of at least 20 days.^[194,195] Additionally, the high anhydrite solubility can be explained with very small crystals obtained from the thermic process as it is not mentioned if they were removed from the investigated sample as required.^[194,223] Therefore, the given value of the gypsum-anhydrite equilibrium of 322.5 ± 2.5 K must be considered as too high.

Møller^[208] gives a transition temperature of 322 K. This value was obtained from the calculations of an extended form of the previously published model^[207] enabling the predictions of solubilities to high temperature and concentration. The basis of Møllers calculation is gypsum solubility data that was used in the previous calculations.^[207,266] The data for insoluble anhydrite is calculated from the above mentioned gypsum solubilities together with the water activity data of Hardie.^[200] As the values of Hardie^[200] are in error, the calculated anhydrite solubilities and the resulting transition point are based on wrong input data and must be considered as inaccurate as well. The idea of Raju and Atkinson^[210], the present work is adopting, shows one fundamental mistake in their implementation and therefore the predicted transition temperature of 332.9 K is factually flawed. The fundament of the later used equa-

tion are the Pitzer ion interaction parameters at 298 K from Rogers.^[267] To describe the temperature dependency, parameters established in the equation of Holmes and Mesmer^[268] of the similar 2–2 electrolyte magnesium sulfate were used. In the work of Rogers^[267], the third virial coefficient C^ϕ in the equation for 298 K is neglected. Holmes and Mesmer^[268] on the contrary did use the third virial coefficient C^ϕ for their equation, hence the two sets of parameters are not combinable.

5.4 Conclusion

The approach, to predict the thermodynamic properties of electrolyte solutions with only very limited data available, has been successfully applied on the system of $\text{CaSO}_4\text{-H}_2\text{O}$. The Pitzer ion interaction model in its original form is capable to calculate accurate values for activity coefficients and water activities of aqueous calcium sulfate solutions. The usage of a CaSO_4^0 ion pair was not required for the effective predictions, even at elevated temperatures. Instead, the application of aqueous magnesium sulfate solution properties for the $\text{CaSO}_4(\text{aq})$ parameterization allows the extrapolation of the Pitzer equation to high molalities with a simultaneously good representation of the temperature dependency. The combination with carefully selected solubility data, obtained from the literature, enabled the calculation of thermodynamic solubility products and lead continuative to a prediction of equilibrium conditions between the phases of gypsum, insoluble anhydrite and α -hemihydrate from 273 K to 373 K. These predictions could be successfully reinforced with additional solubility data from mixtures, creating a consistent relationship. For a satisfactory reproduction of β -hemihydrate or soluble anhydrite, the experimental database was insufficient.

The strongly discussed transition temperature of gypsum to insoluble anhydrite in water was pinned to 315 ± 2 K determined from carefully evaluated solubility data. The transition temperature of gypsum to α -hemihydrate assigned to 371 ± 1 K concurs with earlier work. Additional analysis of reported calcium sulfate solubilities in ternary and quaternary systems supported this work's results of both the predicted phase equilibria and transition temperatures.

The equilibrium properties in the system $\text{CaSO}_4\text{-H}_2\text{O}$ would rather speak for a low temperature storage application. Even though the transition of hemihydrate to gypsum up to 371 K is possible, it still happens in an area where gypsum is metastable with respect to insoluble anhydrite. Further investigations are necessary, especially with phase transitions that comprise soluble anhydrite hydration reactions. An application as a chemical heat pump for elevated temperatures is already under investigation with promising results^[269] and the question remains if the material might also be used for household heating. In case of this system, the comprehensive thermodynamic view is not a suitable tool for this evaluation but nonetheless, the gained information answers a highly discussed question and the obtained parameters for the aqueous solution will be useful, e.g. in the field of modeling the properties of complex hydrometallurgical solutions that also contain aqueous CaSO_4 .

6 The measurement of the pressure resistance of mirabilite ($\text{Na}_2\text{SO}_4 \cdot 10\text{H}_2\text{O}$)

6.1 Introduction

In the previous chapters, the phase change behavior of the investigated hydrates was focused on the temperature and water vapor pressure at homogeneous atmospheric pressure. The calculation of the pressure dependency of both the deliquescence humidity and the hydration–dehydration equilibria can be done with the equations for the crystallization and hydration pressure mentioned in chapter 2.4.

In this chapter, the focus is on the development of an apparatus for the actual measurement of the hydration pressure. Previous articles have shown, that the damage of porous materials via the mechanism of hydration, Eq. (2) from right to left, are unlikely to be responsible for the generation of stress.^[17,270] A dissolution–recrystallization process is presumed to be more likely as a damaging mechanism.^[17] This mechanism would cause a crystallization pressure according to the degree of supersaturation in the solution.

In recent years, studies reported about damages to large structures caused by the hydration of calcium sulfate anhydrate (insoluble anhydrite) to its dihydrate (gypsum).^[213,214] In case of^[213], this process took place in a deep stratum resulting in the heave of the massive pillars of a railway bridge with a rate of 5 to 10 mm per month. In both cases, it is also assumed, that the sudden availability of liquid water is responsible for the generation of stress via the above mentioned mechanism. On the other hand, this enormous pressure generated by the crystals to lift the constructions in return also acts on the gypsum crystals; hence the pressure resistance of gypsum crystals must be very high.

In general, a hydrated crystal has a maximum pressure resistance and if that pressure is exceeded, it becomes metastable with respect to another phase. For this study, sodium sulfate was chosen, not because its crystallization is far more damaging than any other salt^[17] but because the system $\text{Na}_2\text{SO}_4\text{--H}_2\text{O}$ is fairly simple. In addition, previous experiments on the measurement of its crystallization pressure were performed but uncompleted.^[271] According to thermodynamic considerations, a crystal of mirabilite ($\text{Na}_2\text{SO}_4 \cdot 10\text{H}_2\text{O}$) can withstand a pressure of 9 MPa at 298 K and $\varphi = 0.858$ before its solubility becomes equal to that of thenardite (Na_2SO_4) and further pressure increase forces dissolution to take place.^[31] In the previous investigation^[271], several attempts were made to measure the generated pressure of mirabilite by exposing thenardite to liquid or gaseous water. The exposure to water vapor would indicate that a measurement of the hydration pressure was done, but unfortunately the actual water vapor pressure was not reported. Nonetheless, the failure of this experiment was mentioned by the formation of a thin hydrated crust that prevented a further passage of water vapor to the anhydrous crystal. To avoid the above reported problems with partial hydration, this work is aiming at the dehydration reaction.

6.2 Experimental Planning and Measurement Setup

Preliminary to the development of a measurement apparatus, the requirements for the measurement of the pressure resistance of a hydrated salt by forcing its dehydration must be evaluated. The crystal has to be in confinement that generates an anisotropic stress. It must allow the crystal to dehydrate and the dehydration products, the dehydrated salt and the released water from the lattice, must not interfere with the ongoing measurement. Access to the vapor phase must be given and the partial water vapor pressure and the temperature have to be kept constant for the equilibration process.

Figure 24a shows the isothermal phase diagram for $\text{Na}_2\text{SO}_4\text{-H}_2\text{O}$ at 298 K with the additional pressure, Δp , on the system versus the relative humidity. The deliquescence humidities, solubility products and ion activity products were calculated with the equations of Steiger and Asmussen.^[272] The influence of pressure on the phase boundaries was calculated with Eqs. (51) and (54) for the crystallization and hydration pressure respectively. Figure 24b pictures the estimated progress during a measurement. Starting at point A, an initial pressure is applied on the crystal. At this point, it is important to mention that the initial pressure is kept constant and the only possibility for the crystal to reduce it is by decreasing its volume. In the phase diagram (cf. Fig. 24a), the range between point A and B is outside the field of existence for the loaded sides of a mirabilite crystal and dissolution will occur. Point B marks the pressure dependent deliquescence humidity of mirabilite or in other words its crystallization pressure at $\varphi = 0.85$. A further decrease of pressure can no longer be accomplished through dissolution. In the range between B and C, mirabilite is metastable with respect to thenardite; hence a solid state dehydration is considered the only way for a further decrease of the crystals volume. Reaching point C that represents the hydration pressure, mirabilite is in equilibrium with thenardite and it is no longer essential to reduce its volume hence the applied pressure stabilizes.

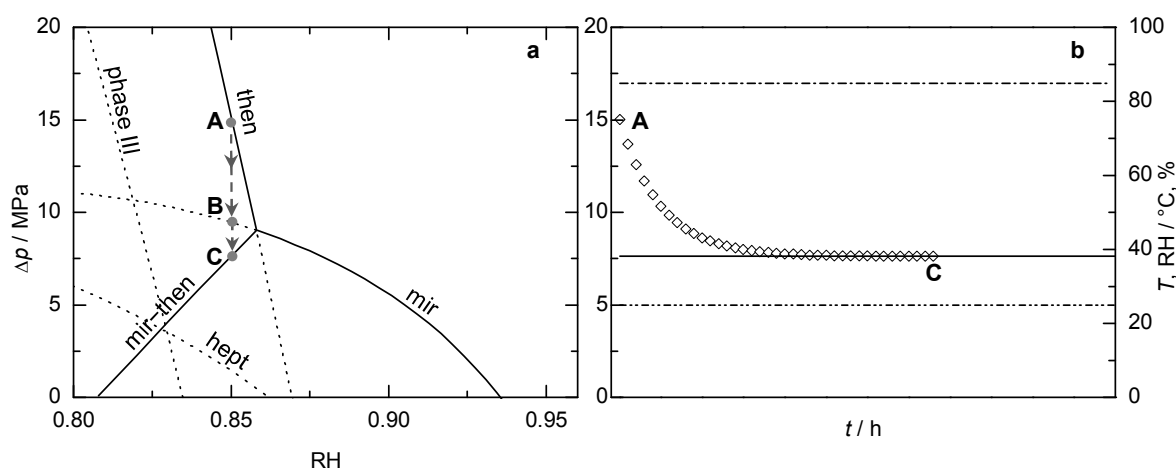


Figure 24: a) Pressure dependent phase boundaries in the system $\text{Na}_2\text{SO}_4\text{-H}_2\text{O}$ at 298 K.^[272] Solid and dotted lines show stable and metastable deliquescence humidities for thenardite (then), mirabilite (mir), phase III (phase III) and heptahydrate (hept) respectively. The hydration–dehydration equilibrium between mirabilite and thenardite is pictured by the solid line (mir–then). The gray points A, B and C and gray arrows represent experimental planning, see text for further explanation. b) Estimated progress during a measurement. Lines show the hydration pressure of mirabilite (solid) at constant temperature (dash–dot–dot) and relative humidity (dash–dot). Open diamonds represent the actual measurement progress.

The developed experimental setup, that is capable of simulating the above mentioned effects of a constant pressure on the crystal that can only change if the crystal changes can be described as a column with a weak point. The further explanation of the setup will be separated in three parts. The central column where the reaction takes place, the fixation of the column that allows the generation of pressure on the central column and the surrounding setup that controls the relative humidity, temperature and air circulation.

The central column is pictured in Figure 25a. The crystal is embedded between two steel plates, 9.9 mm in diameter, to create the needed confinement with a surface area of 0.769 cm^2 . A 1 mm gap between the steel plates and the steel cylinder enables “unwanted” reaction products like solution or water to leave the reaction site, is a diffusion path for the water vapor and allows the crystal to be under anisotropic stress with loaded and unloaded sides. Besides the gap, the steel cylinder has only a stabilizing function for the bottom side of the column. To prevent the contamination of the force sensor (K13 force sensor, Lorenz Messtechnik GmbH) with e.g. saline solution, it is placed on top of the column. The crystal in confinement is connected with the force sensor via the steel piston allowing a direct force transmission between the sensor and reaction site.

The fixation of the column is a crucial matter as the column must be able to move in the y-axis but has to be prevented from moving along the x- and z-axis. In addition it has to encapsulate the column to enable the generation of pressure while giving access for the vapor phase to the crystal surface. A picture of the fixation is given in Figure 25b.

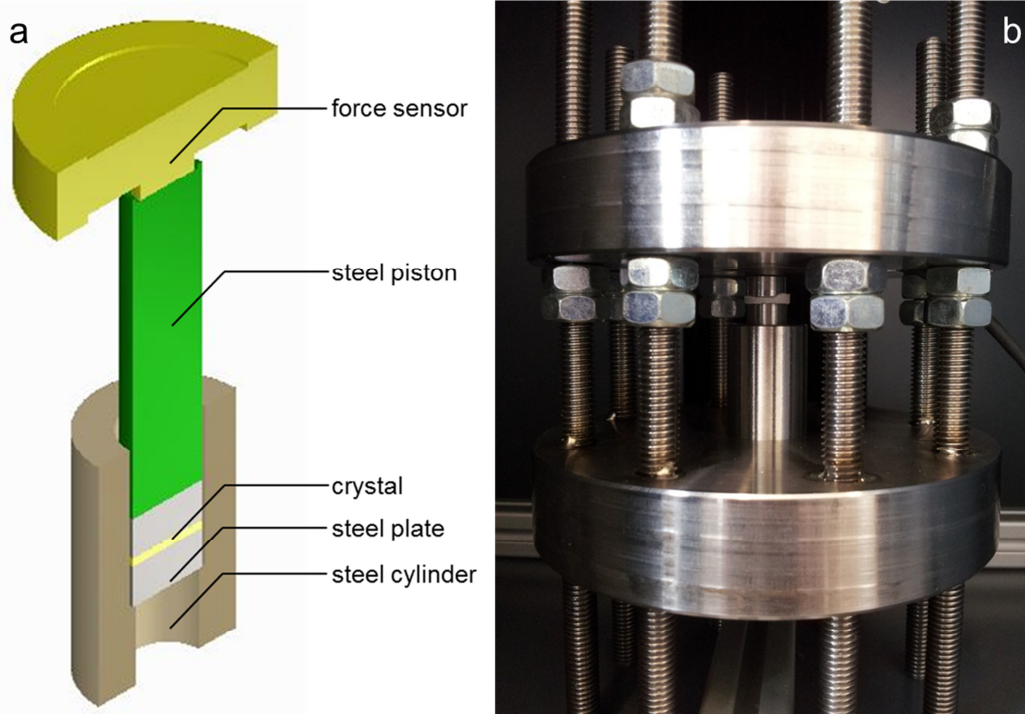


Figure 25: a) schematic display of the general column. b) picture of the general column within the fixation.

In Figure 25b, the central column is embedded between two 3 cm thick steel muff. The two muffs are connected with eight threaded steel bars that are welded to the lower muff. The upper muff has eight corresponding holes that it can be placed on top of the column. Variations in height can be compensated using nuts under the upper muff that are fixed by additional locknuts. The upper muff is prevented from movement along the y-axis with nuts securing it against the lower nuts. In the lower muff, a 1 mm recess with the diameter of the cylinder of the column enables it to hold the column in place. The upper muff has recesses for the force sensor and its cable as well as an additional hole above the force sensor which is threaded.

The surrounding setup is pictured in Figure 26 and consists of a climatic chamber in which the column and fixation (measuring setup) are placed during an ongoing measurement. The chamber is built from PVC (polyvinyl chloride) plates and has multiple access points for sensor equipment as well as for fluid and gas supply. The chamber itself is isolated with isolation foam (Armaflex, Armacell GmbH) and contains a built-in radiator (Rad) with two fans attached to it. The temperature is set using an external thermostat (F32-ME, Julabo GmbH), Th1, that supplies the radiator with a tempered heat transfer medium (Thermal G, Julabo GmbH). The thermostat is controlled and regulated by a directly connected Pt-100 temperature sensor which measures the temperature inside the chamber to get isothermal conditions. The humidity is set by a humidity generating unit consisting of a humidity generator (HG) providing a humid airflow and a thermostat (Th2) to prevent condensation in the supply lines. The humid gas flow (RH) is directed through the lamellae of the radiator to get a fast tempering. The relative humidity of the gas is measured by a humidity sensor (RH/T). Its data is recorded by a data logger (DL1) which is connected to a computer (PC). Here the data is saved and the ratio of a mixture between a dry and wet gas flow is constantly calculated for the humidity generator to achieve a constant relative humidity. The force measured by the force sensor inside the measuring setup is recorded by a different data logger (DL2) and also saved by the computer.

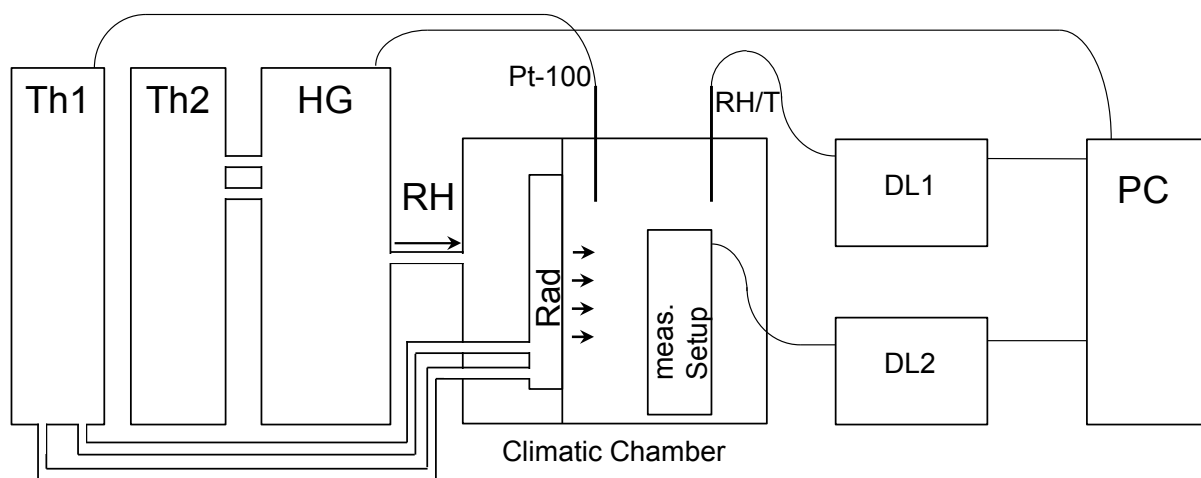


Figure 26: Schematic view of the surrounding setup. For further explanations, see text.

6.3 Experimental Procedure

As mentioned above, sodium sulfate was chosen for this study. The anhydrous sodium sulfate was supplied by the Grüssing GmbH as pure grade material and once recrystallized for further purification. The obtained mirabilite crystals were used for the pressure resistance experiments. To generate an even surface on the investigated crystal, it was prepared as a pellet during a measurement where the steel plates and the cylinder were used as a press to compact a loose filling of either large or carefully ground mirabilite crystals with an average diameter of about 1 mm.

The measurement was prepared by preconditioning the column and the fixation for 24 h in the chamber to eliminate possible temperature gradients in the metal parts and to achieve constant climate conditions. After the initial period, the pressure was applied on the central column to generate a compacted crystal and to start the measurement. For the whole measurement period, the data is digitally recorded for the climate and the measured force separately. In between measurements, adaptations in the experimental setup or procedure were performed to identify possible error sources and their influence on the results. The changes, their advantages and limitations will be mentioned subsequently.

The construction is capable to undergo variations in the measurement setup. One of these is the placement of the crystal in the central column. It can be elevated out of the cylinder for a better exposure to the gaseous phase. With the crystal outside the cylinder it is assumed, that slower diffusion and therefore gradients in the surrounding climate can be eliminated. In addition, the transportation of dehydration products away from the loaded side of the crystal should be faster and therefore fasten the equilibration process. The downside of this method is that only pretreated crystals can be used, e.g. previously used and already compacted crystals.

Another variation is the generation of pressure on the crystal. Two different ways are possible. One is to tighten a threaded rod that is connected to the threaded center hole in the upper muff, pushing the force sensor on the remaining central column. This enables the pressure to be applied without the climatic chamber to be opened as the threaded rod is accessible from outside the chamber. The downside is that the generated pressure weighs on only one thread increasing the risk of declamping. The other way is by tightening the nuts on top of the upper muff. This way, the whole muff is pressed on the central column reducing the possibility of a declamping in the pressure generating thread(s) as it is carried by eight threads instead of one. The disadvantage is the need of opening the climate chamber and interrupting the constant climate to start the measurement. In addition, repetitive measurements suffer the same limitations.

6.4 Results and Discussion

In the following presentation of the results, the measurements are first summarized in series that had the same climate conditions. After these series, various changes in the measurements setup and procedure were investigated, see Chapter 6.3, and their influence on the results will be summarized. The theoretical pressure, mirabilite can resist before dehydration occurs, was

calculated for each climate setting using the equations for $\text{Na}_2\text{SO}_4\text{-H}_2\text{O}^{[272]}$ and Eq. (54). Note that the measured values are shown as lines instead of points in the following figures for clearness, as they are recorded with 1 value per minute.

6.4.1 Series 1 at 298.95 K and 85% RH

The results of the first series are shown in Figure 27–Figure 29. The theoretical value for the pressure threshold of mirabilite at these climatic conditions was calculated to 6.5 MPa or 497 N at the above mentioned area of 0.769 cm^2 . Note, that during all measurements in series 1, the same compacted crystal has been used. In a general observation, it can be seen that all measurements show that the applied pressure drops below the theoretical value. In addition, the state of equilibrium is not reached.

For the preparation of the compressed crystal, mirabilite crystals were filled in the cylinder and compacted. This process is pictured in Figure 27a. While the compression took place, the chamber was conditioned to the desired climatic conditions of 298.98 K and 85% RH. Figure 27b shows the progress of the first measurement. The initial force of 1050 N quickly dropped below the threshold at 497 N after only 6 hours. It was assumed that solution was formed in the setup at the high pressure loads as the crystallization pressure of mirabilite is 8.62 MPa or 663 N at the given conditions.^[272] Subsequently the pressure was increased again but also dropped below the threshold after only a few hours. The quick decrease of the measured force below the threshold needed explanation and an inspection revealed that excess solution was inside the setup. It appears that inside the cylinder, the diffusion rate was too slow, hence the transportation away from the crystal failed. The result was a slow crystallization at the inner wall of the cylinder due to the released solution at the loaded surfaces of the crystal. This induced a creeping of crystalline sodium sulfate out of the cylinder. Nonetheless, the compressed crystal could be used for further experiments and was put back in the setup after it was dried at ambient conditions.

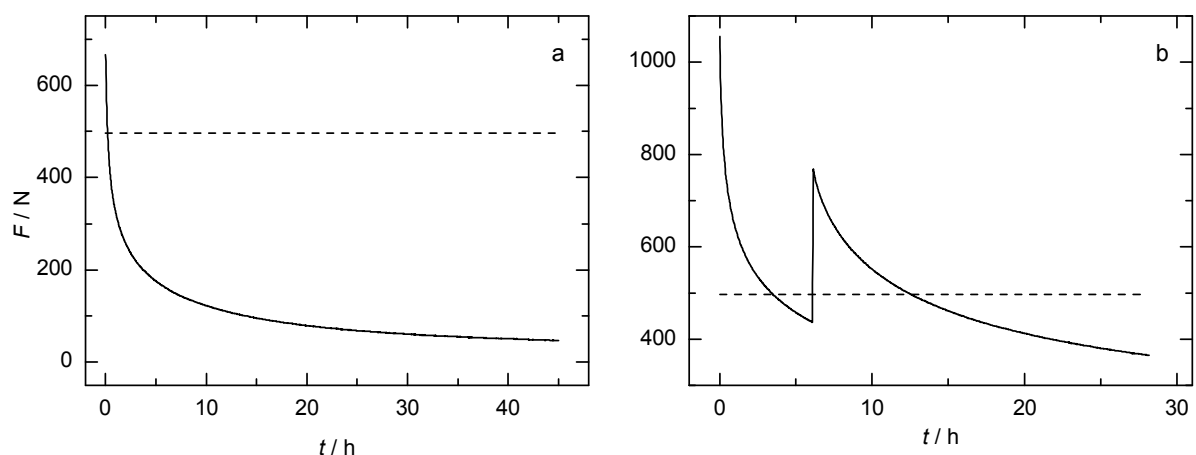


Figure 27: The solid line represents the measurements progress while the dashed line shows the theoretical maximum pressure resistance of mirabilite at 298.95 K and 85% RH.^[272]

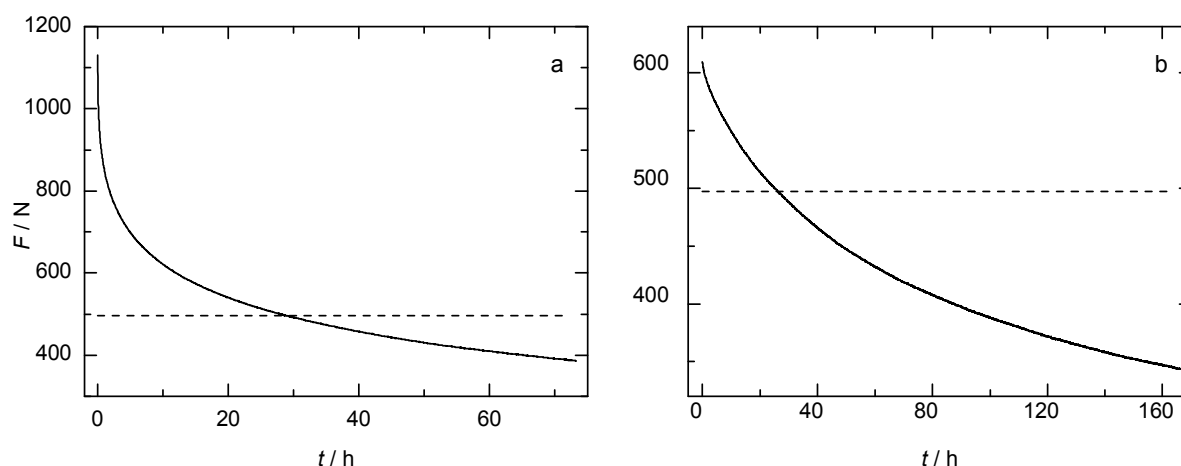


Figure 28: The solid line represents the measurements progress while the dashed line shows the theoretical maximum pressure resistance of mirabilite at 298.95 K and 85% RH.^[272]

Further investigation, if the deliquescence of the crystal could be held responsible for the quick decrease in measured force, was done during the measurements shown in Figure 28a and b. Both measurements show an almost similar time before the threshold is crossed, even though the first investigation started above the crystallization pressure, what should lead to the formation of solution and the second was started underneath the expected pressure at which deliquescence of mirabilite occurs. This indicates that the formation of solution during a measurement by deliquescence does not have a diminishable effect on its progress and the excess solution was carried inside the setup by the initially used crystals which were covered with a thin film of the saturated solution they were stored in.

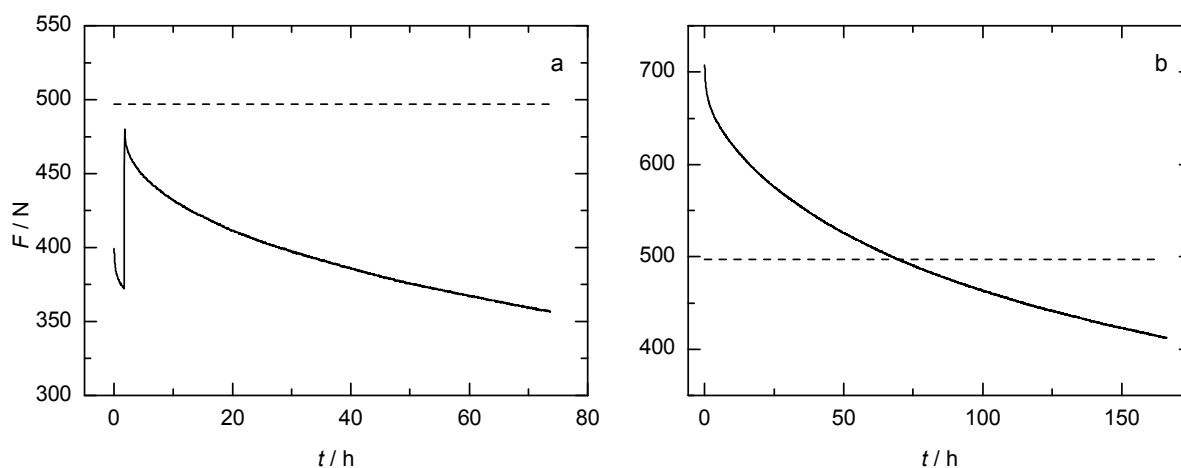


Figure 29: The solid line represents the measurements progress while the dashed line shows the theoretical maximum pressure resistance of mirabilite at 298.95 K and 85% RH.^[272]

Unexplained remains the fact that the applied force always drops below the expected threshold and that also during the long period of over 160 hours in Figure 28b no equilibration process is indicated. This might imply that initially not thought of reactions take place in ongoing measurements. The following measurements in Figures 29a and b show an investigation if the ongoing decrease in pressure below the threshold can somehow be reproduced. The initial pressure drop in Figure 29a is probably a relaxing in the thread after the tightening. The

slope decrease of both measurements was investigated by determining the slopes of Figures 29a and b over the last 16 hours with a linear regression. The result was that the secondary reactions have a repetitive shape with the slopes of the curves in Figures 29a and b determined to $-0.013 \text{ N min}^{-1}$ and $-0.014 \text{ N min}^{-1}$ respectively but a procedure to transfer it between measurements could not be found.

To estimate the influence of the setup and the magnitude of the drift in the force sensor, a measurement without a crystal was performed. The result is shown in Figure 30. A declamping action in the thread at the beginning of the measurement can be observed as in the previous measurements, though its effect is much smaller. In general the decrease in pressure over the whole measurement period is much smaller than in a measurement with a crystal but the ongoing decrease in the above mentioned measurements below the threshold cannot be solely explained with the results of this measurement as the slope is $-0.0003 \text{ N min}^{-1}$ over the last 16 hours.

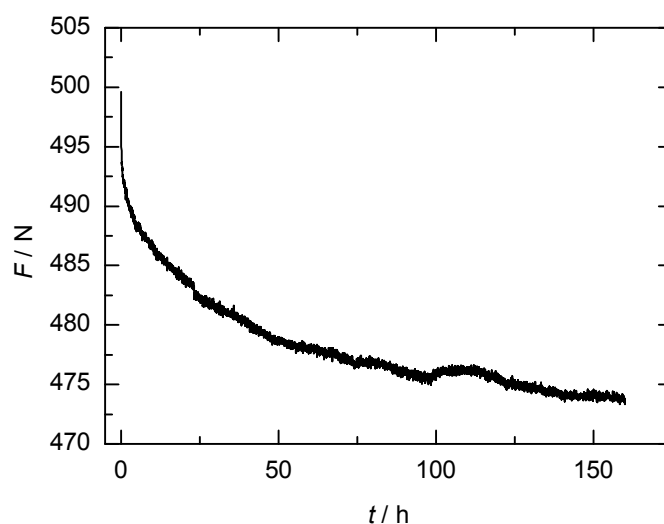


Figure 30: Measurement of the setup without a crystal at 298.8 K and 85% RH.

6.4.2 Series 2 at 298.95 K and 84% RH

The general idea behind series 2 was to decrease the pressure threshold of mirabilite to a lower value to investigate if the secondary reactions are dependent of the applied pressure. As shown in Figure 24a and Eq. (54), the pressure dependent hydration–dehydration equilibrium between mirabilite and thenardite decreases in pressure with decreasing relative humidity. The change to 84% RH results in a change of the pressure threshold to 4.67 MPa or 359 N at 0.769 cm^2 .

A new compacted crystal was prepared from mirabilite crystals that had their excess solution removed while the setup was conditioned to 298.98 K and 84% RH for 24 hours. The results are shown in Figure 31a. An irregularity in the curve progression after 3 hours was assumed an artifact as none of the following measurements could reproduce that effect. Figure 31b shows a repetitive measurement with the same conditions as the previous investigation but with a newly compacted crystal. With slopes during the last 120 minutes of $-0.014 \text{ N min}^{-1}$ and $-0.013 \text{ N min}^{-1}$, both results are similar.

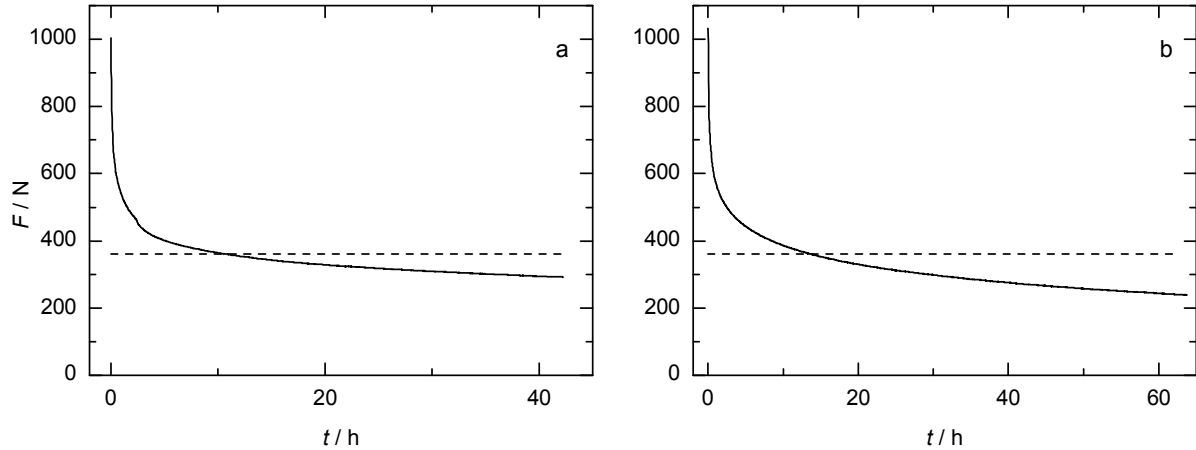


Figure 31: The solid line represents the measurements progress while the dashed line shows the theoretical maximum pressure resistance of mirabilite at 298.95 K and 84% RH.^[272]

Figure 32a shows the repetition of the measurement of Figure 31b with newly applied pressure and no interruption of the climate in between the two measurements. In this case, the curve progression is also similar to the previous investigations but during the measurement, the relative humidity dropped below 10% shortly after the start and was corrected after 7 hours. For an unknown reason, there was no recognizable effect on the measured quantity but the measurement was repeated. Its results are shown in Figure 32b. The curve progression is again similar but although it seems that an equilibrium state was reached at the end, the slope in the last 120 minutes was still negative with $-0.011 \text{ N min}^{-1}$. The progression of the measurement without a crystal is $-0.0005 \text{ N min}^{-1}$ over its last 120 minutes enforcing the assumption that secondary reactions are taking place.

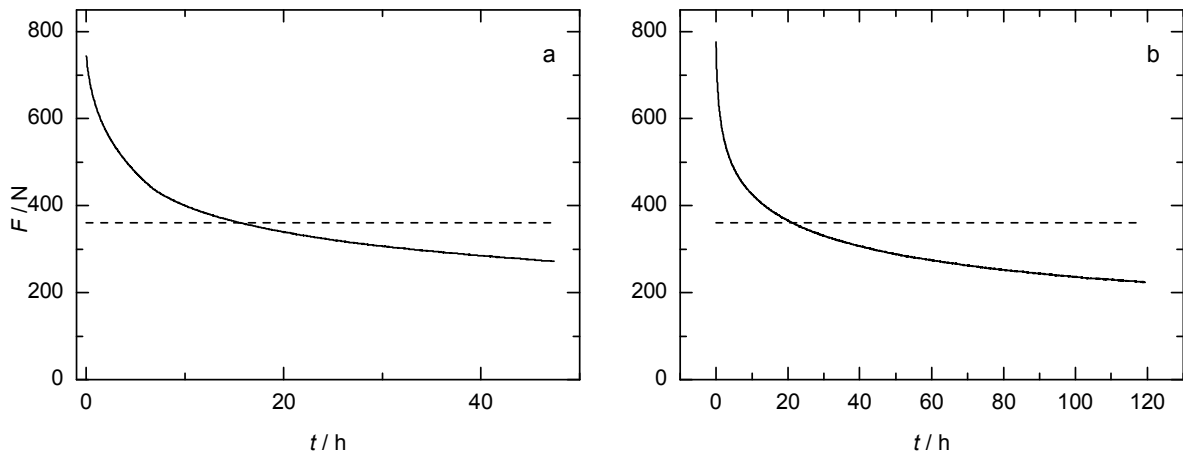


Figure 32: The solid line represents the measurements progress while the dashed line shows the theoretical maximum pressure resistance of mirabilite at 298.95 K and 84% RH.^[272]

6.4.3 Influences on the Measurements

As mentioned in Chapter 6.3 the alternative way to apply pressure on the column was investigated. Here the pressure is not generated with the central thread; instead the nuts that hold the upper muff in place are used to press the muff with the embedded force sensor on the stamp

of the column. In a first attempt, an investigation without a crystal was performed. Its results are shown in Figure 33.

The progression of the curve shows, that a linear decrease in the measured force is recognizable after a few hours. The separation of the load on multiple threads appears to enable the setup to apply a more constant pressure on the column even though the slope in the last 120 minutes with $-0.008 \text{ N min}^{-1}$ is much smaller than in the measurements shown in Figure 30. This might be because of the short duration of the measurement. In addition, note that the applied force is about factor two higher than the expected pressure resistance of mirabilite crystals in the previous measurement series. In a following investigation, the effect of the alternative pressure generation will be studied. In that investigation an additional change has been applied to the setup. Here, a previously compacted crystal that does not need further support at its sides is placed in the setup. The difference is that it is placed outside the cylinder for a better contact to the gaseous phase. This change was easily done by reversing the stamp and the steel plates. The results are shown in Figure 34a and its repetition in Figure 34b. To maintain comparability to the previous measurement series, the climatic conditions were set to 298.5 K and 84% RH.

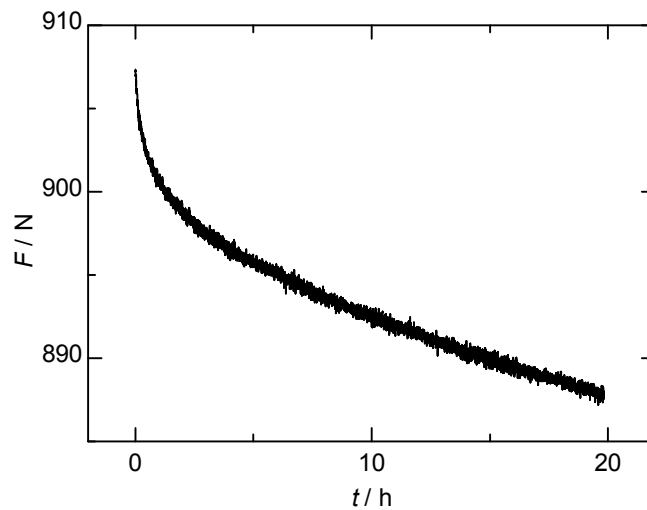


Figure 33: Measurement using an alternative way to generate pressure on the column without a crystal in the setup. The solid line represents the measurements progress.

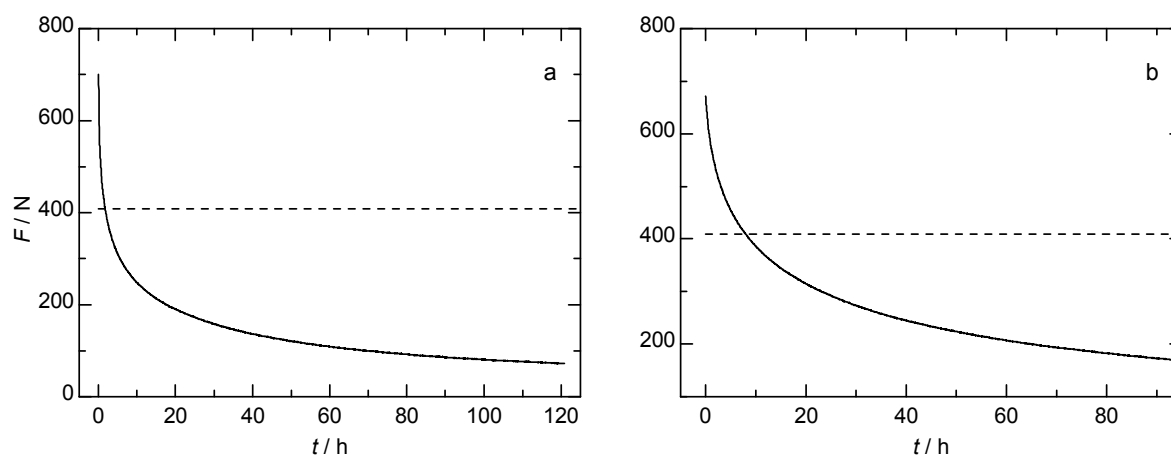


Figure 34: The solid line represents the measurements progress while the dashed line shows the theoretical maximum pressure resistance of mirabilite at 298.5 K and 84% RH.^[272]

Besides the fact that the pressure threshold of 5.3 MPa or 409 N is passed as in the previous measurements, even at very low pressures and long measurement periods no equilibrium state is reached. In addition, the measured force at the end of these two measurements is lower and the pressure loss is faster when compared with the measurements of series 2. While here the threshold is passed under 10 hours, the previous measurements showed longer periods between 10 and 20 hours, even though the crystal in these measurements was already compacted.

To investigate, if the preparation of the compacted crystal is responsible for the continuous decrease below the theoretical threshold, a crystal piece from a large mirabilite needle has been prepared by making two cross sections using a milling cutter to get even surfaces. The Crystal with a height of about 1.5 mm was placed outside the cylinder and the pressure was applied using the central thread as in series 1 and 2. This step was necessary, because the generation of pressure using the upper muff was too insensitive. Area of the prepared crystal was measured 0.18 cm². The calculated threshold at 298.35 K and 84% RH is 5.6 MPa or 101 N at the given surface area.

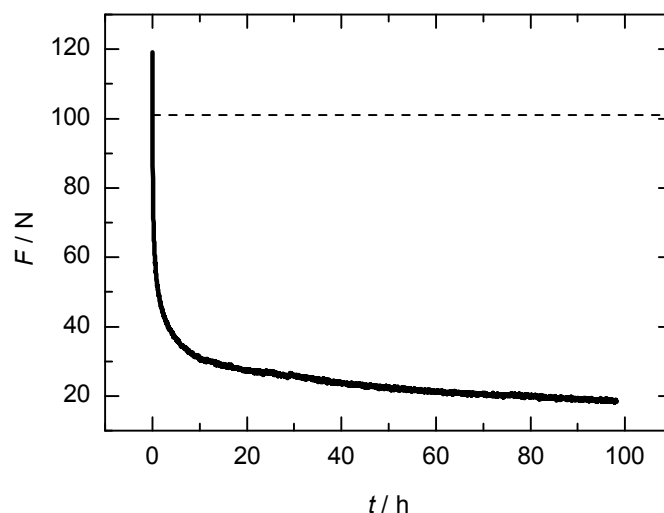


Figure 35: Measurement of the pressure resistance of a mirabilite crystal prepared from a single mirabilite needle with a milling cutter at 298.35 K and 84% RH. Measured values are shown as solid line while the dashed line gives the theoretical pressure threshold at the given climate and measured area of the crystal.

At the beginning of the measurement, the applied force with about 120 N is higher than the theoretical resistance of the crystal. Directly after the beginning, the applied force quickly dropped below the threshold. At about 30 N the slope turns in the characteristically slow decrease observed in all previous measurements. Repetitive measurements with the initial pressure set below the threshold showed results with a similar quick drop and the slope turning between 25 N and 35 N. With a calculated pressure between 1.4 MPa and 1.9 MPa, the pressure that would be generated by mirabilite crystals on porous materials would be low enough that typical building materials with a tensile strength below 3–5 MPa^[272] would most likely be able to withstand them. This is clearly not the case as sodium sulfate is used in standard crystallization tests as of its destructive capabilities.

If the measurements without a crystal are compared with those containing sodium sulfate in the column, the question arises why the force drops much quicker and further in the latter investigations. The desired dehydration reaction but also the previously mentioned side reactions could be named for an answer.

The dehydration reaction correlates with a decrease in volume, simply because the molar volume of thenardite is about a quarter of the molar volume of mirabilite. While the dehydration continues and the height of the column decreases as intended the relaxation in the column might also lead to a declamping in the thread that generates the pressure. The loosening of the thread would result in the observed pressure loss and can also explain why the applied force always drops below the threshold while no equilibration occurs. In the measurements with a crystal, it was observed, that the decrease in measured force does not follow a linear pattern as in Figure 33 but with a continuously decreasing negative slope. With an ongoing pressure loss, the pushing motion against the thread gets weaker and the slope after 20 hours is $-0.004 \text{ N min}^{-1}$, correlating to the creeping motion of the sensor.

Side reactions in the crystal itself can as well be held responsible for the continuous pressure drop. When crystals are exposed to pressure they can sustain deformation, e.g. an elonga-

tion.^[273] In addition, the Schottky effect, an entropic effect that favors voids in the crystal lattice and Fick's law, saying that diffusion in the lattice takes place until the voids are evenly spread throughout the crystal say that there will be motion in the crystal. These effects will most likely continue to take place even when the applied force goes below the pressure resistance mirabilite. In the following experiment, the deformation of crystals under pressure was investigated. As mirabilite is unsuitable for an examination of its surface in a SEM because of the vacuum, sodium chloride was used instead. Another advantage of the use of sodium chloride is that at the investigated temperature no other phases exist. As it is more sensitive, the pressure was generated using the threaded center hole. The progress of the experiment is shown in Figure 36.

The applied pressure at the beginning was about 21 MPa or 640 N on 0.3 cm^2 . At the climatic conditions of 298.35 K and 50% RH, the crystallization pressure of sodium chloride is calculated to 235 MPa hence no deliquescence is expected. The measurement progress is again very similar to the previous investigations. As dehydration cannot and deliquescence will not occur at these conditions, a decrease in the crystals volume can be assumed to happen only through side reactions and/or a declamping in the setups thread. The slope in the last 120 minutes is $-0.003 \text{ N min}^{-1}$ but even it seems to be lower than in the "slope" of the setup itself, note that the duration of this measurement is 14 times longer. After 40 hours in the measurement, the slope is still $-0.010 \text{ N min}^{-1}$. The SEM pictures are shown in Figure 37.

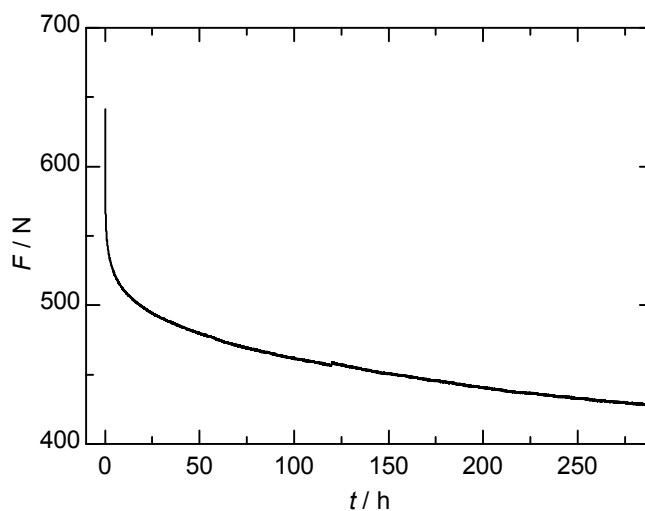


Figure 36: Pressurization of sodium chloride at 298.35 K and 50% RH.

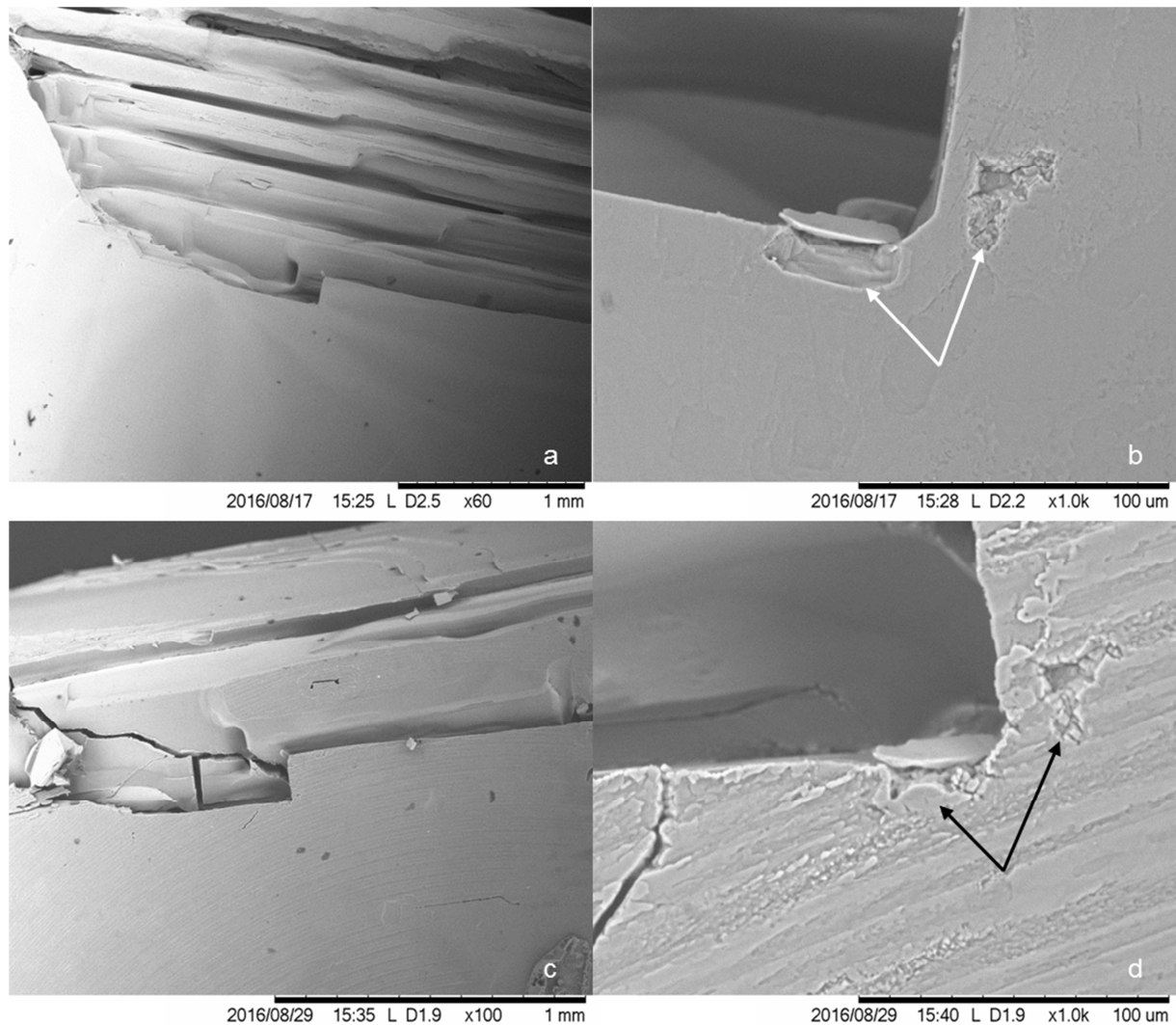


Figure 37: SEM pictures showing a detail of the surface of a sodium chloride crystal. The pictures a and b were taken before and the pictures c and d were taken after the pressure was applied.

The Figures 37a and b show a spot on the sodium chloride crystal as an overview and detailed image respectively in premeasurement condition. From the overview, a smooth surface is noticeable but most important is the visible depth profile. It shows that the crystal itself is not entirely solid as during its growth, caverns have been formed. In the detailed image, two defects are highlighted by white arrows and a straight edge is visible. The Figures 37c and d show the same spots on the crystal after a measurement period of 12 days (cf. Fig. 36). In the overview, cracks in the depth of the crystal are clearly visible but in addition, the previously even surface now shows a cyclic pattern similar to growth rings in a tree. The detailed image gives a better visualization of the cyclic pattern and shows a permanently changed surface. The highlighted two defects also show significant changes in their shape that lead to the assumption that the crystal height has dropped by parts of the crystal being pressed from the loaded side towards the unloaded spots in the defects and the edges that are clearly rougher than before the measurement.

A similar phenomenon has been observed in an investigation regarding the influence of RH on the surface of a sodium chloride crystal mentioned in the review of Ewing.^[274] It was

found, that already a 20% RH a rounding of the sharp corners of the crystal took place. At 42% RH, increased movement on the crystals surface was noticed that created an uneven surface. In an additional investigation of the electrical conductivity as a function of RH, it was found that between 40% and 50% RH an increase in the conductivity was measured and explained by solvated ions in the thin water layer. These experiments show that even at climatic conditions below the deliquescence humidity of sodium chloride the available water can interact and alter the surfaces of NaCl crystals. In subsequent studies using atomic force microscopy the changes in the crystals surface could be quantified as a function of RH creating steps on the surface.^[275]

These experiments give a reasonable explanation for a mechanism that allows the changes in the crystal surface that happen below its deliquescence humidity and show similarities with the experiment shown in Figure 37. The ongoing decrease in pressure can be explained as follows. From the previously mentioned experiments, it was shown that at 50% RH a thin water layer is present on the crystals surface. The formation of steps would follow but in this works experiment, the investigated sides were loaded and therefore the creation of steps should be unfavorable as the resulting pressure is very high in correlation to the very small surfaces. Nonetheless, ions will enter the water layer but as they cannot rejoin the crystal lattice while it is loaded, diffusion will take them to unloaded places like defects or the edges as visualized in Figure 37d. This process will result in a degradation of the crystals height and therefore lead to an ongoing pressure loss during the measurement.

6.5 Conclusion

An experimental setup was developed that is capable of generating anisotropic stress on a solid material, such as a crystal, at constant climatic conditions. In this study, the investigated mechanism was the way of dehydration from mirabilite to thenardite in the fairly simple system of $\text{Na}_2\text{SO}_4\text{-H}_2\text{O}$. That way, previously encountered problems with partial hydration or clumping of the salt could be prevented. Additionally, it is possible to use solid, nonporous material for the crystals confinement as the driving force of the dehydration reaction is the applied pressure. The relative humidity just acts as a regulator as the water vapor is expected to be in an equilibrium process with the loaded sides of the crystal in its confinement. From the first experiments, it can be concluded that the availability of excess liquid water drastically reduces the applicable pressure. The crystals loaded surface has an increased solubility in contrast to the unloaded surface and this gradient is expected to be the driving force for a shifting in the crystals shape. The availability of excess water can be reduced but not entirely eliminated due to physico-chemical principles. On one hand, there is always water released through the forced dehydration process of mirabilite. On the other hand, the high relative humidity that is required for the investigated reaction produces a thin adsorbed water layer on the crystals surface, even when it is not in confinement. A tendency, if a pressure induced deliquescence and the accompanying solution leads to a faster shape shift of the crystal then the dehydration reaction could not be observed. During all measurements, a continuous decrease in applied pressure was observed but it was not possible to clearly isolate the sources for a successful investigation. It could be shown, that the optimal way to generate the pressure

in this setup was the usage of multiple nuts. The partitioning of the pressure to several threads leads to an almost linear decrease that is within the creeping of the force sensor but the investigation of the slope revealed that this effect cannot solely explain the continuous pressure loss below the threshold of the mirabilite crystals. As the measurements regarding the influence of the crystals grew direction were very similar then those with a compacted crystal, it is assumed that side reactions take place. It could be shown, that in this case these reactions are pressure related. The surface of an investigated sodium chloride crystal showed irreversible changes after pressure was applied at 50% RH even though the present conditions prevented deliquescence and dehydration is not possible.

The results of this study, even though the state of equilibrium was never reached, have given new insight in the behavior of crystals that are under anisotropic stress at high relative humidities. If liquid water is present, the anisotropic stress will deform the crystal as the loaded sides are unfavorable and the water acts as a diffusion bridge for a quick ion transfer. In this study, this rate of diffusion could be reduced but not eliminated as adsorbed water on the crystals surface cannot be prevented at high relative humidities, hence the system $\text{Na}_2\text{SO}_4\text{-H}_2\text{O}$ appears to be unsuited for an investigation of pressure induce dehydration. A possible candidate for a further investigation would be the system $\text{CuSO}_4\text{-H}_2\text{O}$. Although it is not known as a damaging salt in constructions, its thermodynamic properties look very promising. The dehydration reactions at ambient temperatures take place at very low relative humidities and the dehydration related volume loss is rather small if compared to mirabilite. At the low relative humidities, the film of adsorbed water can be expected as too thin for an effective ion transport and in addition, the released water from its dehydration reaction will evaporate much faster. These preconditions should retard the reshaping of the crystal during the measurement. The gain from the reduced volume loss is expected to have less influence on a possible declamping action in the setup that would also decelerate the measured pressure loss. The setup of choice for such a measurement would be the placement of a compacted crystal outside the cylinder and the generation of pressure using multiple nuts. The possible humidities at 298.15 K for the measurement of the $5\text{H}_2\text{O}\text{-}3\text{H}_2\text{O}$ hydration pressure with the setup from this study would be between 32.5–34.5% RH ($\Delta p_{\text{hydr}} = 0.5\text{--}9.5$ MPa) calculated with this works results from chapter 4.4.3.

7 Conclusion

The understanding of the phase change behavior of salt hydrates over a wide temperature range is crucial for an examination of its potential as an energy storage material candidate. The more detailed the knowledge about the phase changes in both stable and metastable states of the respective hydrate, the better the capability for this evaluation. In this study, the focus was on the characterization of the thermodynamic equilibria between the phases of three different binary systems with a sulfate anion in common; $\text{CaSO}_4\text{-H}_2\text{O}$, $\text{CuSO}_4\text{-H}_2\text{O}$ and $\text{ZnSO}_4\text{-H}_2\text{O}$.

The creation of the φ vs. T phase diagrams is shown in two different approaches. In case of $\text{ZnSO}_4\text{-H}_2\text{O}$ (chapter 3) and $\text{CuSO}_4\text{-H}_2\text{O}$ (chapter 4), a rich literature data base was available for phase equilibria and the solution properties had only small need of supplementation. After the evaluation of the data for the salts aqueous solutions, the pitzer ion interaction approach provided the needed information about the solutions activities and activity coefficients of the solute to combine the available equilibrium data. The procedure allowed the establishment of a comprehensive phase diagram where both solubility data and dissociation humidities are matched in an internally consistent relation.

In case of $\text{CaSO}_4\text{-H}_2\text{O}$ (chapter 5), the database available was insufficient for the above mentioned approach. Instead, similarities between the bivalent sulfates CaSO_4 and MgSO_4 could be used for the characterization of its solution properties. Missing hydrate equilibrium data could be compensated due to the large solubility database. The calculated phase boundaries were supplemented with phase transitions solubilities of CaSO_4 phases in solutions containing one additional salt.

In the literature, usually large amounts of data are available for various salt systems. In most cases, the available data is sufficient, regarding the key question which materials are candidates for an energy storage application for household heating. The area of interest for most systems is supplemented with experimental data, hence only interpolation is required for an estimation of the phase boundaries.

The three systems investigated closely in this study showed large variations in their hydration–dehydration and deliquescence behavior.

- i. The CaSO_4 phases have no relevant deliquescence humidity, hence the dissolution–recrystallization mechanism is not usable for the energy storage application. The possible insoluble anhydrite formation makes the pursued hemihydrate–gypsum hydration risky as stepwise insoluble anhydrite formation during cycling can occur. The question remains at which conditions the phases can run through many cycles without the inhibiting phase transition to the insoluble anhydrite.
- ii. The System $\text{ZnSO}_4\text{-H}_2\text{O}$ had the advantage of less metastable phases in the desired reaction area than $\text{MgSO}_4\text{-H}_2\text{O}$ but even though both phase diagrams look very similar, the transition temperature of its hexahydrate to the monohydrate is too low. This disqualifies $\text{ZnSO}_4\text{-H}_2\text{O}$ for a use in an energy storage for household heating but the

detailed information on the system open room for further investigations towards applications at lower temperatures.

- iii. Of the investigated candidates, the system $\text{CuSO}_4\text{-H}_2\text{O}$ has shown the best equilibrium properties as its pentahydrate–trihydrate equilibrium is at unusually low relative humidities for sulfates. In addition, the difference between the deliquescence humidities of the mono- to the tri- and pentahydrate is considerable high. This leaves much space in the pentahydrates stability field, offering a large variability for operation parameters in a storage unit.

The measurement of hydration pressures revealed much information about the behavior of crystals that are exposed to anisotropic stress. Side reactions, that prevented the system to enter the equilibrium state, were observed. The measurements series indicate, that the system $\text{Na}_2\text{SO}_4\text{-H}_2\text{O}$ was not suited for this investigation as the required relative humidities were simply too high.

This work has shown different approaches to determine phase boundaries of a salt system in a comprehensive way. It is concluded, that two of the three investigated systems have the potential for a household heating application. In addition, the basic information for the operating parameters and their optimization towards better reaction kinetics without side reactions in the storage unit is provided.

8 Abstract

Recently, politics dictated a change in energy production, away from carbon based fossil fuels and nuclear power towards renewable based energy generation. In the sector of household heating in the FRG, a massive potential exists for the application of renewable heat production. With the right storing technologies to transfer heat from times of excess supply to times of high demand, up to 1.9 EJ could be transferred to the renewables sector. This energy amount equates about 14.3% of the primary energy production in the FRG. Besides that, large amounts of CO₂ emissions could be prevented and next to the economic benefit of saving large quantities of conventional energy sources the independence from foreign imports will be increased.

The most pressing matter with the switch towards the renewable energy sector is its unreliability in case of a predictable production. In addition, not only on a seasonal but also on a daily basis, the energy supply of renewables seldom overlaps with the consumers demand for it. To answer these problems, both long-term and short-term energy storage technologies are required. This work will focus on the characterization of materials to evaluate their potential to be used as storage material for thermochemical energy storage. Next to the other two reversible technologies available for heat storage, sensible and latent, the thermochemical application shows the highest storage density, a property that will have great influence when storage units reach the state of commercial availability.

The use of salt hydrates for a thermochemical energy storage application is under investigation for some decades now, but recent studies often define very strict reaction conditions to measure a very large quantity of potential materials. This thesis focusses on few materials that are characterized in detail to allow not only the energy storage research area to profit from its results but also other fields like hydrometallurgy or even in some parts the sector of construction chemistry and the conservation of cultural heritage.

The general equations for the relations between the thermodynamic fundamentals of electrolyte solutions and the correction terms for their real behavior are given in chapter 2. This chapter also comprises the required equations of the used pitzer ion interaction approach that is used to calculate the activity coefficients of the solute and water activities of the electrolyte solution. In addition, a quick introduction about the required quantities for a parameterization of the electrolyte solution properties is given. The phase diagrams, used to display the areas of stability of each phase are introduced. Examples about the phase changes with varying conditions are given and the influence of pressure on the crystals growth is presented.

Chapter 3 to 5 represent the key results of this theses by presenting the detailed work about the characterization of the three investigated salt systems, ZnSO₄-H₂O, CuSO₄-H₂O and CaSO₄-H₂O in the mean temperature range from 273 K to 373 K.

Both chapters 3 and 4 show an approach, where a rich database in the literature existed. Solution properties and thermochemical data have been critically evaluated and supplemented with additional isopiestic data in case of ZnSO₄(aq) and heat capacity data for aqueous CuSO₄

solutions. The isopiestic measurements were performed in a fully automated water vapor sorption analyzer that allowed many simultaneous measurements at the same time. With the ability to calculate activity coefficients and water activities of the respective electrolyte solutions, solubility products of the different phases could be calculated from solubility data. These results were then supplemented with values from determined from hydration–dehydration equilibria. This allowed the creation of internally consistent phase diagrams that cover both stable and metastable phase boundaries in the investigated temperature range. In case for a household heating application, the entire range is covered with experimental data. In the outer temperature ranges, some cases require extrapolations that leave a small uncertainty with the predicted values.

Chapter 5 deals with $\text{CaSO}_4\text{--H}_2\text{O}$, a system where almost no thermodynamic data exists. In a different approach, values at 298.15 K were combined with the existing parameters of a similar salt, $\text{MgSO}_4\text{--H}_2\text{O}$, which allowed the definition of its temperature dependency. The rich solubility database was evaluated and the phase boundaries for gypsum, insoluble anhydrite and α -hemihydrate were derived. These calculations were supplemented with changes between the above mentioned phases from isothermal solubility data in solutions containing a single additional salt or acid. That way, values for hydration–dehydration equilibria could be included, while their direct measurements always lead to very contradictory results. In addition, the highly discussed transition temperature between gypsum and insoluble anhydrite could be pinned to 315 ± 2 K.

The influence of pressure on hydrated crystals is studied experimentally in chapter 6. A new approach on measuring the absolute pressure resistance of hydrate crystals on the example of the system $\text{Na}_2\text{SO}_4\text{--H}_2\text{O}$ is investigated. During the measurement series, the state of equilibrium was never achieved but it could be shown that the influence of a high relative humidity can prohibit a crystal that is under anisotropic stress from entering the state of equilibrium. The available water will act as a diffusion bridge to transport ions from the loaded sides of the crystal towards the more favorable unloaded sides. This effect could be visualized by scanning electron microscopy on the surface of a NaCl crystal as hydrates are not stable under vacuum conditions.

9 Zusammenfassung

Vor kurzem diktierte die Politik einen Wandel in der Energieproduktion, weg von fossilen Brennstoffen auf Kohlenstoffbasis und der Kernenergie hin zu erneuerbarer Energieerzeugung. Im Bereich der Hausheizung in der BRD besteht ein großes Potenzial für die Anwendung der erneuerbaren Wärmeerzeugung. Mit den richtigen Speichertechnologien zur Übertragung von Wärme von Zeiten des Überangebots auf Zeiten hoher Nachfrage könnten bis zu 1.9 EJ der Energieproduktion auf den erneuerbaren Sektor übertragen werden. Diese Energiemenge entspricht etwa 14.3% der Primärenergieproduktion in der BRD. Darüber hinaus könnten große Mengen an CO₂-Emissionen vermieden werden und neben des wirtschaftlichen Vorteils der Einsparung großer Mengen konventioneller Energieträger wird die Unabhängigkeit von ausländischen Importen erhöht.

Das Hauptaugenmerk beim Wechsel auf den Bereich der erneuerbaren Energien liegt bei ihrer Unzuverlässigkeit was die vorhersehbare Energieproduktion angeht. Darüber hinaus überschneidet sich nicht nur die saisonale, sondern auch die tägliche Energieversorgung der erneuerbaren Energien selten mit der Nachfrage der Verbraucher. Um diese Probleme zu lösen, sind sowohl langfristige als auch kurzfristige Energiespeichertechnologien erforderlich. Diese Arbeit konzentriert sich auf die Charakterisierung von Materialien, um ihr Potential zu bewerten, als Speichermaterial für die thermochemische Energiespeicherung verwendet zu werden. Neben den beiden anderen reversiblen Technologien, die für die Wärmespeicherung verfügbar sind, dem sensiblen und latenten Wärmespeicher, zeigt die thermochemische Anwendung die höchste Speicherdichte, eine Eigenschaft, die großen Einfluss haben wird, wenn Speichereinheiten den Zustand der kommerziellen Verfügbarkeit erreichen.

Die Verwendung von Salzhydraten für eine thermochemische Energiespeicheranwendung wird bereits seit einigen Jahrzehnten untersucht, aber in neueren Studien werden oft sehr strenge Reaktionsbedingungen definiert, um eine sehr große Menge an potentiellen Materialien zu messen. Diese Arbeit konzentriert sich auf wenige Materialien, die im Detail charakterisiert werden, damit nicht nur das Energiespeicherforschungsgebiet von ihren Ergebnissen profitieren kann, sondern auch andere Bereiche wie die Hydrometallurgie oder sogar in Teilen den Bereichen der Bauchemie und der Denkmalpflege.

Die allgemeinen Gleichungen für die Beziehungen zwischen den thermodynamischen Grundlagen der Elektrolytlösungen und den Korrekturtermen für ihr reales Verhalten sind in Kapitel 2 wiedergegeben. Dieses Kapitel enthält auch die erforderlichen Gleichungen für das verwendete Pitzer-Ionen-Wechselwirkungsmodell, das zur Berechnung der Aktivitätskoeffizienten des gelösten Stoffs und der Wasseraktivität der Elektrolytlösung verwendet wird. Darüber hinaus wird eine Einführung in die erforderlichen thermodynamischen und thermochemischen Größen für eine Parametrisierung der Eigenschaften der Elektrolytlösungen gegeben. Die Phasendiagramme, die verwendet werden, um die Stabilitätsfelder jeder Phase anzuzeigen, werden erklärt. Beispiele für Phasenänderungen mit variierenden Bedingungen werden gegeben und der Einfluss des Drucks auf das Wachstum von Salzkristallen wird dargestellt.

Die wichtigsten Ergebnisse dieser Arbeit sind in den Kapiteln 3 bis 5, in denen die detaillierten Arbeiten zur Charakterisierung der drei untersuchten Salzsysteme $\text{ZnSO}_4\text{-H}_2\text{O}$, $\text{CuSO}_4\text{-H}_2\text{O}$ und $\text{CaSO}_4\text{-H}_2\text{O}$ im Temperaturbereich von 273 K bis 373 K erläutert werden, dargestellt.

Kapitel 3 und 4 zeigen jeweils den Ansatz, bei dem eine ausführliche Datenbasis in der Literatur existierte. Die Daten über die entsprechenden Lösungseigenschaften sowie thermochemische Daten wurden kritisch bewertet und zusätzlich durch isopiestic Daten im Falle von ZnSO_4 (aq) und Wärmekapazitätsdaten für wässrige CuSO_4 -Lösungen ergänzt. Die isopiestic Messungen wurden in einem vollautomatischen Wasserdampfsorptionsmessgerät durchgeführt, der viele simultane Messungen ermöglichte. Mit der Möglichkeit, Aktivitätskoeffizienten und Wasseraktivitäten der jeweiligen Elektrolytlösungen zu berechnen, konnten Löslichkeitsprodukte der verschiedenen Phasen aus den Löslichkeitsdaten berechnet werden. Diese Ergebnisse wurden dann mit weiteren Werten aus Hydratations-Dehydratations-Gleichgewichten ergänzt. Dies ermöglichte die Erstellung konsistenter Phasendiagramme, die sowohl stabile als auch metastabile Phasengrenzen im untersuchten Temperaturbereich abdecken. Im Falle einer Heizungsanwendung für den Heimgebrauch wird der gesamte Bereich mit experimentellen Daten abgedeckt. In den äußeren Temperaturbereichen erfordern einige Fälle Extrapolationen, die eine kleine Unsicherheit für die vorhergesagten Werte hinterlassen.

Kapitel 5 beschäftigt sich mit $\text{CaSO}_4\text{-H}_2\text{O}$, einem System, in dem fast keine thermodynamischen Daten vorliegen. Hier war ein anderer Ansatz erforderlich bei dem Werte bei 298.15 K mit den bestehenden Parametern eines ähnlichen Salzes, $\text{MgSO}_4\text{-H}_2\text{O}$, kombiniert wurden. So wurde die Definition der Temperaturabhängigkeit für wässrige CaSO_4 Lösungen ermöglicht. Die große Datenbasis für Löslichkeiten wurde ausgewertet und die Phasengrenzen für Gips, unlöslichen Anhydrit und α -Hemihydrat wurden bestimmt. Diese Berechnungen wurden mit Änderungen zwischen den oben erwähnten Phasen aus isothermen Löslichkeiten in Lösungen, die ein einziges zusätzliches Salz oder eine Säure enthielten, ergänzt. Auf diese Weise konnten Werte für Hydratations-Dehydratations-Gleichgewichte ermittelt werden, während ihre direkten Messungen immer wieder zu sehr widersprüchlichen Ergebnissen führen. Darüber hinaus konnte die hoch diskutierte Übergangstemperatur zwischen Gips und unlöslichem Anhydrit auf 315 ± 2 K festgelegt werden.

Der Einfluss des Drucks auf hydratisierte Kristalle wird experimentell in Kapitel 6 untersucht. Ein neuer Ansatz wird verfolgt, der die Messung der absoluten Belastbarkeit von Hydratkristallen am Beispiel des Systems $\text{Na}_2\text{SO}_4\text{-H}_2\text{O}$ untersucht. Während der Messreihen wurde der Gleichgewichtszustand nie erreicht, aber es konnte gezeigt werden, dass der Einfluss einer hohen relativen Feuchtigkeit einen unter anisotropen Belastungen stehenden Kristall daran hindern kann in den Gleichgewichtszustand zu kommen. Das verfügbare Wasser wirkt als Diffusionsbrücke, die den Transport von Ionen von den belasteten Flächen des Kristalls zu den günstigeren unbelasteten Flächen ermöglicht. Dieser Effekt konnte durch Rasterelektronenmikroskopie auf der Oberfläche eines NaCl -Kristalls sichtbar gemacht werden, da Hydrate unter Vakuumbedingungen nicht stabil sind.

10 References

- [1] "Primärenergieverbrauch nach Energieträgern", can be found under https://www.bmwi.de/SiteGlobals/BMWI/Forms/Listen/Energiedaten/energiedaten_Formular.html?&addSearchPathId=304670, **2016**.
- [2] R. Aringhoff, M. Geyer, U. Herrmann, R. Kistner, P. Nava, R. Osuna in *Proceedings of the 11th SolarPACES International Symposium on Concentrated Solar Power and Chemical Energy Technologies. September 4-6, 2002, Zurich, Switzerland* (Ed.: A. Steinfeld), Paul Scherrer Institut, Villigen [Switzerland], **2002**, pp. 37–42.
- [3] R. Schlögl, *Chemical Energy Storage*, De Gruyter, Berlin, **2013**.
- [4] J. Jänchen, D. Ackermann, H. Stach, W. Brösicke, *Sol. Energy* **2004**, 76, 339.
- [5] "Endenergieverbrauch nach Anwendungsgebieten", can be found under https://www.bmwi.de/SiteGlobals/BMWI/Forms/Listen/Energiedaten/energiedaten_Formular.html?&addSearchPathId=304670, **2015**.
- [6] V. Wesselak, T. Schabbach, T. Link, J. Fischer, *Regenerative Energietechnik*, Springer Vieweg; Springer, [S.l.], **2013**.
- [7] W. Wagner, A. Pruß, *J. Phys. Chem. Ref. Data* **2002**, 31, 387.
- [8] A. V. Novo, J. R. Bayon, D. Castro-Fresno, J. Rodriguez-Hernandez, *Appl. Energ.* **2010**, 87, 390.
- [9] E. Levitskji, Y. I. Aristov, M. M. Tokarev, V. N. Parmon, *Sol. Energ. Mat. Sol. C.* **1996**, 44, 219.
- [10] H. Kerskes, F. Bertsch, B. Mette, A. Wörner, F. Schaube, *Chem.-Ing.-Tech.* **2011**, 83, 2014.
- [11] Y. Ding, S. B. Riffat, *Int. J. Low-Carbon Tech.* **2015**, 8, 106.
- [12] K. E. N'Tsoukpoe, T. Schmidt, H. U. Rammelberg, B. A. Watts, W. K. Ruck, *Appl. Energ.* **2014**, 124, 1.
- [13] M. Steiger, K. Linnow, D. Ehrhardt, M. Rohde, *Geochim. Cosmochim. Ac.* **2011**, 75, 3600.

- [14] K. Posern, K. Linnow, M. Niermann, C. Kaps, M. Steiger, *Thermochim. Acta* **2015**, *611*, 1.
- [15] P. A. Kallenberger, F. J. Brieler, K. Posern, M. Fröba, *Chem.-Ing.-Tech.* **2016**, *88*, 379.
- [16] M. Meier, *Staatsexamensarbeit*, Universität Hamburg, Hamburg, **2007**.
- [17] R. J. Flatt, G. W. Scherer, *MRS Proc.* **2002**, 712.
- [18] M. Steiger, K. Linnow, H. Juling, G. Gülker, A. E. Jarad, S. Brüggerhoff, D. Kirchner, *Cryst. Growth Des.* **2008**, *8*, 336.
- [19] M. B. Ewing, T. H. Lilley, G. M. Olofsson, M. T. Rätzsch, G. Somsen, *J. Chem. Thermodyn.* **1995**, *27*, 1.
- [20] J. A. Rard, R. F. Platford in *Activity Coefficients in Electrolyte Solutions*, CRC Press, Boca Raton, **1991**, pp. 209–277.
- [21] K. S. Pitzer, *Thermodynamics*, McGraw-Hill, New York et al., **1995**.
- [22] W. Wagner, J. R. Cooper, A. Dittmann, J. Kijima, H.-J. Kretzschmar, A. Kruse, R. Mareš, K. Oguchi, H. Sato, I. Stöcker et al., *J. Eng. Gas Turb. Power* **2000**, *122*, 150.
- [23] K. S. Pitzer, *Activity Coefficients in Electrolyte Solutions*, CRC Press, Boca Raton, **1991**.
- [24] D. G. Archer, *J. Phys. Chem. Ref. Data* **1991**, *20*, 509.
- [25] K. S. Pitzer, P. Wang, J. A. Rard, S. L. Clegg, *J. Solution Chem.* **1999**, *28*, 265.
- [26] D. G. Archer, P. Wang, *J. Phys. Chem. Ref. Data* **1990**, *19*, 371.
- [27] M. Steiger, J. Kiekbusch, A. Nicolai, *Constr. Build. Mater.* **2008**, *22*, 1841.
- [28] K. S. Pitzer, G. Mayorga, *J. Solution Chem.* **1974**, *3*, 539.
- [29] V. K. Filippov, D. S. Barkov, Y. A. Fedorov, *J. Solution Chem.* **1986**, *15*, 611.
- [30] G. W. Scherer, *Cement Concrete Res.* **1999**, *29*, 1347.
- [31] M. Steiger, *J. Cryst. Growth* **2005**, *282*, 455.
- [32] H. Mortensen, *Petermanns Mitt.* **1933**, *79*, 130.

-
- [33] R. Beyer, M. Steiger, *J. Chem. Thermodyn.* **2002**, *34*, 1057.
- [34] a) *Ullmann's encyclopedia of industrial chemistry. Water to zirconium and zirconium compounds*, Wiley-VCH-Verl., Weinheim, **2011**; b) E. Catelli, F.-G. Bănică, A. Bănică, *Herit. Sci.* **2016**, *4*, 196.
- [35] a) E. Guerra, M. Bestetti, *J. Chem. Eng. Data* **2006**, *51*, 1491; b) H. Liu, V. G. Papangelakis, *Fluid Phase Equilib.* **2005**, *234*, 122.
- [36] G. Azimi, V. G. Papangelakis, J. E. Dutrizac, *Can. Metall. Quart.* **2010**, *49*, 1.
- [37] J. M. Hammarstrom, R. R. Seal, A. L. Meier, J. M. Kornfeld, *Chem. Geol.* **2005**, *215*, 407.
- [38] F. Grønvold, K. K. Meisingset, *J. Chem. Thermodyn.* **1982**, *14*, 1083.
- [39] J. D'Ans, H.-E. Freund, E. Kaufmann, *Z. Elektrochem.* **1957**, *61*, 546.
- [40] J. D'Ans, H.-E. Freund, *Z. Elektrochem.* **1960**, *64*, 517.
- [41] I.-M. Chou, R. R. Seal, *Chem. Geol.* **2005**, *215*, 517.
- [42] C. W. DeKock, *Thermodynamic Properties of Selected Transition Metal Sulphates and Their Hydrates*. US Bureau of Mines Information Circular 9081, U.S. Bureau of Mines, Washington, DC, **1986**.
- [43] D. D. Wagman, W. H. Evans, V. B. Parker, R. H. Schumm, I. Halow, S. M. Bailey, K. L. Churney, R. L. Nuttal, *J. Phys. Chem. Ref. Data* **1982**, *11*, 1.
- [44] K.-D. Grevel, J. Majzlan, *Chem. Geol.* **2011**, *286*, 301.
- [45] J. G. Albright, J. A. Rard, S. Serna, E. E. Summers, M. C. Yang, *J. Chem. Thermodyn.* **2000**, *32*, 1447.
- [46] E. Königsberger, G. Eriksson, *Calphad* **1995**, *19*, 207.
- [47] W. Wang, D. Zeng, H. Zhou, X. Wu, X. Yin, *J. Chem. Eng. Data* **2015**, *60*, 3024.
- [48] D. G. Archer, *J. Phys. Chem. Ref. Data* **1992**, *21*, 793.
- [49] R. Beyer, M. Steiger, *J. Chem. Eng. Data* **2010**, *55*, 830.
- [50] M. Steiger, *Chem. Geol.* **2016**, *436*, 84.
-

- [51] C. M. Criss, F. J. Millero, *J. Solution Chem.* **1999**, *28*, 849.
- [52] H. Yang, D. Zeng, W. Voigt, G. Hefter, S. Liu, Q. Chen, *J. Chem. Eng. Data* **2014**, *59*, 97.
- [53] H. Yang, D. Zeng, W. Voigt, Y. Chen, Q. Zhou, *J. Chem. Eng. Data* **2016**, *61*, 3406.
- [54] J. Ananthaswamy, G. Atkinson, *J. Appl. Chem.* **1985**, *30*, 120.
- [55] S. L. Clegg, J. A. Rard, K. S. Pitzer, *J. Chem. Soc. Faraday T.* **1994**, *90*, 1875.
- [56] H. F. Holmes, R. H. Busey, J. M. Simonson, R. E. Mesmer, *J. Chem. Thermodyn.* **1994**, *26*, 271.
- [57] L. Kahlenberg, *J. Phys. Chem.* **1900**, *5*, 339.
- [58] F. Rüdorff, *Ann. Phys. Chem.* **1872**, *221*, 599.
- [59] H. Hausrath, *Ann. Phys.* **1902**, *314*, 522.
- [60] M. de Coppet, *Ann. Chim. Phys.* **1872**, *4*, 502.
- [61] P. G. M. Brown, J. E. Prue, *P. Roy. Soc. A-Math. Phy.* **1955**, 232, 320.
- [62] I. M. Klotz, R. M. Rosenberg, *Chemical Thermodynamics. Basic theory and methods*, Benjamin/Cummings, Menlo Park CA, **1972**.
- [63] H. Jones, F. Getman, *Z. Phys. Chem.* **1904**, *49*, 385.
- [64] E. Plake, *Z. Phys. Chem.* **1935**, *172A*, 113.
- [65] G. T. Gerlach, *Z. Anal. Chem.* **1887**, *26*, 413.
- [66] S. M. Johnston, *T. Roy. Soc. Edin.* **1908**, *45*, 855.
- [67] R. P. Smith, *J. Am. Chem. Soc.* **1939**, *61*, 500.
- [68] G. Tammann, *Z. Phys. Chem.* **1888**, *2*, 42.
- [69] G. Tammann, *Ann. Phys.* **1885**, *260*, 523.
- [70] N. V. Sidgwick, E. K. Ewbank, *J. Chem. Soc.* **1924**, *125*, 2268.
- [71] W. Kangro, A. Groeneveld, *Z. Phys. Chem.* **1962**, *32*, 110.
- [72] R. Emden, *Ann. Phys. Chem.* **1887**, *267*, 145.

-
- [73] C. Dieterici, *Ann. Phys.* **1923**, 375, 617.
- [74] G. S. Kell, *J. Phys. Chem. Ref. Data* **1977**, 6, 1109.
- [75] A. Wexler, L. Greenspan, *J. Res. NBS. A Phys. Ch.* **1971**, 75A, 213.
- [76] E. Lange, J. Monheim, A. L. Robinson, *J. Am. Chem. Soc.* **1933**, 55, 4733.
- [77] W. F. Giauque, R. E. Barieau, J. E. Kunzler, *J. Am. Chem. Soc.* **1950**, 72, 5685.
- [78] E. Plake, *Z. Phys. Chem.* **1932**, 162A, 257.
- [79] J.-C. Marignac, *Arch. Phys. Nat.* **1876**, 55, 113.
- [80] E. Cohen, W. Helderman, A. Moesveld, *Z. Phys. Chem.* **1924**, 112, 135.
- [81] A. Groeneveld, *Dissertation*, Technische Hochschule Carolo-Wilhelmina zu Braunschweig, Braunschweig, **1956**.
- [82] J. Timmermans, *The Physico-chemical Constants of Binary Systems in Concentrated Solutions. Volume 3. Systems with metallic compounds.*, Interscience Publishers, New York, **1960**.
- [83] A. Benrath, *Z. Anorg. Allg. Chem.* **1930**, 189, 82.
- [84] A. Benrath, *Z. Anorg. Allg. Chem.* **1931**, 202, 161.
- [85] W. Schröder, *Z. Anorg. Allg. Chem.* **1936**, 228, 129.
- [86] R. Rohmer, *C. R. Acad. Sci.* **1940**, 210, 669.
- [87] H. L. Callendar, H. T. Barnes, *Proc. R. Soc. London* **1897**, 62, 117.
- [88] E. Cohen, *Z. Phys. Chem.* **1900**, 79.
- [89] E. Cohen, C. W. G. Hetterschij, *Z. Phys. Chem.* **1925**, 440.
- [90] R. M. Caven, W. Johnston, *J. Chem. Soc.* **1926**, 129, 2628.
- [91] C. R. Bury, *J. Chem. Soc.* **1924**, 125, 2538.
- [92] G. Agde, F. Schimmel, *Z. Angew. Chem.* **1928**, 41, 340.
- [93] L. C. Copeland, O. A. Short, *J. Am. Chem. Soc.* **1940**, 62, 3285.
- [94] E. V. Jones, M. H. Lietzke, W. L. Marshall, *J. Am. Chem. Soc.* **1957**, 79, 267.
-

- [95] G. Wiedemann, *J. Prakt. Chem.* **1874**, 9, 338.
- [96] P. Frowein, *Z. Phys. Chem.* **1887**, 1, 5.
- [97] C. R. Schulze, *Wied. Ann. Phys.* **1887**, 204.
- [98] M. H. Lescoeur, *Ann. Chim. Phys.* **1890**, 21, 511.
- [99] C. E. Linebarger, *Z. Phys. Chem.* **1894**, 500.
- [100] W. Müller-Erzbach, *Z. Phys. Chem.* **1896**, 19, 135.
- [101] H. W. Foote, S. R. Scholes, *J. Am. Chem. Soc.* **1911**, 33, 1309.
- [102] A. A. Noyes, L. R. Westbrook, *J. Am. Chem. Soc.* **1921**, 43, 726.
- [103] H. M. Roberts, C. R. Bury, *J. Chem. Soc. T.* **1923**, 123, 2037.
- [104] W. C. Schumb, *J. Am. Chem. Soc.* **1923**, 45, 342.
- [105] F. Ishikawa, T. Murooka, *Sci. Rep. Res. Tohoku A* **1933**, 1, 138.
- [106] D. G. R. Bonnell, L. W. Burrige, *T. Faraday Soc.* **1935**, 31, 473.
- [107] J. Bell, *J. Chem. Soc.* **1940**, 72.
- [108] K. Kohler, P. Zäske, *Z. Anorg. Allg. Chem.* **1964**, 331, 1.
- [109] Y. K. Uvaliev, G. A. Motornaya, *Izv. Akad. Nauk Kaz. SSSR Ser. Khim.* **1989**, 54.
- [110] M. Diesnis, *Bull. Soc. Chim. Fr.* **1935**, 1901.
- [111] Y. Kou, S. J. Schmidt, *Food Chem.* **1999**, 66, 253.
- [112] R. E. Barieau, W. F. Giauque, *J. Am. Chem. Soc.* **1950**, 72, 5676.
- [113] E. Cohen, K. Inouye, C. Euwen, *Z. Phys. Chem.* **1911**, 1.
- [114] a) H. W. Richardson in *Kirk-Othmer Encyclopedia of Chemical Technology* (Ed.: J. Kroschwitz), Wiley, Hoboken, **1994**; b) C. Akilan, P. M. May, G. Hefter, *J. Solution Chem.* **2014**, 43, 885; c) "Uses of Copper Compounds: Table A - Uses of Copper Sulphate", can be found under https://www.copper.org/resources/properties/compounds/table_a.html.

-
- [115] W. G. Davenport, A. K. Biswas, *Extractive metallurgy of copper*, Pergamon, Oxford, **2002**.
- [116] P. J. Bartos, *Resour. Policy* **2002**, 28, 85.
- [117] J. L. Jambor, D. K. Nordstrom, C. N. Alpers, *Rev. Mineral. Geochem.* **2000**, 40, 303.
- [118] J. L. Jambor, *Can. Mineral.* **1964**, 8, 92.
- [119] C. Ferchaud, *Dissertation*, Technische Universiteit, Eindhoven, **2016**.
- [120] I.-M. Chou, R. R. Seal, B. S. Hemingway, *Am. Mineral.* **2002**, 87, 108.
- [121] C. J. Downes, K. S. Pitzer, *J. Solution Chem.* **1976**, 5, 389.
- [122] W. Libuś, T. Sadowska, Z. Libuś, *J. Solution Chem.* **1980**, 9, 341.
- [123] D. G. Miller, J. A. Rard, L. B. Eppstein, R. A. Robinson, *J. Solution Chem.* **1980**, 9, 467.
- [124] C. Akilan, *Dissertation*, Murdoch University, Perth, **2008**.
- [125] W. Birnthaler, E. Lange, *Z. Elektrochem. Angew. P.* **1937**, 43, 643.
- [126] R. A. Robinson, R. S. Jones, *J. Am. Chem. Soc.* **1936**, 58, 959.
- [127] D. G. Archer, *J. Phys. Chem. Ref. Data* **1999**, 28, 1.
- [128] F. Hovorka, W. H. Rodebush, *J. Am. Chem. Soc.* **1925**, 47, 1614.
- [129] R. F. Nielsen, D. J. Brown, *J. Am. Chem. Soc.* **1927**, 49, 2423.
- [130] F. H. Getman, *J. Phys. Chem.* **1930**, 34, 1454.
- [131] F. E. W. Wetmore, A. R. Gordon, *J. Chem. Phys.* **1937**, 5, 60.
- [132] F. Müller, H. Reuther, *Z. Elektrochem. Angew. P.* **1941**, 47, 640.
- [133] F. Müller, H. Reuther, *Z. Elektrochem. Angew. P.* **1942**, 48, 682.
- [134] Kapustinskii A.F., D. S. Yakushevski B.M., *Zh. Fiz. Khim.* **1953**, 27, 588.
- [135] G. S. Kell, *J. Chem. Eng. Data* **1975**, 20, 97.
- [136] M. Poggiale, *Ann. Chim. Phys.* **1843**, 3, 463.

- [137] E. Tobler, *Ann. Chem. Pharm.* **1855**, 95, 193.
- [138] F. Pfaff, *Ann. Chem. Pharm.* **1856**, 99, 224.
- [139] H. Schiff, *Ann. Chem. Pharm.* **1861**, 118, 362.
- [140] K. R. von Hauer, *J. Prakt. Chem.* **1868**, 103, 114.
- [141] G. E. Patrick, A. B. Aubert, *Trans. Kans. Acad. Sci.* **1874**, 3, 117.
- [142] J. E. Trevor, *Z. Phys. Chem.* **1897**, 7, 468.
- [143] M. Etard, *Ann. Chim. Phys.* **1894**, 7, 503.
- [144] W. Stortenbeker, *Z. Phys. Chem.* **1897**, 22, 60.
- [145] E. Cohen, J. W. Commelin, *Z. Elektrotech. Elektrochem.* **1903**, 9, 431.
- [146] J. Koppel, *Z. Phys. Chem.* **1905**, 52, 385.
- [147] E. Cohen, F. D. Chattaway, E. Tombrock, *Z. Phys. Chem.* **1907**, 60, 706.
- [148] F. Schreinemakers, *Z. Phys. Chem.* **1909**, 69, 557.
- [149] A. Massink, *Z. Phys. Chem.* **1916**, 92, 351.
- [150] H. W. Foote, *J. Ind. Eng. Chem.* **1919**, 11, 629.
- [151] Lattey R., *Dissertation*, TU Braunschweig, **1923**.
- [152] G. Agde, H. Barkholt, *Z. Angew. Chem.* **1926**, 39, 851.
- [153] R. M. Caven, W. Johnston, *J. Chem. Soc.* **1927**, 0, 2358.
- [154] F. Flöttmann, *Z. Anal. Chem.* **1928**, 73, 1.
- [155] A. Benrath, H. Benrath, *Z. Anorg. Allg. Chem.* **1929**, 179, 369.
- [156] W. J. Müller, L. Holleck, *Monatsh. Chem.* **1929**, 52, 409.
- [157] H. D. Crockford, M. W. Webster, *J. Phys. Chem.* **1929**, 34, 2375.
- [158] H. D. Crockford, L. E. Warrick, *J. Phys. Chem.* **1929**, 34, 1064.
- [159] H. D. Crockford, D. J. Brawley, *J. Phys. Chem.* **1931**, 36, 1594.
- [160] F. T. Miles, A. W. C. Menzies, *J. Am. Chem. Soc.* **1937**, 59, 2392.

-
- [161] F. Schreinemakers, *KNAW Proc.* **1911**, *13*, 1163.
- [162] Tilden W. A., W. A. Shenstone, *Philos. Trans. Roy. Soc. London* **1883**, *175*, 23.
- [163] F. Ishikawa, *J. Chem. Soc. Japan* **1923**, *44*, 708.
- [164] A. Naumann, *Ber. Dtsch. Chem. Ges.* **1874**, *7*, 1573.
- [165] A. H. Pareau, *Ann. Phys.* **1877**, *237*, 39.
- [166] W. Müller-Erzbach, *Ber. Dtsch. Chem. Ges.* **1886**, *19*, 2877.
- [167] W. Müller-Erzbach, *Ann. Phys. Chem.* **1887**, *268*, 313.
- [168] W. Müller-Erzbach, *Ann. Phys. Chem.* **1888**, *270*, 1047.
- [169] G. Tammann, *Ann. Phys. Chem.* **1888**, *269*, 322.
- [170] Bouzat M. A., *C. R. Acad. Sci.* **1903**, 1395.
- [171] A. C. Cumming, *J. Chem. Soc. T.* **1909**, *95*, 1772.
- [172] Biltz. W., *Z. Phys. Chem.* **1909**, 561.
- [173] J. R. Partington, *J. Chem. Soc. T.* **1911**, *99*, 466.
- [174] A. Siggel, *Z. Elektrochem. Angew. P.* **1913**, *19*, 340.
- [175] A. W. C. Menzies, *J. Am. Chem. Soc.* **1920**, *42*, 1951.
- [176] R. E. Wilson, *J. Am. Chem. Soc.* **1921**, *43*, 704.
- [177] C. D. Carpenter, E. R. Jette, *J. Am. Chem. Soc.* **1923**, *45*, 578.
- [178] J. R. Partington, D. B. Huntingford, *J. Chem. Soc. T.* **1923**, *123*, 160.
- [179] A. W. C. Menzies, C. S. Hitchcock, *J. Phys. Chem.* **1930**, *35*, 1660.
- [180] T. S. Logan, *J. Phys. Chem.* **1931**, *36*, 1035.
- [181] A. W. C. Menzies, F. T. Miles, *J. Am. Chem. Soc.* **1934**, *56*, 1647.
- [182] C. F. Prutton, S. H. Maron, E. D. Unger, *J. Am. Chem. Soc.* **1935**, *57*, 407.
- [183] K. Sano, *Sci. Rep. Res. Tohoku A* **1935**, *24*, 719.
- [184] H. Perpérot, F. Schacherl, *J. Phys. Radium* **1935**, *6*, 439.
-

- [185] E. M. Collins, A. W. C. Menzies, *J. Phys. Chem.* **1935**, *40*, 379.
- [186] D. Balarew, *Monatsh. Chem.* **1937**, *71*, 30.
- [187] B. Ghosh, *J. Indian Chem. Soc.* **1945**, *22*, 17.
- [188] J. R. I. Hepburn, R. F. Phillips, *J. Chem. Soc.* **1952**, 2569.
- [189] D. Puchalska, G. Atkinson, S. Routh, *J. Solution Chem.* **1993**, *22*, 625.
- [190] a) P. Pawlowitsch, *Z. Phys. Chem.* **1913**, 169; b) M. Diesnis, *Ann. Chim.* **1937**, *7*, 5; c) M. L. Pollio, D. Kitic, S. L. Resnik, *LWT-Food Sci. Technol.* **1996**, *29*, 376; d) A. N. Kirgintsev, Luk'yanov A. V., *Russ. J. Inorg. Chem.* **1967**, *12*, 1070.
- [191] Van't Hoff, J. H., E. F. Armstrong, W. Hinrichsen, F. Weigert, G. Just, *Z. Phys. Chem.* **1903**, *45*, 257.
- [192] E. P. Partridge, A. H. White, *J. Am. Chem. Soc.* **1929**, *51*, 360.
- [193] J. D'Ans, P. Höfer, *Angew. Chem.* **1937**, *50*, 101.
- [194] J. D'Ans, D. Bredtschneider, H. Eick, H. E. Freund, *Kali und Steinsalz* **1955**, *1*, 17.
- [195] A. E. Hill, *J. Am. Chem. Soc.* **1937**, *59*, 2242.
- [196] E. Posnjak, *Am. J. Sci.* **1938**, *5*, 247.
- [197] E. Bock, *Can. J. Chem.* **1961**, *39*, 1746.
- [198] E.-A. Zen, *J. Petrol.* **1965**, *6*, 124.
- [199] K. K. Kelley, J. C. Southard, C. T. Anderson, *U.S. Bur. Mines Tech. Paper* **1941**, 1.
- [200] L. A. Hardie, *Am. Mineral.* **1967**, *52*, 171.
- [201] C. W. Blount, F. W. Dickson, *Am. Mineral.* **1973**, *58*, 323.
- [202] O. Knacke, W. Gans, *Z. Phys. Chem.* **1977**, *104*, 41.
- [203] A. B. Zdanovskii, G. A. Vlasov, *Russ. J. Inorg. Chem.* **1968**, *13*, 1318.
- [204] V. P. Kruchenko, B. A. Beremzhanov, *Russ. J. Inorg. Chem.* **1978**, *23*, 1056.
- [205] G. Innorta, E. Rabbi, L. Tomadin, *Geochim. Cosmochim. Ac.* **1980**, *44*, 1931.







- [206] a) C. E. Harvie, H. P. Eugster, J. H. Weare, *Geochim. Cosmochim. Ac.* **1982**, *46*, 1603;
b) C. E. Harvie, N. Møller, J. H. Weare, *Geochim. Cosmochim. Ac.* **1984**, *48*, 723.
- [207] C. E. Harvie, J. H. Weare, *Geochim. Cosmochim. Ac.* **1980**, *44*, 981.
- [208] N. Møller, *Geochim. Cosmochim. Ac.* **1988**, *52*, 821.
- [209] M. Whitfield, *Mar. Chem.* **1975**, *3*, 197.
- [210] Raju, K. U. G., G. Atkinson, *J. Chem. Eng. Data* **1990**, *35*, 361.
- [211] G. Azimi, V. G. Papangelakis, J. E. Dutrizac, *Fluid Phase Equilibr.* **2007**, *260*, 300.
- [212] a) W. Steiner, *Int. J. Rock. Mech. Min.* **1993**, *30*, 361; b) L. Oldecop, E. Alonso, *Int. J. Rock. Mech. Min.* **2012**, *54*, 90; c) K. Serafeimidis, G. Anagnostou, *Environ. Earth Sci.* **2014**, *72*, 4985.
- [213] E. E. Alonso, A. Ramon, *Géotechnique* **2013**, *63*, 707.
- [214] I. Sass, U. Burbaum, *Acta Carsologica* **2012**, *39*.
- [215] D. Freyer, W. Voigt, *ZKG Int.* **2009**, *62*, 47.
- [216] J. Schneider, *Dissertation*, TU Bergakademie Freiberg, Freiberg, **2010**.
- [217] a) C. S. Gibson, S. Holt, *J. Chem. Soc.* **1933**, 638; b) D. Balarew, A. Koluschewa, *Kolloid Z.* **1935**, *70*, 288; c) H. B. Weiser, W. O. Milligan, W. C. Ekholm, *J. Am. Chem. Soc.* **1936**, *58*, 1261; d) L. S. Ramsdell, E. P. Partridge, *Am. Mineral.* **1929**, *14*, 59.
- [218] A. G. Ostroff, *Geochim. Cosmochim. Ac.* **1964**, *28*, 1363.
- [219] A. E. Charola, J. Pühringer, M. Steiger, *Environ. Geol.* **2007**, *52*, 339.
- [220] K. S. Pitzer, *J. Chem. Soc. Faraday T. 2* **1972**, *68*, 101.
- [221] E. Königsberger in *Highlights in Solute-Solvent Interactions* (Ed.: W. Linert), Springer Vienna, Vienna, **2002**, pp. 127–150.
- [222] J. D'Ans, *Die Lösungsgleichgewichte der Systeme der Salze ozeanischer Salzablagerungen*, Verlagsgesellschaft f. Ackerbau m. b. H., Berlin, **1933**.
- [223] A. E. Hill, *J. Am. Chem. Soc.* **1934**, *56*, 1071.
- [224] W. H. Power, B. M. Fabuss, *J. Chem. Eng. Data* **1964**, *9*, 437.

- [225] Silcock H. L., *Solubilities of Inorganic and Organic Compounds: Ternary and Multicomponent Systems of Inorganic Substances*, Pergamon Press, Oxford, **1979**.
- [226] C. Marignac, *Fresen. Z. Anal. Chem.* **1874**, *13*, 57.
- [227] F. K. Cameron, *J. Phys. Chem.* **1900**, *5*, 556.
- [228] F. K. Cameron, A. Seidell, *J. Phys. Chem.* **1900**, *5*, 643.
- [229] G. A. Hulett, L. E. Allen, *J. Am. Chem. Soc.* **1902**, *24*, 667.
- [230] F. K. Cameron, J. F. Breazeale, *J. Phys. Chem.* **1902**, *7*, 571.
- [231] A. Seidell, J. G. Smith, *J. Phys. Chem.* **1903**, *8*, 493.
- [232] F. K. Cameron, J. M. Bell, *J. Phys. Chem.* **1905**, *10*, 210.
- [233] A. C. Melcher, *J. Am. Chem. Soc.* **1910**, *32*, 50.
- [234] W. D. Harkins, H. M. Paine, *J. Am. Chem. Soc.* **1919**, *41*, 1155.
- [235] P. S. Roller, *J. Phys. Chem.* **1930**, *35*, 1133.
- [236] A. E. Hill, N. S. Yanick, *J. Am. Chem. Soc.* **1935**, *57*, 645.
- [237] A. E. Hill, J. H. Wills, *J. Am. Chem. Soc.* **1938**, *60*, 1647.
- [238] W. M. Madgin, D. A. Swales, *J. Appl. Chem.* **1956**, *6*, 482.
- [239] W. M. Madgin, D. A. Swales, *J. Chem. Soc.* **1956**, 196.
- [240] W. Denman, *Ind. Eng. Chem.* **1961**, *53*, 817.
- [241] W. L. Marshall, R. Slusher, E. V. Jones, *J. Chem. Eng. Data* **1964**, *9*, 187.
- [242] W. H. Power, B. M. Fabuss, C. N. Satterfield, *J. Chem. Eng. Data* **1966**, *11*, 149.
- [243] A. G. Ostroff, A. V. Metler, *J. Chem. Eng. Data* **1966**, *11*, 346.
- [244] W. L. Marshall, R. Slusher, *J. Phys. Chem.* **1966**, *70*, 4015.
- [245] J. Block, O. B. Waters, *J. Chem. Eng. Data* **1968**, *13*, 336.
- [246] A. B. Zdanovskii, G. A. Vlasov, *Russ. J. Inorg. Chem.* **1968**, *13*, 1415.
- [247] A. B. Zdanovskii, G. A. Vlasov, L. I. Sotnikova, *Russ. J. Inorg. Chem.* **1968**, *13*, 1418.

- [248] J. D'Ans, *Kali und Steinsalz* **1968**, 5, 109.
- [249] B. A. Beremzhanov, V. P. Kruchenko, *Russ. J. Inorg. Chem.* **1972**, 17, 1036.
- [250] W. L. Marshall, R. Slusher, *J. Chem. Thermodyn.* **1973**, 5, 189.
- [251] B. A. Beremzhanov, V. P. Kruchenko, *Russ. J. Inorg. Chem.* **1975**, 20, 1746.
- [252] D. Barba, V. Brandani, G. Di Giacomo, *J. Chem. Eng. Data* **1984**, 29, 42.
- [253] A. Kumar, V. P. Mohandas, V. R. K. S. Susarla, P. K. Ghosh, *J. Solution Chem.* **2004**, 33, 995.
- [254] A. Kumar, V. P. Mohandas, R. Sanghavi, P. K. Ghosh, *J. Solution Chem.* **2005**, 34, 333.
- [255] Z. Li, G. P. Demopoulos, *J. Chem. Eng. Data* **2005**, 50, 1971.
- [256] Z. M. Mel'nikova, I. A. Moshkina, A. S. Kolosov, *Izv. Sib. Otd. Akad. Nauk SSSR, Ser. Khim. Nauk* **1971**, 6, 15.
- [257] J. A. Rard, A. Habenschuss, F. H. Spedding, *J. Chem. Eng. Data* **1977**, 22, 180.
- [258] W. L. Marshall, E. V. Jones, *J. Phys. Chem.* **1966**, 70, 4028.
- [259] E. Posnjak, *Am. J. Sci.* **1940**, 238, 559.
- [260] S. L. Clegg, P. Brimblecombe, A. S. Wexler, "Extended AIM Aerosol Thermodynamics Model", can be found under <http://www.aim.env.uea.ac.uk/aim/aim.php>.
- [261] A. S. Wexler, *J. Geophys. Res.* **2002**, 107, 745.
- [262] a) K. S. Carslaw, S. L. Clegg, P. Brimblecombe, *J. Phys. Chem.* **1995**, 99, 11557; b) S. L. Clegg, P. Brimblecombe, *J. Phys. Chem. A* **2005**, 109, 2703–2706; c) M. Massucci, S. L. Clegg, P. Brimblecombe, *J. Phys. Chem. A* **1999**, 103, 4209.
- [263] E. Friese, A. Ebel, *J. Phys. Chem. A* **2010**, 114, 11595.
- [264] E. M. Collins, *J. Phys. Chem.* **1932**, 37, 1191.
- [265] D. Freyer, W. Voigt, *Monatsh. Chem.* **2003**, 134, 693.
- [266] C. E. Harvie, *Ph. D. dissertation*, University of California, San Diego, **1981**.

- [267] Rogers, P. S. Z., *Ph. D. dissertation*, University of California, Berkeley, **1981**.
- [268] H. Holmes, R. Mesmer, *J. Chem. Thermodyn.* **1983**, *15*, 709.
- [269] a) J.-H. Lee, H. Ogura, *Appl. Therm. Eng.* **2013**, *50*, 1557; b) J.-H. Lee, H. Ogura, S. Sato, *Appl. Therm. Eng.* **2014**, *63*, 192.
- [270] C. Rodriguez-Navarro, E. Doehne, *Earth Surf. Process. Landforms* **1999**, *24*, 191.
- [271] O. Knacke, R. von Erdberg, *Berich. Bunsen. Phys. Chem.* **1975**, *79*, 653.
- [272] M. Steiger, S. Asmussen, *Geochim. Cosmochim. Ac.* **2008**, *72*, 4291.
- [273] W. Kleber, H.-J. Bautsch, J. Bohm, *Einführung in die Kristallographie*, Oldenbourg, München, **2010**.
- [274] G. E. Ewing in *Structure and bonding* (Ed.: D. J. Wales), Springer-Verlag, Berlin/Heidelberg, **2005**, pp. 1–25.
- [275] H. Shindo, M. Ohashi, O. Tateishi, A. Seo, *J. Chem. Soc. Faraday T.* **1997**, *93*, 1169.

I Used Chemicals

Substance	GHS-Symbol	H-Sätze	P-Sätze
2-Propanol		H225 H319 H336	P210 P240 P305+P351+P338 P403+P233
Acetone		H225 H319 H336 EUH066	P210 P240 P305+P351+P338 P403+P233
Calcium sulfate	–	–	–
Copper(II) sulfate		H302 H315 H319 H410	P273 P302+P353 P305+P351+P338
Lithium chloride		H302 H315 H319	P302+P352 P305+P351+P388
Magnesium chloride	–	–	–
Potassium acetate	–	–	–
Potassium carbonate		H315 H319 H335	P302+P352 P305+P351+P338
Potassium chloride	–	–	–
Potassium sulfate	–	–	–
Sodium bromide	–	–	–
Sodium chloride	–	–	–
Zinc sulfate		H302 H318 H410	P273 P280 P305+P351+P338 P313

II Statement in Lieu of an Oath (Eidesstattliche Versicherung)

Hiermit versichere ich von Eides statt, die vorliegende Dissertation selbst verfasst und keine anderen als die angegebene Hilfsmittel benutzt zu haben. Die eingereichte schriftliche Fassung entspricht der auf dem elektronischen Speichermedium. Ich versichere, dass diese Dissertation nicht in einem früheren Promotionsverfahren eingereicht wurde

Hamburg, 13. September 2017

Fritz Höffler